LLRF Control Techniques for the European XFEL Continuous Wave Upgrade

vorgelegt von

Andrea Bellandi

Hamburg
2021

To Vanessa, my love.

Contents

Zusammenfassung

In dieser Doktorarbeit werden mögliche Lösungen für supraleitende Hohlraumregelsysteme, die im Continuos Wave (CW)-Regime arbeiten, diskutiert und analysiert. Der Schwerpunkt der Arbeit liegt auf den Anforderungen, die erfüllt sein müssen, um den European XFEL neben der bestehenden gepulsten Betriebsart um eine CW-Betriebsart zu erweitern. Die größte Herausforderung aus Sicht des Regelsystems ergibt sich aus der Notwendigkeit, einen geladenen Qualitätsfaktor (Q_L) im Bereich von 10^7-10^8 zu verwenden. Ein solcher (Q_L) ist eine Größenordnung größer als der tatsächliche Wert, der in der gepulsten Betriebsart verwendet wird. Infolgedessen ist die Gestimmtheit des Resonators empfindlicher gegenüber mikrofonischen Effekten. Aus diesem Grund sind aktive Lärmkompensationsverfahren erforderlich, um den Gesamtverbrauch des Beschleunigungssystems zu begrenzen und die Energiestabilität des beschleunigten Strahls zu erhöhen. Ein weiterer Effekt, der bei der zukünftigen Nachrüstung vorhanden ist, sind ponderomotorische Instabilitäten. Diese Instabilitäten resultieren aus der nichtlinearen Kopplung zwischen der Lorentzkraft bedingten Verstimmung und dem Hohlraumbeschleunigungsfeld. Diese Instabilitäten werden analysiert und ein mögliches Kompensationsschema wird vorgeschlagen. Um eine genaue Schätzung der Hohlraumverstimmung zu erhalten, wurde ein Echtzeitverstimmungschätzer entwickelt. Diese Komponente, die für Resonanzregelsysteme erforderlich ist, wird auch für die Schätzung des Hohlraumqualitätsfaktors verwendet, um ein Quenchdetektionssystem zu realisieren. Das letzte Thema befasst sich mit der Linearisierung von Hochfrequenzverstärkern auf der Basis von Vakuumröhren, die zur Stromerzeugung der supraleitenden Kavitäten verwendet werden. Der Grund für die Durchführung einer Linearisierung dieser Verstärker ist die Verbesserung der Feldstabilität und die Vereinfachung der Setup-Prozeduren des HF-Regelsystems. Für diese Studie wurden Klystrons und IOT-Verstärker (Induction Output Tube) verwendet.

Riassunto

In questa tesi di dottorato vengono illustrate e analizzate possibili soluzioni nell'ambito dei sistemi di controllo per cavità superconduttive di modello TESLA operanti in regime continuo. L'elaborato si concentra sulle richieste necessarie per procedere all'aggiunta di una modalità di operazione continua a European XFEL accanto alla preesistente modalità pulsata. La principale sfida da affrontare dal punto di vista dei sistemi di controllo deriva dalla necessità di usare un fattore di qualità delle cavità (Q_L) in un intervallo di 10^7-10^8, un ordine di grandezza maggiore rispetto al valore usato in modalità pulsata. Di conseguenza si ha una maggiore sensibilità del tune agli effetti microfonici. Per tal motivo è richiesto lo sviluppo di soluzioni di compensazione attiva del rumore al fine di limitare i consumi complessivi del sistema accelerante, e di aumentare la stabilità energetica del fascio accelerato. Un altro effetto presente nel futuro upgrade è la presenza di instabilità ponderomotive dipendenti dall'accoppiamento nonlineare tra Lorentz Force Detuning e campo accelerante. Tali effetti sono quindi analizzati e viene proposto un possibile schema di compensazione. Al fine di ottenere una precisa stima del detuning delle cavità è stato inoltre sviluppato un sistema di calcolo in tempo reale dello stesso. Tale componente, necessario per i sistemi di controllo di risonanza, viene inoltre utilizzato per la stima del fattore di qualità delle cavità al fine di realizzare un sistema di rivelazione di quench. L'ultimo argomento trattato è la linearizzazione di amplificatori a radiofrequenza basati su tubi di vuoto necessari al funzionamento del sistema di accelerazione al fine di migliorare la stabilità e la facilità di utilizzo del sistema di controllo a radiofrequenza. Per tale studio, sono stati utilizzati amplificatori di tipo Klystron e Induction Output Tube (IOT).

Abstract

In this doctoral thesis, possible solutions for superconducting cavity control systems operating in the Continuous Wave(CW) regime are discussed and analyzed. The paper focuses on the requirements for adding a CW mode of operation to European XFEL alongside the existing pulsed mode of operation. The main challenge from a control system point of view stems from the need to use a loaded quality factor (Q_L) in the range of 10^7-10^8. Such a (Q_L) is an order of magnitude greater than the actual value that is used in the pulsed mode of operation. As a result, the cavity tune is more sensitive to microphonic effects. For this reason, active noise compensation techniques are required in order to limit the overall power consumption of the accelerating system, and to increase the energy stability of the accelerated beam. Another effect present in the future upgrade are ponderomotive instabilities. These instabilities result from the nonlinear coupling between the Lorentz force-induced detuning and the cavity acceleration field. These instabilities are then analyzed and a possible compensation scheme is proposed. In order to obtain a precise estimate of the cavity detuning, a real-time detuning estimator has been developed. This component, necessary for resonance control systems, is also used for the estimation of the cavity quality factor in order to realize a quench detection system. The last topic is about the linearization of radio frequency amplifiers based on vacuum tubes used to produce power the superconducting cavities. The reason for doing a linearization of these amplifiers is the improvement of the field stability and the simplification of setup procedures of the RF control system. For this study, Klystrons and Induction Output Tube (IOT) amplifiers were used.

Chapter 1

Introduction

Accelerator-based light sources are a discovery tool of ever-increasing importance in modern science. The ability for these facilities to generate a broad spectrum of radiation at very high brightness proved fundamental to understanding the electronic structure and properties of matter at microscopic scales. Therefore many progress in biology, biotechnology, solid-state physics, and materials engineering strongly depends on the quality of the generated light of present and future facilities. In the last fifteen years, the advancements in accelerator science and technology allowed the construction of a new kind of light source: the X-Ray Free Electron Lasers (XFEL).

Compared to storage ring-based light sources, XFELs provide a peak brilliance several orders of magnitude higher. Peak brilliance is expressed in photons/s/mm^2/$mrad^2$/$0.1\%BW$ where BW denotes a bandwidth relative to the emitted photon frequency (Fig. 1.1). XFELs also allows the generation of photon pulses with a high degree of transverse coherence and a duration in the order of $10\,\mathrm{fs}$ Full Width Half Maximum (FWHM). To generate the radiation, FELs use a relativistic electron beam passing through an undulator (Fig. 1.2).

In the undulator, the magnetic field has a periodicity along the beam trajectory and is directed in the transverse plane (Fig. 1.3). Such a magnetic configuration
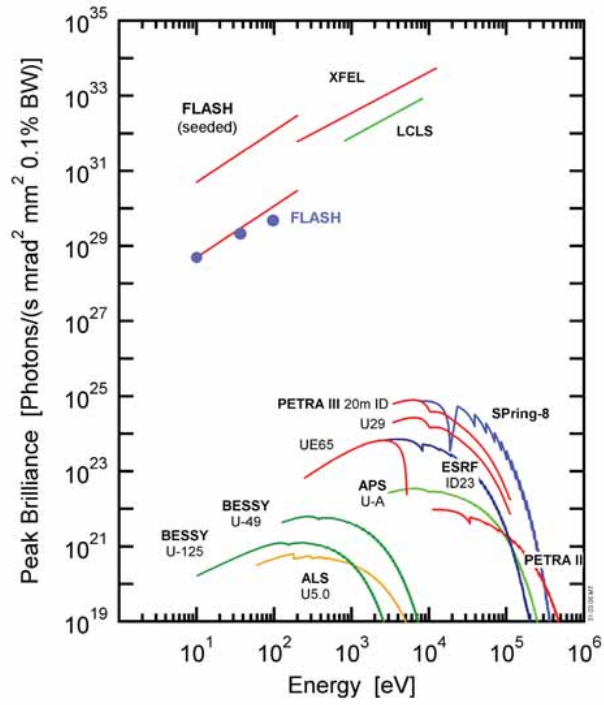
Figure (1.1)   Comparison between peak brilliance of storage rings (lower part) and XFEL based (upper part) light sources [1].

Figure (1.2)   An undulator installed at EuXFEL [2].

allows converting the kinetic energy of the electrons in high energy photons. The generated radiation has a wavelength

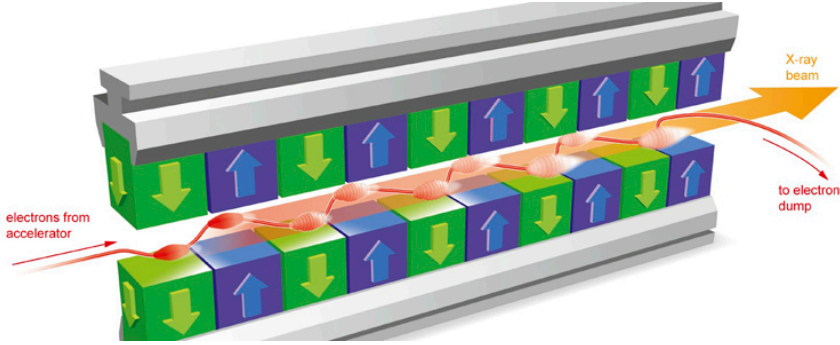$$\lambda = \frac{\lambda_w}{2\gamma^2}(1 + K^2), \tag{1.1}$$

Figure (1.3)   Scheme of an undulator [2].

with λ the photon wavelength, λ_w the undulator period, γ the Lorentz term and γmc^2 the electron beam energy. The undulator strength K is

$$(1.2)$$

$$K = \frac{eB_w\lambda_w}{2\sqrt{2}\pi mc}, \qquad (1.3)$$

with B_w the undulator magnetic field. The FEL process is the result of a collective instability happening inside the electron bunches. Such instability causes an exponential growth of the radiation intensity along the undulators line until a saturation point is reached. Depending on the saturation length, a variable number of undulators are used in an FEL beamline. The resulting properties of the generated radiation strongly depend on the electron beam parameters. The radiation growth depends on the squared number of electrons that participate in the instability process. Therefore it is of importance to maximize the peak current of the electron bunches. For typical parameters of the undulator ($K \approx 1$, $\lambda_w \approx 4\,\mathrm{cm}$) and using (1.2), the required beam energy to produce X-ray radiation spans from some hundreds of MeV to some tens of GeV. Moreover, since experiments generally require stable photon energy between radiation pulses, the acceleration process has to be tightly controlled to minimize the beam energy variations. Radio Frequency (RF) LINear ACcelerators (LINAC) are used to generate the beam for XFELs. This kind of accelerator uses RF cavities to transfer energy to the electron beam. When a bunch passes through an RF cavity, it encounters the alternating electric field, thus getting accelerated. Contrary to synchrotrons, the electron bunches in a LINAC are accelerated in a single pass to maintain the high peak current required in the FEL process. In modern hard X-ray FELs the achieved peak current is of several kA. Since the beam energy required to drive

an X-ray FEL is in the order of GeV, it is of primary importance to maximize the cavity accelerating gradient to minimize the accelerator length and construction costs. Simultaneously, experiments benefit from a high bunch production rate to speed up data collection and improve the experiment statistics. Therefore the RF duty cycle of the cavities has to be maximized. Depending on the desired beam parameters and facility cost, different technologies are used to realize RF accelerating cavities: Normal-Conducting (NC) copper cavities and Super-Conducting (SC) niobium cavities. Linear accelerators are often classified based on the kind of cavities they use. In NC accelerators, S-band and C-band cavities operated at room temperature are used. The achieved gradient in recent C-band NC cavities is higher than $38\,\mathrm{MV\,m^{-1}}$ [3]. Tests on X-band cavities also shown the possibility to realize future NC accelerators with gradients higher than $50\,\mathrm{MV\,m^{-1}}$ [4]. NC LINACs for XFELs are always operated with a duty cycle $\ll 1\%$ and RF pulse lengths in the µs scale to limit the power of RF losses by ohmic dissipation on cavity walls. Constraining the maximum power is necessary to avoid damages to the accelerating structure. Typical RF pulse repetition rates for NC LINACs are several tens of Hz (Tab. 1.1). In NC LINACs, the RF pulse length usually allows accelerating just one bunch, making the bunch repetition rate equal to the RF pulse repetition rate.

SC LINACs for XFELs use Superconducting RF (SRF) L-band cavities. These resonators are operated at a cryogenic temperature of a few Kelvins to maintain their superconducting state. Although different materials can be used to produce superconducting cavities, current and future SC XFELs use bulk niobium resonators due to the production processes maturity. The achievable SC cavity gradients are of some tens of $\mathrm{MV\,m^{-1}}$ and are strongly dependent on the superconducting material properties and fabrication treatments. The maximum theoretical gradient achievable with L-band cavities for electrons acceleration is between 50 and $60\,\mathrm{MV\,m^{-1}}$ [18]. Compared to their normal-conducting counterparts, superconducting cavities present a much lower surface resistance, allowing longer RF pulses or even Continuous Wave (CW) mode of operation without incurring a damaging RF heat dissipation. Therefore, despite having a lower gradient with respect to state of the art normal-conducting cavities, SC cavities allow generating thousands or even millions of bunches per second.

Facility (NC)	Energy (GeV)	RF pulse repetition rate (Hz)	RF pulse length (µs)	Bunches per pulse	Average gradient (MV/m)	Start of operation
LCLS	14.3	120	3.0	1	17	2009
SACLA	8	60	4.5	1	35	2011
FERMI	1.5	50	0.7	1	27	2012
PAL-XFEL	10	60	1.2	1	27	2017
SwissFEL	5.8	100	3.0	2	28	2018
SXFEL-TF	0.5	10	5.5	1	38	2019
SXFEL-UF	1.5	50	5.5	1	40	2021[*]
Facility (SC)						
FLASH	1.25	10	800	800	20	2005
EuXFEL	17.5	10	650	2700	23.6	2017
LCLS-II	4	-	-	1 MHz (CW)	16	2022[*]
LCLS-II-HE	8	-	-	1 MHz (CW)	18	2028[*]
SHINE	8	-	-	1 MHz (CW)	16	2025[*]

[*] Expected completion year

Table (1.1)   List of present and future X-ray facilities [5, 6, 7, 8, 9, 3, 10, 11, 12, 13, 14, 15, 16, 17]

1.1 Presentation of this dissertation

In this doctoral thesis, a study of various digital control techniques for the foreseen European XFEL (EuXFEL) CW/Long Pulse (LP) upgrade will be presented. EuXFEL is a superconducting FEL that works in pulsed RF mode with a duty cycle in the order of 1%. The CW/LP upgrade aims to increase the duty cycle to 10-100%. All the measurements were performed on the 1.3 GHz accelerating cavities. Even if it was not possible to test all the techniques presented in this dissertation on the third harmonic 3.9 GHz module and gun cavity due to the lack of an experimental setup, these methods will be used in future tests and are generally applicable to high loaded quality factor (Q_L) SRF resonators and their RF systems. In chapter 2 an overview of EuXFEL is given along with its existing Low Level RF (LLRF) system. In chapter 3, the CW/LP upgrade is introduced. In chapter 4, an Field Programmable Gate Array (FPGA)-based quench detection component for SRF cavities driven in CW mode is presented. Due to the cavity RF model symmetry, the component also estimates cavity detuning. The experimental results using this concept are presented in the paper "Online detuning and quench detection for superconducting resonators" [19] (published, *IEEE Transactions on Nuclear Science*). The author performed the design, implementation and test of the component in various superconducting facilities. In chapter 5, an overview of the ponderomotive instabilities is given. A method to alleviate the occurrence of the monotonic instability using integral control is analytically studied in the paper [20] "Integral Resonance Control In Continuous Wave Superconducting Particle Accelerators" (published, *IFAC-PapersOnLine*). The author contributed with the derivation of the linearized electro-mechanical cavity system, with the controller stability analysis and with the simulations and tests performed on cavities driven in CW. In chapter 6, an overview of klystron and Inductive Output Tube (IOT) nonlinearities is given. These nonlinear effects can be corrected using the predistortion method. This method is implemented as an FPGA-based component in the LLRF controller. The author contributed to the definition of a calibration procedure for such a technique and the measurement of the component linearization performance the of the amplifiers at EuXFEL, FLASH, and Cryo Module Test Bench (CMTB). The results are presented in the article "Results on FPGA-based high power tube amplifier linearization at DESY" [21] (published, *IEEE Transactions on Nuclear Science*). Finally, in chapter 7, the conclusions

are given along with an outlook of possible future improvements of the LLRF controller.

Chapter 2

Introduction to EuXFEL

European XFEL is a 17.5 GeV pulsed hard X-ray FEL located between Hamburg and Schenefeld in Germany (Fig. 2.1). At the time of writing, EuXFEL is the
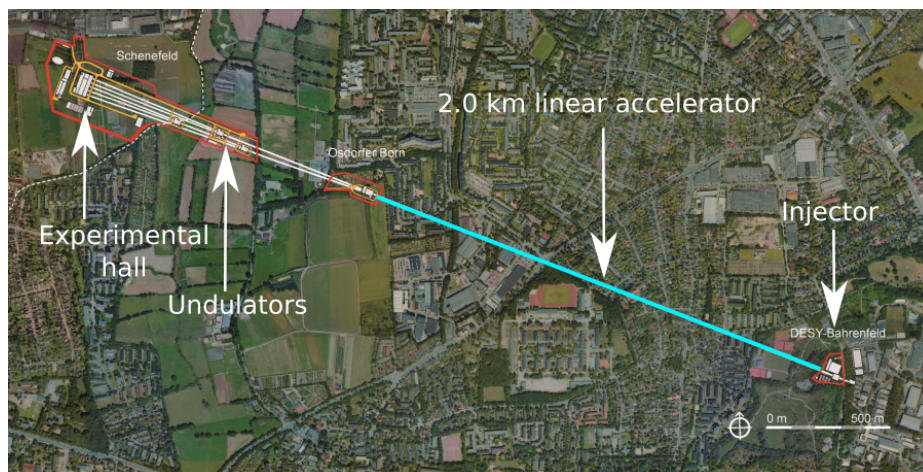

Figure (2.1) Top view of the EuXFEL location [22].

brightest XFEL worldwide with the capability of generating X-ray pulse wavelengths as short as 0.04 nm [2]. The RF pulse repetition rate of EuXFEL is 10 Hz, and the maximum amount of bunches that can be accelerated per RF pulse is 2700, thus allowing the production of 27000 light pulses per second. The generation of the electron bunches happens in an RF gun located at the beginning of the

accelerator [23]. The electron emission occurs when a UV laser pulse of 262 nm illuminates a Cs_2Te photocathode located at the bottom of the gun cavity. Then the bunch is accelerated to 6.6 MeV by the gun cavity field. When the maximum amount of bunches per RF pulse is requested, the laser is run at a repetition rate of 4.5 MHz thus resulting in a temporal spacing between bunches of 0.22 μs. The maximum bunch charge is 1 nC that is equivalent to a beam current of 4.5 mA averaged along the RF pulse. After the gun, a solenoid focuses the beam in the following acceleration stages. Then the beam is accelerated by a 2 km super-conducting LINAC with an average accelerating gradient of 23.6 MV m^{-1}. The accelerator is divided into three sections: the injector section (L1), the booster section (L2), and the main section (L3) section. Between the accelerator sections, bunch compressors are used to increase the peak current of the beam. At the accelerator end, fast kickers distribute the bunches between three undulator lines (Fig. 2.2).
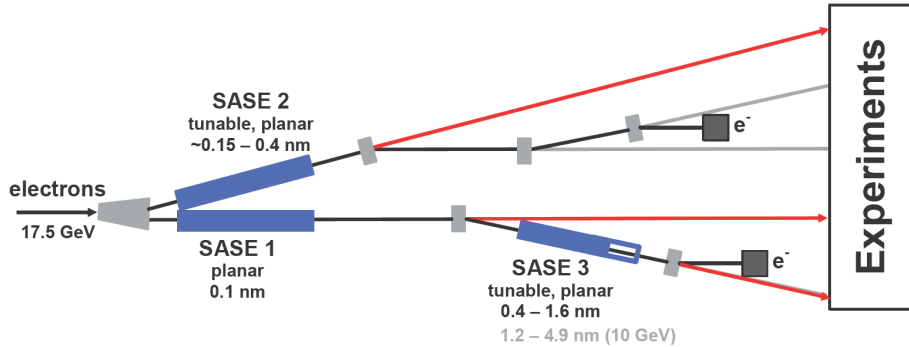

Figure (2.2)   EuXFEL beamlines [22]

The undulators in SASE1 and SASE2 produce hard X-ray pulses with wavelengths between 0.04 and 0.15 nm while SASE3 is used to generate soft X-ray light with wavelengths between 0.4 and 1.0 nm [22]. Variable-gap undulators in SASE2 and SASE3 allow flexibility in choosing the generated wavelength in each beamline. The generated radiation is then transported and distributed to six instruments in the experimental hall. Two additional tunnels are left for the installation of future FEL beamlines and experiments.

In the accelerator 776 cavities of the TESLA-type [18] (Fig. 2.3) are used to accelerate the beam. These cavities operate in the L-band with a resonance frequency of 1.3 GHz, and they are cooled at 2 K by a superfluid helium bath. The cavities are housed in modules that provide mechanical support, thermal isolation,

Figure (2.3)   Picture of a TESLA cavity.

and vacuum and cryogenic piping. Each module contains eight cavities and other devices like quadrupoles, correctors, and Beam Position Monitors (BPM). Four modules are grouped in a single RF station and controlled using the Vector-Sum (VS) scheme. Therefore a single high-power pulsed klystron provides the required RF power for all the cavities within an RF station [24]. The control system then controls the stability of the sum of the accelerating voltages of the 32 cavities within an RF station.
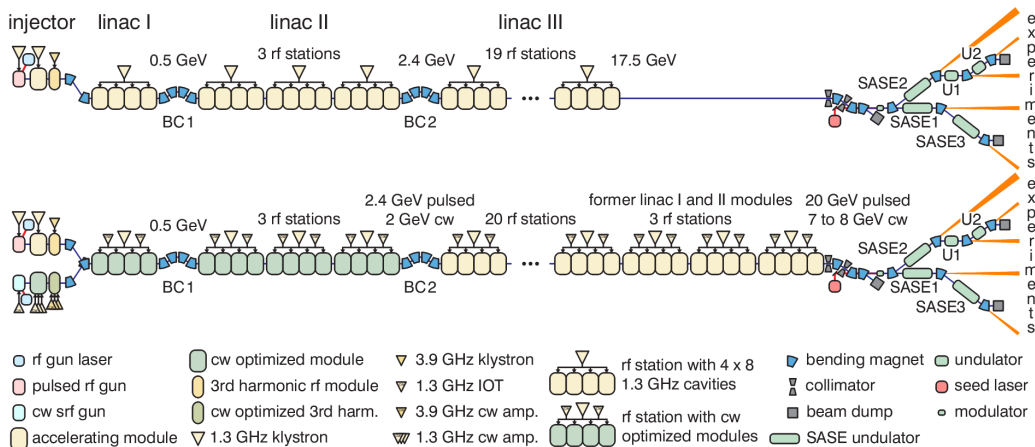

Figure (2.4)   Scheme of EuXFEL before (top) and after (bottom) the CW/LP upgrade [25]

In total, 25 stations are installed at EuXFEL: 1 in the L1 section, 3 in the L2 section, 21 in the L3 section (Fig. 2.4 top). Additionally, EuXFEL has a third harmonic module equipped with eight superconducting cavities [26] with a resonance frequency of 3.9 GHz and an additional accelerating module with TESLA cavities right after the gun [27]. The third harmonic module is used to
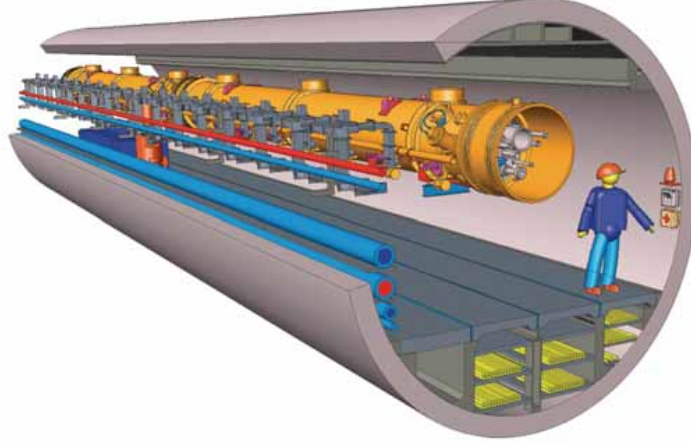
correct the bunch curvature and remove beam tails.

Figure (2.5)   3D drawing of the EuXFEL tunnel [28]

The LINAC is installed in a single tunnel $15 - 30\,\mathrm{m}$ underground with a diameter of $5.2\,\mathrm{m}$ (Fig. 2.5). Since there no service tunnel, every piece of supporting equipment for the LINAC was carefully designed to fit into the accelerator tunnel.

2.1   The LLRF control system

To generate stable high-brilliance FEL radiation at EuXFEL, the error on the accelerating voltage amplitude and phase of an RF station has to be smaller than 0.01% RMS and $0.01°$. Therefore, the LLRF system that controls the station must meet these demanding requirements. Additionally, the LLRF system has to catch eventual anomalies or failures in the accelerating system and execute proper actions to minimize the accelerator downtime or prevent damages to the facility [29, 30]. The LLRF system should also allow to monitor and measure the status of the accelerating cavities. Finally, the LLRF system controls the resonance frequency of the cavities against mechanical disturbances to minimize the RF power required to generate the accelerating gradient. Such a task is performed using mechanical tuners that act on the cavity geometry thus modifying the resonance frequency. All the LLRF systems parameters have to be accessed through a high-level interface that abstracts the low-level details of the control system. Since EuXFEL lacks a service tunnel and the LLRF is installed next to the accelerator, there are additional constraints to be fulfilled:

1. The LLRF system must be highly reliable since shutting down the entire facility is required to repair a single system.

2. Since the LLRF crates are positioned right below the accelerator, the electronics have to be radiation-tolerant. Radiation-aware design, radiation shielding, self status check, and automatic correction of radiation generated errors [31] (e.g., bit-flip in memories) are required.

3. For the same reason expressed in point 2., the time to repair or modify the LLRF system hardware has to be minimized. Moreover, the required tools to perform the maintenance operations have to be kept to the minimum and have to be easily transportable through the tunnel. Therefore, a standardized plug-and-play modular form factor has to be used for the LLRF system electronics.

4. The LLRF system firmware and software must have the possibility to be configured and upgraded remotely.

5. The limited available space in the tunnel requires that the LLRF system size is kept to the minimum.

6. VS cavity control requires the RF signals of up to sixteen cavities to be managed by a single LLRF crate. Therefore the LLRF system needs to have a high count number of RF ADC channels.

7. The LLRF system has to correct for environmental disturbances that happen in the tunnel. These variations include changes in the RF electronic calibration due to seasonal or day/night variation in tunnel humidity or temperature

Finally, since the EuXFEL accelerator is 2.0 km long, a sophisticated RF synchronization system is required to keep the RF reference of the LLRF system stable against drifts at a femtosecond level [33, 34]. Therefore the LLRF needs low-noise interfaces for synchronization purposes. For these reasons, the LLRF controller EuXFEL is implemented with the Micro TCA technology (MTCA.4) standard [35, 36, 37]. Apart from the MTCA.4 crate, the following custom modules are installed in the LLRF racks:
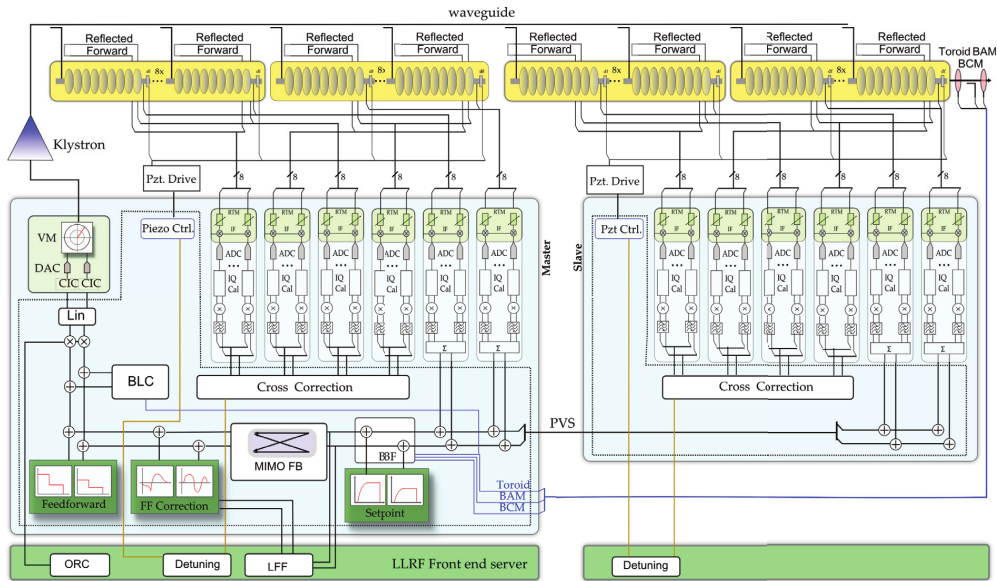
Figure (2.6)   Scheme of the EuXFEL LLRF system [32]. Two LLRF racks work in a distribuited way and are connected via an optical link. The system is able to manage all the 32 cavities in an RF station.
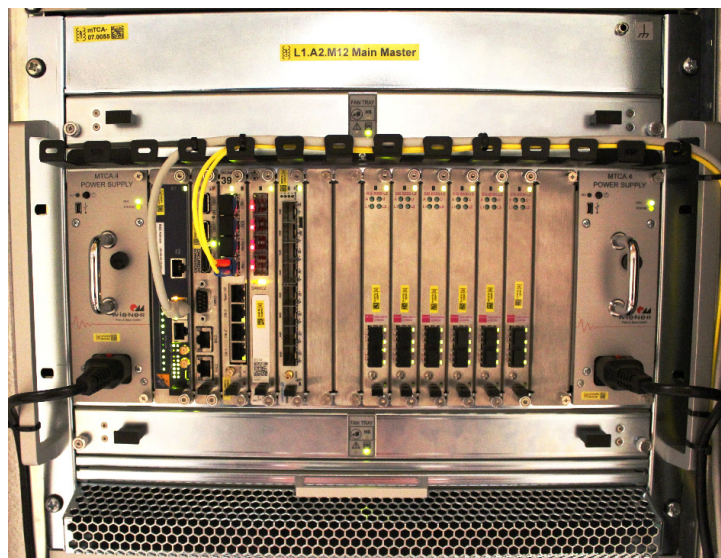

Figure (2.7)   MTCA.4 LLRF crate installed at EuXFEL.

- **REFM-OPT** : Optical synchronization unit based on a Mach-Zehnder interferometer. REFM-OPT locks a 1.3 GHz RF reference signal to the Master Laser Oscillator (MLO).

- **DCM** : Drift Calibration Module. This module corrects for variations in

the RF measurement chain of probe signals. A reference signal is injected before each pulse, thus allowing the precise tracking of drifts in the ADCs.

- **LOGM** : The LO Generation Module uses the 1.3 GHz RF reference signal from the REFM to generate other RF and clock signals used in other parts of the LLRF system.

- **PZ16M** : This is the piezoelectric tuner driver module, and it is capable of handling the actuator and sensor signals of up to 16 cavities. The drive voltage range is +/- 70 V with a bandwidth of 20 kHz. This module is connected to the MTCA.4 crate through an optical link.

- **CPIM** : LLRF coupler processinng interlock module, preventing excitation of the cavities at room temperature.

- **PSM** : The Power Supply distribution Module is a fully redundant power supply for the REFM, LOGM, and DCM. The diagnostic data of this module is accessible over an ethernet connection.

Fig. 2.6 depicts the complete LLRF scheme for EuXFEL. For further informations see [36].

For each RF station, there are a master and slave rack that work in a distributed manner. Since for the VS mode of operation, the sum of the probe signals within an RF station is required for control purposes, the MTCA.4 crates in the two racks compute the partial vector sum of 16 cavities each. Then, the slave MTCA.4 crate sends its partial vector sum value to the master crate through an optical link. The master crate uses this information to compute the final VS value and to generate the station klystron control signal.

2.2 The MTCA.4 LLRF control crate

The MTCA.4 is an open standard for a modular crate form factor directly derived from the Advanced Telecommunication Computing Architecture (ATCA)

standard. Due to the modularity of MTCA.4 and the availability of several commercial off-the-shelf MTCA.4-compliant cards, it is possible to customize the crate depending on the target application. In the EuXFEL LLRF system, the front modules or Advanced Mezzanine Carriers (AMC) are used to perform digital signal processing, whereas the rear modules or Rear Transition Modules (RTM) are used for analog signal processing. Each RTM is paired with an AMC and communicates with it through a connector (referred to as Zone3). In the RTM side, an RF backplane is used to share RF signals and clocks between the modules. In the AMC side, a backplane provides multiple channels in different commonly used high-speed digital communication standards such as PCIe, Gigabit Ethernet, and RapidIO. Customized point-to-point connections also allow direct low-latency high-speed data transfer between different AMCs. Additional lines on the AMC backplane are reserved for custom clock signals and future standard extensions. The standard MTCA.4 module composition for an accelerating RF station of EuXFEL is the following [37]:

- **uDWC** : The down converter RTM board converts RF signals from $1.3\,\mathrm{GHz}$ to the Intermediate Frequency (IF) of $54\,\mathrm{MHz}$. Each board has ten available channels with a programmable attenuation between 0 and $30\,\mathrm{dB}$.

- **SIS8300** : SIS8300 is an ADC AMC board that is paired with the DWC. It samples the signals that come through Zone3 at a rate of $81.25\,\mathrm{MHz}$ and convert them in an In-phase and Quadrature (I&Q) signals. The board is equipped with a Xilinx Virtex 6 Field Programmable Gate Array (FPGA) to perform fast Digital Signal Processing (DSP) calculations on the sampled signals. These calculations comprise delay adjustment, I&Q signal rotation and scaling, drift compensation using the DCM reference signal, and the filtering of the $8\pi/9$ cavity mode signal. The partial vector sum calculation is also performed on this board at a rate of $9.027\,\mathrm{MHz}$ and sent to the main controller board (uTC). In total, 8 ADC channels are used to sample cavity signals. Therefore, since for each accelerating cavity, a probe, a forward, and a reflected signal are digitized, 6 SIS8300 boards are installed in each crate to sample the signals produced by 16 accelerating cavities.

- **uTC** : uTC is the main controller AMC in the LLRF crate. This compenent is based on the DAMC-TCK7 and is equipped with a Xilinx Kintex 7 FPGA

to perform fast DSP calculations. For a slave crate, it just generates the partial VS signal using the data from the SIS8300 and sends it to the master crate. The uTC in the master crate computes the total VS value using the received value and the data from the SIS8300 boards. An error signal is generated by subtracting the rescaled VS with a setpoint. Gradient limiters and beam-based feedback components for bunch arrival stabilization also contribute to the final value of the error signal [38, 39]. Additionally, it is possible to add setpoint tables to the measured error to generate arbitrary RF pulse shapes over time. This feature is needed to define the gradient trajectory during filling and to produce multiple flattop regions to accelerate the beam at different energies within a single RF pulse. A fourth-order Multiple-In Multiple-Out (MIMO) feedback controller then uses the error signal to generate the control value [40, 41]. The feedback also corrects the effects produced by the $7\pi/9\pi$ cavity mode since it impacts beam acceleration. The feedback controller can be disabled when only a feedforward drive of the cavities is needed. Feedforward signals are then added to the feedback one. Look-Up Tables (LUT) are used to store the feedforward data. The FeedForward (FF) correction is filled with the precomputed RF drive signal calculated offline using a cavity model. FF is necessary to minimize the control effort of the feedback section, thus improving the system stability. The Beam-Loading Compensation (BLC) table corrects for beam-induced gradient variations. Finally the Learning FeedForward (LFF) table is adaptively updated using an Iterative Learning Control (ILC) algorithm. LFF is used to correct for pulse-to-pulse recurrent errors. Finally, the resulting control value is scaled and corrected to compensate for DAC offsets. The complete signal processing diagram is shown in Fig. 2.8. The output is also checked with limiters to prevent overdriving the klystron. Then the IQ drive signal is sent to the uVM RTM board through Zone3.

- **uVM** : The uVM RTM performs a single sideband modulation of the control signal to generate the 1.3 GHz klystron drive signal. The uVM also embed a fast RF gate for the interlock system and a programmable attenuator.

- **KLM** : The Klystron Lifetime Management (KLM) is based on the SIS8300L AMC and a uDWC RTM. The KLM uses the sampled input and output RF signals of the klystron and cathode voltage and current values to detect possible damaging events, like sparks or loss of vacuum [42]. When an event is

detected, the KLM triggers the crate backplane interlock line, thus switching off the klystron drive.

- **uCPU** : The uCPU is based on Concurrent Technologies AM 902/411-52 board. This module holds an x86-64 processor attached to the PCIe and Gigabit Ethernet interface of the AMC backplane. The uCPU software has the responsibility to handle the communication between the MTCA.4 boards and the higher-level layers of the control system. The uCPU software also configures the registers on the boards and exposes an abstracted interface of the hardware capabilities. The uCPU software has a server-based architecture based on the ChimeraTK [43] framework. Each server takes care of different aspects of the system. The LLRF control server manages the feedback and feedforward parameters, sets the system control tables, and provides the interface to read the cavity RF signals. The diagnostic server monitors the cavities quality factor (Q_L). Such a task is needed to check whether a quench or other unwanted effects have happened on the accelerating cavities. The piezo server calculates the compensation that must be applied to each cavity tuner to correct for resonance drifts and Lorentz Force Detuning (LFD) effects. The servers parameters are accessed through the Distributed Object-Oriented Control System framework (DOOCS) [44].

- **TMG** : X2Timer is a timing board that provide the trigger signals, like the pulse start signal, to the other boards [45].

- **MPS** : The Machine Protection System (MPS) board is responsible for collecting and propagate interlock signals to other boards with low latency. Fiber-optic connections are used to avoid electromagnetic interference in the propagation of the signals. Once an interlock condition is raised, the MPS board can stop the generation of RF pulses. The safety systems of the accelerator are attached to this board(e.g., pressure and temperature signals, Beam Loss Monitor (BLM) signals, and magnet current readouts) [46].

- **MCH** : The MCH provides the switching-capabilities for the Gigabit Ethernet, Rapid IO, and PCIe AMC backplane channels. It also monitors the initialization status of the MTCA.4 crate boards.

Fig. 2.9 shows how the boards are distribuited in the MTCA.4 LLRF crate.
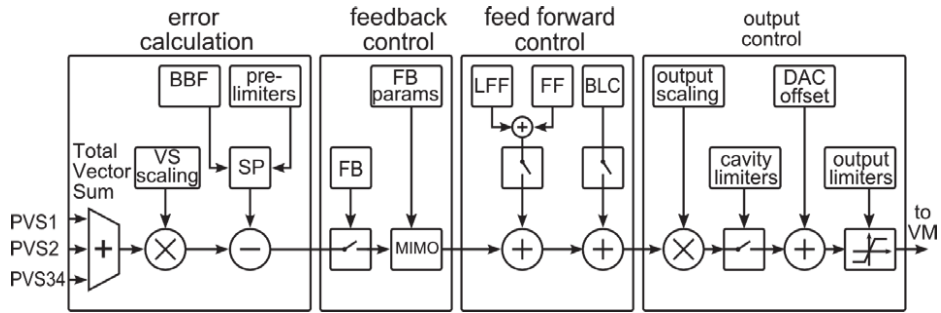
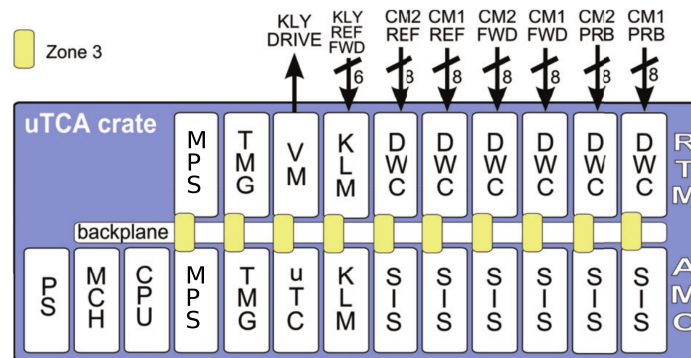Figure (2.8)   Top level diagram of the uTC FPGA digital signal processing [37].

Figure (2.9)   Top view of the MTCA.4 board distribution [36].

The third harmonic module uses a variation of the presented configuration: the uDWC is modified to operate at 3.9 GHz and its MTCA.4 crate is shared with the control boards of the accelerating module installed after the gun.

Chapter 3

The EuXFEL CW/LP upgrade

Due to the separation of just $0.22\,\mu s$ between electron bunches, data acquisition, data pre-processing, and data storing are among the most challenging aspects of the EuXFEL experiments. Despite the latest developments in detector technology and high-speed image processing techniques [45, 47, 48, 49], many user experiments would benefit from an increased FEL pulse separation. A longer separation can be accomplished by lowering the bunch repetition rate. However, to mantain the same amount of bunches per second, the RF pulse length has to be increased. Further increasing the RF pulse duty factor might also allow a higher number of bunches per second, thus speeding up the experimental data acquisition. For these reasons, a possible CW upgrade of EuXFEL is under discussion [50, 51]. After the upgrade, the EuXFEL LINAC will be able to generate a CW beam with a charge of 250 pC at a bunch repetition rate of 100 kHz. It is also foreseen to operate the accelerator with a bunch repetition rate of 1 MHz at a reduced bunch charge. The L3 section will be operated with a maximum CW gradient of $7\,\mathrm{MV\,m^{-1}}$ to limit the cavity dissipation at a reasonable level. The expected final beam energy for the CW mode 8 GeV. Generating higher energy semi-CW beams will be also possible, by reducing the pulse duty factor at a level between 10%-50%. Possible beam parameters for the EuXFEL CW upgrade are listed in Tab. 3.1. Sekutowicz et al. [50] proposes to scale the gradients proportionally to $(7/E_{acc})^2$ to keep the cryogenic heat load constant. This reduced-duty mode of operation is called Long

Pulse (LP) mode to differentiate it from the actual EuXFEL Short Pulse (SP) mode which has a duty factor of 1.4% (Fig. 3.1). Due to the lower beam energies produced in CW and LP mode, a requirement for the EuXFEL upgrade is to keep the existing SP mode of operation. Therefore, depending on the experimental program to follow, the machine has to be configured to SP or (CW/LP) mode. Only remote setup procedures must be required to switch the accelerator between the available modes of operation to minimize machine downtime.
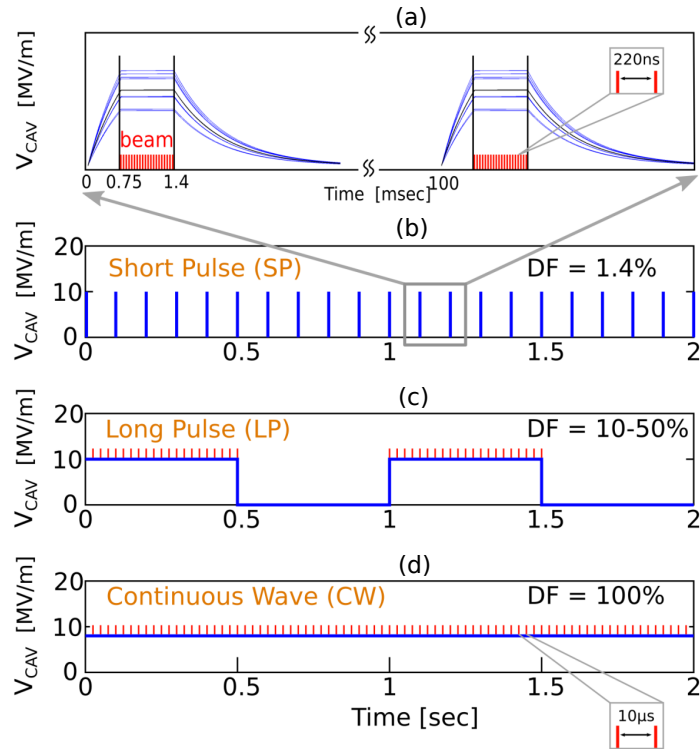

Figure (3.1)   RF pulse shape (blue trace) for the SP (b), LP (c) and CW (d) mode of operation. (a) is the detailed view of a pulse in SP. The red lines correspond to accelerated bunches [52].

As mentioned in the previous sections, a constrain in the accelerator tunnel is given by the limited available space. Therefore, future installations for the CW/LP upgrade must be carefully optimized in size. The upgrade will also require modifications or the substitution of some of the existing LINAC components.

Gun   The actual NC gun is not suitable for CW/LP operation due to the thermal load constraints. Therefore active research is ongoing to produce a new CW gun design. The actual NC gun will be kept to maintain the EuXFEL SP capabilities.

Mode	SP[*]	SP[**]	CW	LP	LP
Energy (GeV)	17.5	20	8	10	14
E_{acc} (MV m^{-1})	23.5	23.5	7[***]	10[***]	15[***]
RF pulse length (ms)	1.38	1.38	-	350	150
RF Repetition rate (Hz)	10	10	-	1	1
Duty factor (%)	1.38	1.38	100	35	15
Bunches per second	27000	27000	100000	35000	15000

[*] Before the upgrade.
[**] After the installation of additional stations in L3.
[***] In L3.

Table (3.1)   Example parameters for the different mode of operation foreseen for the EuXFEL upgrade [50]. The considered bunch charge is 250 nC at a repetition rate of 100 kHz.

The new gun, along with a dedicated third harmonic and accelerating module, will be installed in the second gun cave. Since SC CW guns enable the generation of bunches with lower thermal emittance and higher peak current with respect to CW NC guns, a superconducting photoinjector is under study at DESY [53, 54, 55, 56, 57, 58]. The new gun design has 1.6-cell TESLA-like cells and operates in the L-band. The target specifications for the generated beam for this gun are a bunch charge of $20 - 250$ pC, a peak cathode gradient of $40 - 60$ MV m^{-1}, a bunch energy at the exit of the gun of $3 - 4$ MeV, a transverse emittance of ≈ 1 µm rad and a bunch length of few ps. The new gun has a lead photocathode to minimize cross-contamination effects with the cavity walls and improve durability and quantum efficiency in respect to bulk niobium. Challenges remain in adapting the existing SRF cavity fabrication processes and components (e.g., RF antennas, tuning systems, cryomodules) to the SC gun design. Future tests are foreseen to measure the SRF gun parameters. As a backup option to the SRF gun, a CW NC gun operating in the VHF-band is also considered [59].

Gun/L1/L2 high Q_0 accelerating modules   Due to beam dynamics constraints, the beam energy has to be at least 2 GeV at the beam compressor BC2. Therefore the accelerating cavities of L1, and L2 will be operated in CW at gradients up to 16 MV m^{-1} to fulfill this requirement. Using a significantly higher CW gradient in the first part of the accelerator than in L3 requires the exchange of the accelerating modules. The key reason to exchange the modules is the cavity

23

dissipated power [60]

$$P_c = \frac{V_c^2}{\frac{r}{Q}Q_0},$$ (3.1)

$$V_c = LE_{acc},$$ (3.2)

with L the cavity accelerating length, E_{acc} the cavity gradient, V_c the cavity voltage, $\frac{r}{Q}$ the ratio between the shunt resistance and the quality factor and Q_0 the *intrinsic quality factor* of the cavity.
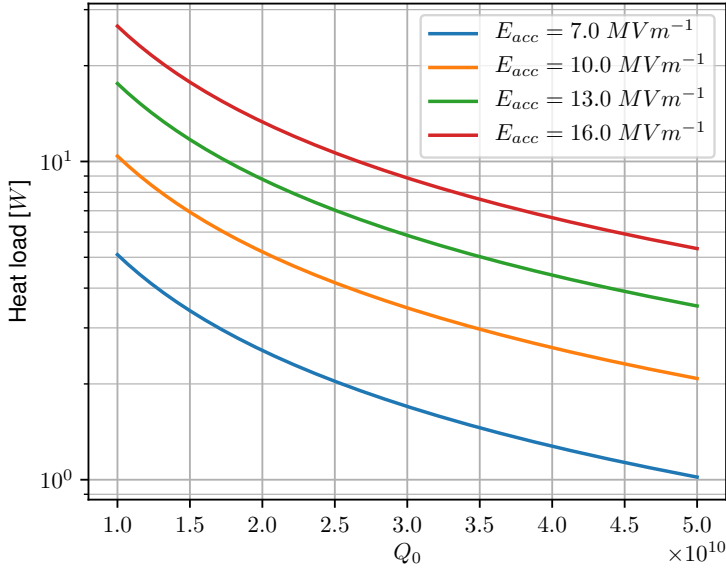

Figure (3.2)   Cavity heat load in function of Q_0.

The ratio $\frac{r}{Q}$ is dependent only on the cavity geometry, and for the TESLA cavities is equal to $1036\,\Omega$ while the RF length L is $1.038\,\mathrm{m}$ [18]. The quality factor Q_0 depends on the resistivity of the cavity walls, which in turn is influenced by temperature, magnetic fields, surface chemistry, and the accelerating gradient. For state of the art TESLA cavities, $Q_0 > 10^{10}$. Having cavities with high Q_0 values is essential to reduce the cryogenic power needed to operate the accelerator (Fig. 3.2). Therefore current research on SRF cavity fabrication processes is focused on improving this parameter. Due to the increased heat load after the CW/LP upgrade, the current cryogenic plant refrigeration power at $2\,\mathrm{K}$ has to be doubled from its actual value of $2.5\,\mathrm{kW}$ and represents the primary cost driver for the project [61]. For the same reason, it is expected to replace the accelerating

modules in L1, L2, and the injector with ones with higher Q_0 resonators. The idea is to install cavities that have a $Q_0 > 2 \cdot 10^{10}$ at $16\,\mathrm{MV\,m^{-1}}$ and, at the same time, are able to sustain the substantially higher gradients of SP mode [62, 63, 64]. Due to heat load in CW, it will also be necessary to modify the module cryogenic distribution system to increase the helium heat transport limit to more than $20\,\mathrm{W}$ per module [61].

Another aspect to take into account is the required RF power per cavity. From [65]

$$V_g \simeq 2\sqrt{\frac{r}{Q}Q_L P_g}, \tag{3.3}$$

$$V_b \simeq I_b \frac{r}{Q}Q_L, \tag{3.4}$$

$$V_c = V_g - V_b, \tag{3.5}$$

$$\tag{3.6}$$

for a cavity driven at its resonance frequency with a beam accelerated on crest. P_g is the generator power, V_g is the induced generator voltage, I_b is the beam current, and V_b is the induced beam voltage. The *loaded quality factor* Q_L is the quality factor of the cavity when coupled with an external transmission line and is dependent on Q_0

$$\frac{1}{Q_L} = \frac{1}{Q_0} + \frac{1}{Q_{ext}}. \tag{3.7}$$

Q_{ext} represents the fraction of RF power that is emitted by the cavity through the coupler in respect to the stored energy and related to how strongly the resonator is coupled to the transmission line. For superconducting cavities in accelerators $Q_0 \gg Q_{ext}$. Therefore for (3.7) $Q_L \simeq Q_{ext}$. Solving (3.3), (3.4) and (3.5) for P_g gives the required generator power that has to be provided to the cavity.

$$P_g = \frac{(V_c + I_b \frac{r}{Q}Q_L)^2}{4\frac{r}{Q}Q_L}. \tag{3.8}$$

The optimal Q_L that minimizes the generated power can be calculated with

$$\frac{dP_g}{dQ_L} = 0. \tag{3.9}$$

Which gives the optimal Q_L

$$(Q_L)_{opt} = \frac{V_c}{I_b \frac{r}{Q}}. \tag{3.10}$$

For the EuXFEL CW/LP upgrade $I_b = 25\,\mu\text{A}$ and $V_g = 16.6\,\text{MV}$. Therefore (3.10) would give a $Q_L \simeq 6.4 \cdot 10^8$. However for these high Q_L values the effect produced by mechanical disturbances have also to be taken into account. Therefore (3.10) has to be modified to include these effects [66].

$$(Q_L)_{opt} = \left[\left(\frac{I_b \frac{r}{Q}}{V_c}\right)^2 + \left(\frac{2\delta f}{f}\right)^2\right]^{-2}. \tag{3.11}$$

In (3.11) δf is the *standard deviation* (STD) of the difference between the cavity resonant frequency and the frequency of the drive signal. Assuming a conservative value of $\delta f = 5\,\text{Hz}$ the optimal Q_L is $1.6 \cdot 10^8$ [67, 68].
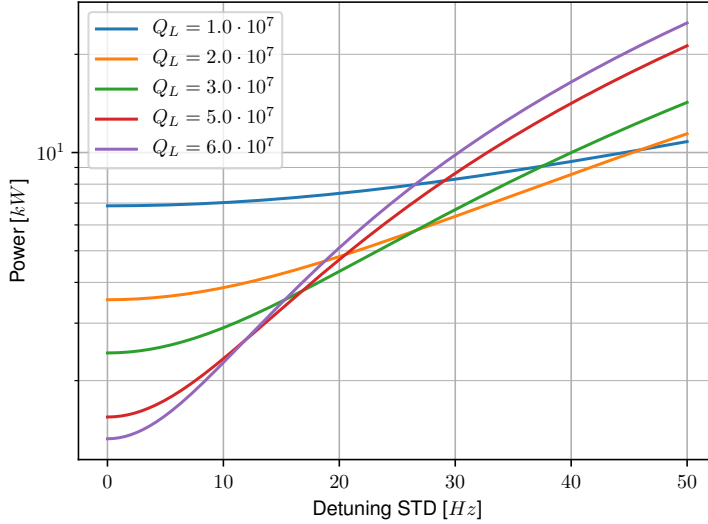

Figure (3.3)   Required cavity RF power in function of detuning STD at different Q_L values. $E_{acc} = 16\,\text{MV}\,\text{m}^{-1}$

Even if these results suggest that it is possible to use a $Q_L > 10^8$, further limitations reduce the maximum usable Q_L value. First, reaching $Q_L > 10^7$ requires a modification of the actual cavity field couplers to increase their operational
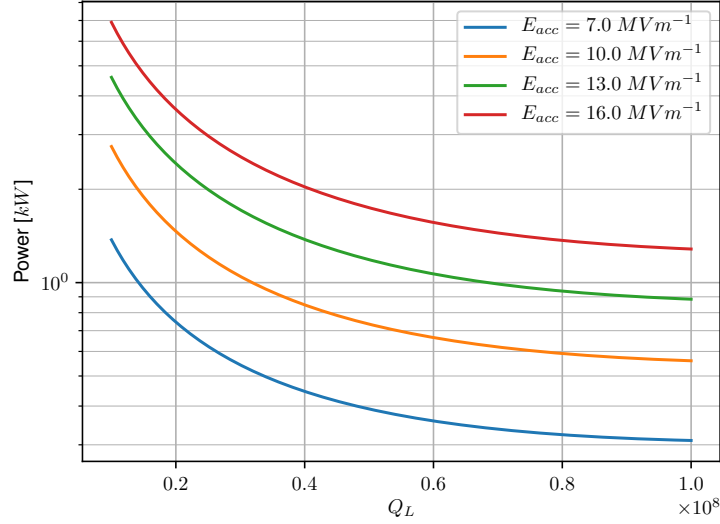
Figure (3.4)   Required cavity RF power in function of Q_L at different gradient values. $\delta f = 5\,\text{Hz}$.

range [61]. At the same time it should be still possible to reach a $Q_L = 4.6 \cdot 10^6$ to operate the accelerator in SP mode. The latest developments suggest that the maximum reachable Q_L with modified couplers is in the order of $8 \cdot 10^7$. Then the EuXFEL requirements on the stability of the accelerating field have to be taken into account. Having a high Q_L reduces the cavity bandwidth, thus making it more sensitive to low frequency microphonic mechanical excitation and harder to control (Fig. 3.3). Finally, for $\delta f = 5\,\text{Hz}$, there is a small gain in going at $QL > 6 \cdot 10^7$ since the required power decreases at a slower rate. (Fig. 3.4). For the foreseen parameter for the EuXFEL CW/LP upgrade every cavity will need $P_f > 1.5\,\text{kW}$.

Other modifications to the cavity couplers will improve the thermal dissipation to avoid overheating the inner conductor. Limiting coupler heating is also important from the LLRF point of view since tests show that thermal expansion of the inner conductor results in a Q_L variation of more than 10%. Fig. 3.5 shows the effects of RF-heating on the cavity coupler.

L3   The L3 part of the LINAC will be extended with the replaced modules in L1 and L2. In total, 12 accelerating modules will be added to the end of L3, making
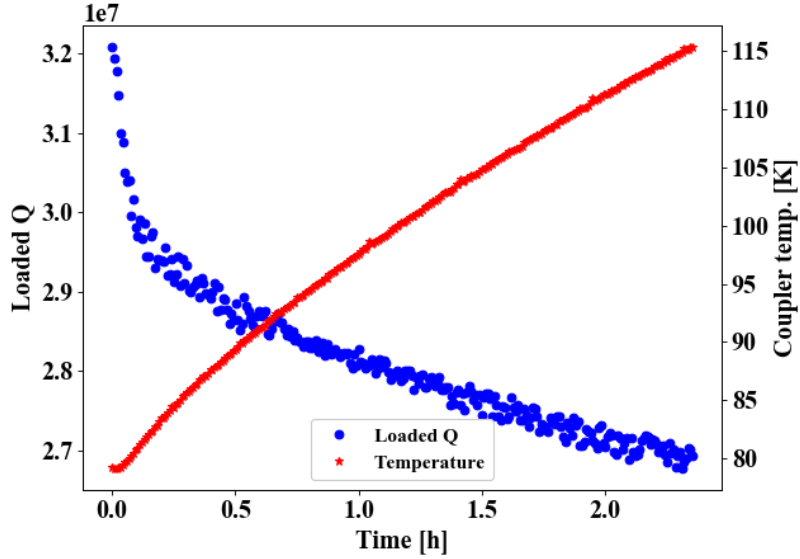
Figure (3.5)   Dependence of Q_L on coupler temperature. The heated coupler, increases its cavity penetration thus increasing the RF coupling. The Q_L drops consequently. The test was done with $P_f = 4\,\text{kW}$.

it possible to reach 20 GeV in SP mode. Since the cavity couplers in L3 will not be modified, the maximum Q_L will be limited to 1-1.5 · 10^7. This will result in a required RF power per cavity of $P_f \approx 1.3\,\text{kW}$.

The complete layout of EuXFEL after the CW/LP upgrade is depicted in (Fig. 2.4).

3.1   LLRF topics for the EuXFEL CW/LP upgrade

The EuXFEL CW/LP upgrade will require substantial modification and improvements to the RF/LLRF system.

RF amplifiers   The actual high power pulsed RF amplifiers are not suitable for continuous operation. Therefore new CW power sources have to be installed in the tunnel.
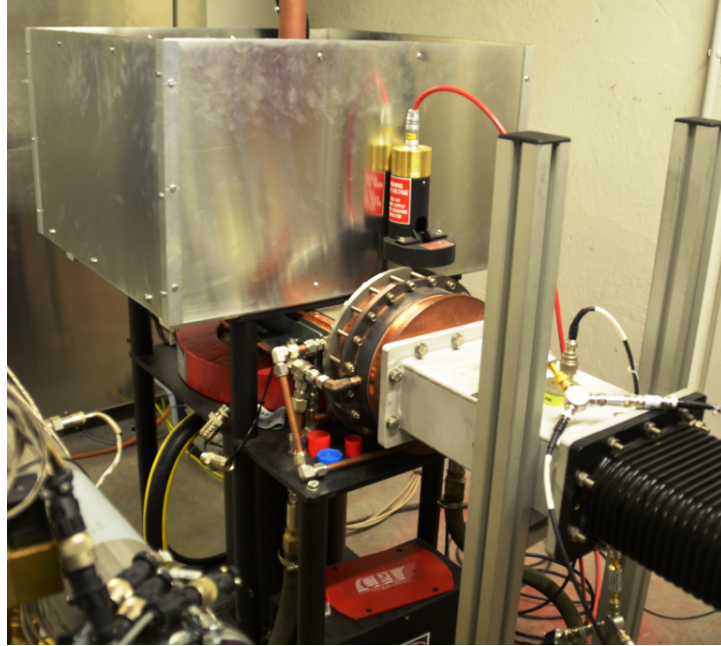
Figure (3.6)   120 kW IOT installed at CMTB [69]

For the upgrade it is planned to use one 120 kW IOT every two accelerating modules [50] (Fig. 3.6). The maximum available power per resonator with this amplifier will be 7.5 kW thus fulfilling the forward power requirements of the CW and LP mode. The RF distribution system will be modified with remotely switchable circulators to select either the SP(klystron) or CW/LP(IOT) power source. Since the input-output characteristics of IOTs are nonlinear, the LLRF system has to correct for these effects to maximize the accelerating field stability. Due to the addition of a different kind of RF power source, the KLM module has to be extended to diagnose the status of the IOT and catch eventual damaging events.

Quench detection   Since quenches can significantly increase heat load, it is of uttermost importance in every superconducting accelerator to stop the RF drive once a quench has happened to avoid releasing additional heat to the cryogenic bath. For the pulsed mode of operation, cavity quenches are caught looking at the field decay. When the forward power is switched off, the cavity voltage follows

an exponential curve

$$V_c(t) = V_c(t_d)e^{-\frac{t-t_0}{\tau}}, \tag{3.12}$$

$$\tau = \frac{Q_L}{2\pi f} \tag{3.13}$$

In the above equation t_0 indicates the start of decay phase while τ is the *decay time*. Then using (3.7) and assuming that Q_{ext} does not change, if the cavity Q_0 drops due to a quench, the decay time decreases as a consequence. Therefore a threshold-based interlock system that looks at the value of τ for each RF pulse can be used to detect quenches. Even though (3.12) can still be applied in LP mode of operation, a different approach has to be found for CW mode of operation. Moreover, a CW quench detection system has to discriminate between real quenches and gradient drops produced by other means (e.g. detuning).

Detuning estimation As shown in Fig. 3.3, detuning increases its effect on cavity gradient at increased Q_L. It is then essential to keep the cavity detuning low. A measure of the impact of detuning on the cavity gradient is given by

$$y = \frac{\Delta f}{f_{(1/2)}}, \tag{3.14}$$

with Δf the cavity detuning and $f_{(1/2)}$ the cavity half bandwidth

$$f_{(1/2)} = \frac{f}{2Q_L}. \tag{3.15}$$

For a cavity with $I_b = 0$ and constant detuning, the accelerating voltage is

$$V_c = \frac{V_g}{\sqrt{1 + y^2}}. \tag{3.16}$$

From 3.16 for $y \ll 1$ the resulting accelerating voltage is $V_c \simeq V_g$ while for $y \gg 1$ the voltage scales as $V_c \simeq \frac{V_g}{y}$. Therefore y has to be kept below the unity to avoid excessively increasing V_g and, consequently, P_f. Correctly estimating Δf is then essential to minimize RF power consumption. In the SP mode of operation, the detuning disturbance is mainly driven by repetitive LFD caused by the accelerating field radiation pressure on cavity walls. Consequently, estimation algorithms are run offline during the time between two RF pulses [70]. For CW

mode of operation, the detuning is produced by external mechanical microphonic disturbances and ponderomotive instabilities. These effects are independent of the machine timings and the detuning. The LLRF system has then to estimate the detuning online. For this, the estimation delay has to be kept shorter than the time period of the highest frequency microphonic component to avoid excessive signal phase shifts in the computed values. Since the microphonics spectrum in CW mode goes up to some hundreds of hertz[68] an estimation delay shorter than 1 ms is required. Although the detuning excitation is mainly driven by the periodic RF pulse train in LP mode, microphonic and ponderomotive disturbances still must be taken into account due to the small bandwidths involved.

Resonance control One of the most challenging aspects of the EuXFEL CW upgrade is resonance control. For the expected Q_L value in L1 and L2, $f_{(1/2)} =$ 10.8-65 Hz. As a consequence, given a static longitudinal tuning sensitivity of 315 kHz mm^{-1} for TESLA cavities, a deformation of few tens nanometers can significantly affect the cavity accelerating gradient [71]. This requires that even the smallest detuning effect has to be taken into account to maintain the cavity at the desired resonance frequency. Additionally, since the exact parameters that determine the cavity mechanical dynamics are not well known and vary from resonator to resonator, the analysis and correction of time-varying detuning signals should take into account uncertanties in the cavity model [72, 73] (Fig. 3.7).

Detuning signals have different characteristics depending on the source of origin:

A slow-varying detuning contribution is caused by the cooling system. Since the helium bath has a stability of ± 0.1 mbar [74] (Fig. 3.8) and the cavity pressure sensitivity is 50 Hz mbar^{-1} [75], the amplitude of the resulting detuning is 5 Hz. The spectrum of this detuning source is in the sub-Hz region. Other microphonics sources are rotary machines that operate next to the accelerator. Vacuum pumps and cooling fans are examples of these detuning sources. These detuning sources produce a sinusoidal excitation with fixed frequency that can include additional higher-order harmonics. The spectrum for this kind of disturbance is composed of narrow peaks with frequencies in the range of 1-100 Hz. Additional large-bandwidth noise, mostly gaussian distributed, has an amplitude in the order of
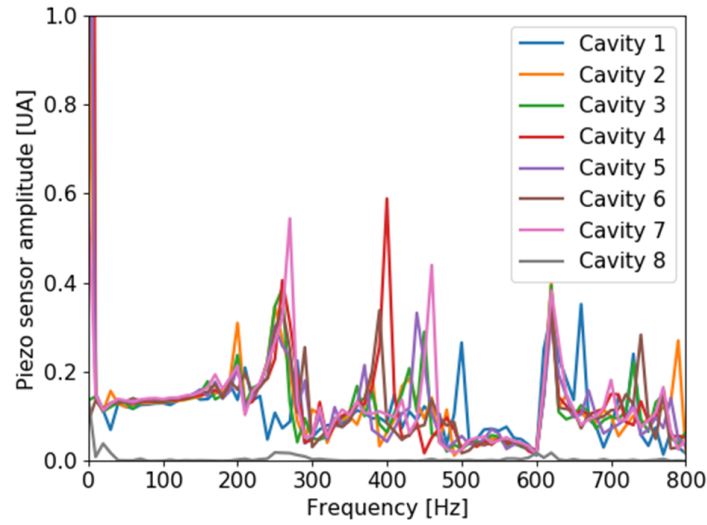
Figure (3.7) Cavity mechanical transfer function of an EuXFEL module. The cavities were excited using the piezoelectric tuner. A second piezoelectric pickup was used to measure the resulting mechanical excitation [73]
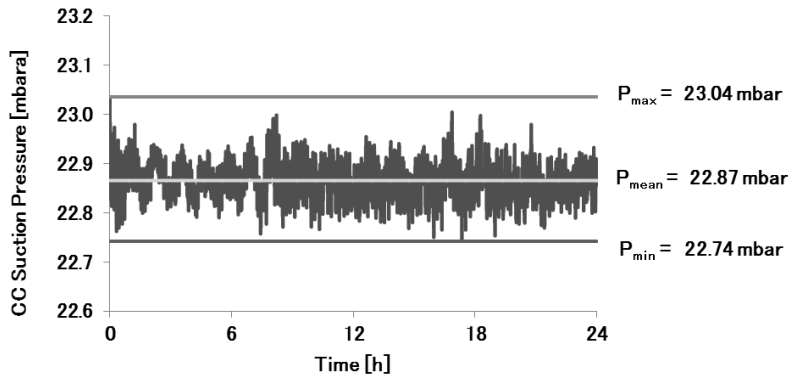

Figure (3.8) Cryogenic bath pressure stability of EuXFEL [74]

magnitude of $1\,\mathrm{Hz}$ RMS and covers the spectrum up to several hundreds of hertz. Fig 3.9 shows a microphonic spectrum measured on a TESLA cavity driven in CW.

Finally the radiation pressure caused by the accelerating field excerts a force on cavity walls thus deforming its geometry. These forces are proportional to the squared value of the cavity gradient and are characterized by the LFD coefficient.

For TESLA cavities the LFD coefficient is $k_{lfd} = -1\,\mathrm{Hz}/(\mathrm{MV/m})^2$. Even though in CW, the average effect of LFD can be easily compensated, pondero-
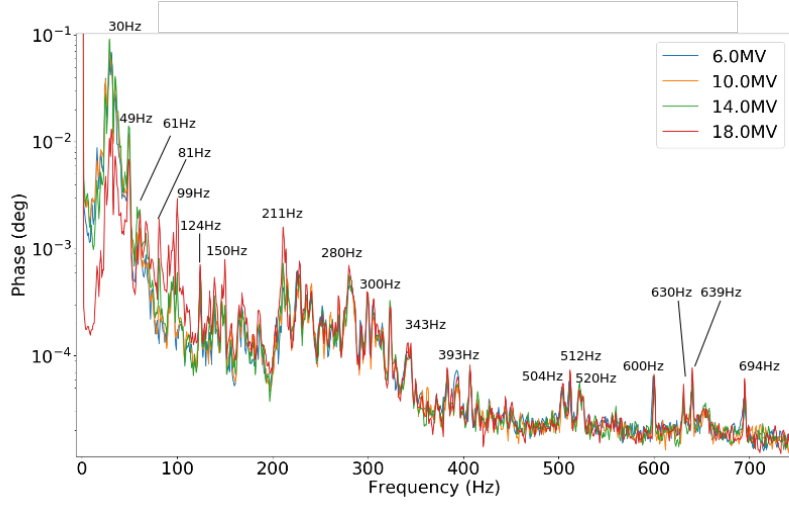
Figure (3.9) Detuning disturbance effects on cavity phase at Cryo Module Test Bench. The lines at 30 Hz and 49 Hz [72] are microphonic oscillations caused by vacuum pumps.

motive instabilities appear when the magnitude of LFD becomes larger than the cavity bandwidth. For a gradient of $16\,\mathrm{MV\,m^{-1}}$ the LFD magnitude is $\sim 250\,\mathrm{Hz}$. Therefore high-gradient cavities in the injector, L1 and L2 will be affected by ponderomotive instabilities. These instabilities are generated by a feedback between the mechanical excitation produced by radiation pressure and the cavity gradient variation due to changing detuning. Two kinds of ponderomotive instabilities are present in superconducting cavities: monotonic and oscillatory instabilities [76].

In monotonic instability, the radiation pressure bends the cavity resonance curve until a zone of instability is generated (Fig. 3.10). If the cavity is tuned over the monotonic instability threshold it experiences a discrete variation of the detuning. Such a variation is caused by mechanical relaxation and causes a drop of the accelerating gradient. Since this threshold is in the proximity of the cavity resonance, detuning drifts may trigger a gradient drop of a tuned cavity. Oscillatory instability happens over a range of negative values for cavity detuning. In this region, the cavity electromagnetic feedback makes the gradient and detuning start to oscillate at increasing amplitude. Nonlinear effects eventually stop the amplitude growth. The presence of oscillatory instability is determined by the cavity bandwidth and detuning and by the parameters of mechanical resonances. It is then of the highest importance to realize a resonance controller that
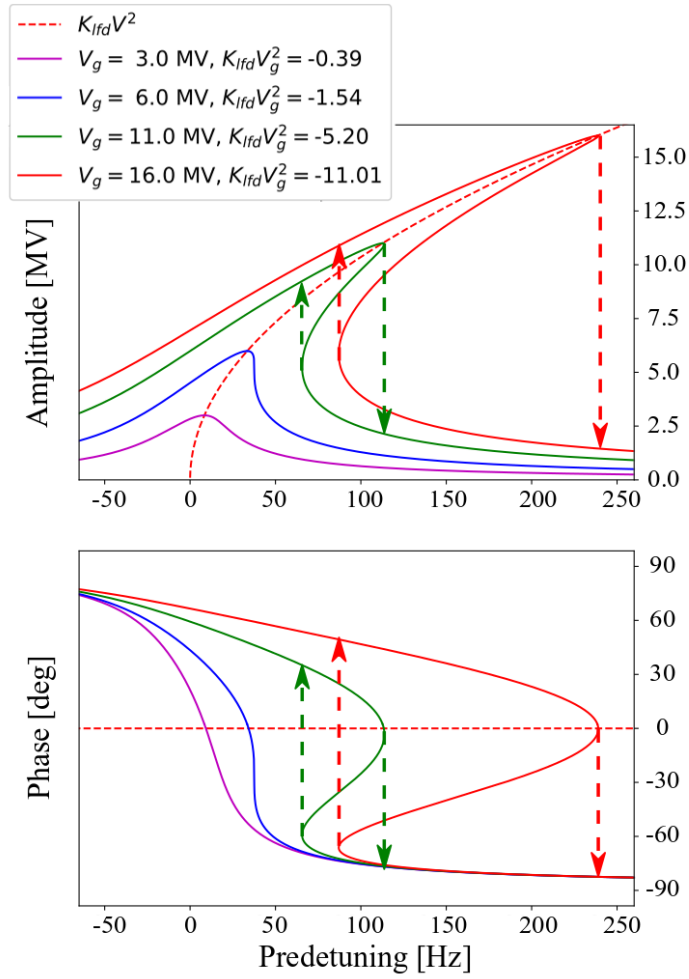
Figure (3.10) Static LFD effects on SRF TESLA cavities with $Q_L = 3 \times 10^7$ and the LFD constant $k_{\mathrm{lfd}} = -1\,\mathrm{Hz}/(\mathrm{MVm}^{-1})^2$. The intrinsic detuning is the detuning of the cavity without considering LFD-produced frequency shift. At higher gradients the cavity resonance curve is bent and is affected by monotonic instability. The instability jumps are indicated with arrows.

reduces the system detuning and prevents the occurrence of instabilities that may lower the accelerator availability or increase the gradient error outside the specifications. An additional challenge in controlling both monotonic and oscillatory instabilities arise from mechanical and RF cross-couplings between the cavities within a single module. The usual way to achieve resonance stability with high Q_L is to control the cavities individually with a mixed Generator Driven Resonance (GDR) and Self Excited Loop (SEL) driving mode [77, 78, 79]. In GDR the drive signal frequency is determined by the RF controller. This driving mode has the lowest amount of phase error and is currently used at EuXFEL. With SEL, the RF drive frequency is locked to the cavity resonance frequency, thus avoiding the occurrence of the ponderomotive instabilities. Therefore a mixed GDR-SEL controller uses GDR to accelerate the beam at low phase errors and reverts back to SEL when the cavity experiences ponderomotive instabilities or large phase errors. For EuXFEL, however, VS mandates multiple cavities to be driven by a single amplifier, thus making the application of SEL-based techniques impossible. Therefore solutions that rely only on the use of the fast piezoelectric tuner have to be used. The LP mode of operation has the challenges of both CW and SP mode of operation. As for the CW mode, cavities driven in the LP mode are affected by microphonics and ponderomotive instabilities, while having periodic detuning excursions of hundreds of hertz due to varying average LFD. Therefore, an improved controller that uses a modified version of CW and SP mode resonance controller techniques will be likely required.

Third harmonic module and CW gun The same consideration for the accelerating cavities has to be done to the third harmonic cavities and CW gun. For the third harmonic cavities it is required to reach a CW gradient of $E_{acc} = 15\,\mathrm{MV\,m^{-1}}$ [26, 80, 81]. The cavity parameters are: $L^{3.9} = 0.346\,\mathrm{m}$ $\frac{r}{Q}^{3.9} = 750\,\Omega$ and $k_{lfd}^{3.9}$ between -0.6 and $-1.2\,\mathrm{Hz/(MV/m)^2}$ [82, 83]. An important difference between the third harmonic and accelerating module design, as presently built in the EuXFEL, is the lack of fast piezoelectric tuners for the 3.9 GHz cavities. Therefore it has to determined if the module that will be installed in the CW injector will need fast tuners. For the LCLS-II accelerator, which at the time of writing is in construction and has similar parameters in respect to the final EuXFEL CW upgrade, it was decided to modify the existing blade tuner design for the third harmonic cavities adding piezoeletric elements [84,

85]. For the EuXFEL 3.9 GHz module, even though much less experimental data is present compared to accelerating modules, it is still possible to give an estimate of the impact of ponderomotive instabilities. To do this, a normalized LFD coefficient, that is independent of cavity bandwidth, can be defined.

$$K_{lfd} = \frac{k_{lfd}}{L^2 f_{(1/2)}}. \tag{3.17}$$

Using (3.17), a condition for the occurrence of the monotonic instability can be defined [76]

$$-K_{lfd} \cdot V_c^2 > 1.54. \tag{3.18}$$

When the above equation is true, the cavity is affected by monotonic instability.

Fig. 3.11 shows the value of $-K_{lfd}V_c^2$ for the third harmonic cavity at different values of k_{lfd} and for a Q_L range between 10^7-10^8. In the plot the required RF power to achieve $E_{acc} = 15\,\mathrm{MV\,m^{-1}}$ is also shown. For $Q_L > 2 \cdot 10^7$ the cavity is affected by monotonic instability, whereas for $Q_L < 2 \cdot 10^7$, the instability might not be present depending on the k_{lfd} value. These estimates give a hint on the necessity to install piezoelectric tuners on the third harmonic module. If the available cavity RF power budget is less than 500 W, fast tuners to control the monotonic instability are likely to be needed. However, contrary to the accelerating modules, single cavity control might be used for the third harmonic module. Therefore using SEL could be a possible way to mitigate the impact of ponderomotive instabilities for this module. These considerations have to be validated by experimental results. For this, CW tests on the spare third harmonic module will start at DESY in 2021. Since the mechanical and electrical specifications are not yet completely defined for the gun cavity, it is even more difficult to determine the impact of microphonics and ponderomotive instabilities.

Enhancement of the RF detection chain   The CW upgrade offers the possibility to improve the current RF detection chain. The DCM module has to be modified to correct CW signals [86]. Additionally, the CW mode of operation allows to achieve lower noise, sub-100 as precision, RF detection [87, 88, 89].
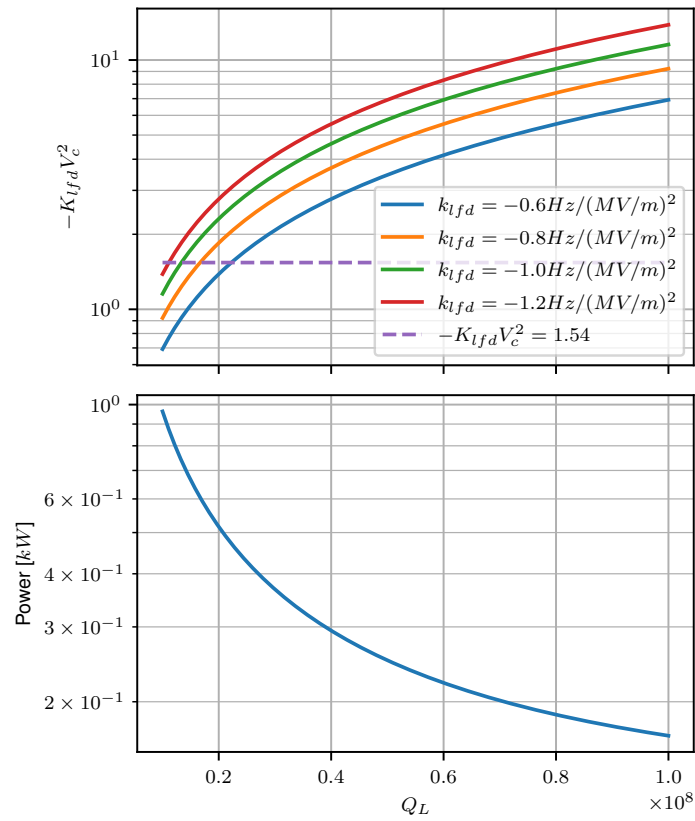
Figure (3.11)   Impact of the monotonic instability and required RF power for the third harmonic $3.9\,\mathrm{GHz}$ cavities in CW for $E_{acc} = 15\,\mathrm{MV\,m^{-1}}$. In the upper plot, $-K_{lfd}V_c^2$ in function of Q_L is shown. The threshold for the monotonic instability, $-K_{lfd}V_c^2 = 1.54$, is represented. In the lower plot, the required RF forward power is shown.

Chapter 4

Cavity parameters estimation

4.1 Online Detuning Computation and Quench Detection for Superconducting Resonators

Having continuous information on the physical state of superconducting RF cavities is crucial to operate SC accelerators reliably and efficiently. Since SRF resonators require cryogenic temperatures to maintain their superconducting properties, every effect that increases these devices power dissipation has to be promptly detected to avoid potential downtime of the accelerator. In particular, superconducting quenches can lower the Q_0 by several orders of magnitude, thus significantly increasing the heat load (Fig. 4.1). For the EuXFEL CW/LP upgrade, it is required to stop the RF drive after few hundreds of microseconds have passed since the quench happened [90]. For this reason, here, a new CW quench detection system is presented. This component is implemented in the LLRF system uTC FPGA logic to minimize estimation delay and is optimized for VS operation. The component can also perform an online estimation of cavity detuning for later use in a resonance controller.
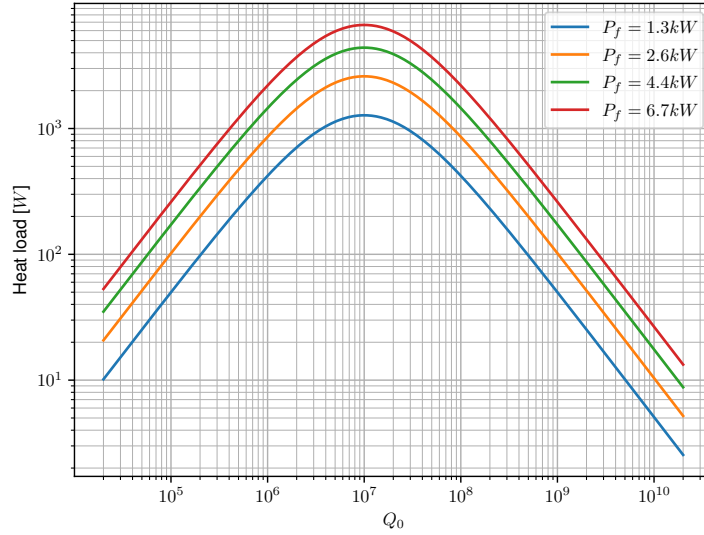
Figure (4.1)   Heat load at different Q_0 values to illustrate the effect of a quench on cavity heat dissipation. The Q_0 of a superconducting cavity is $> 10^{10}$ while, during a quench, it can go as low as 10^4. In this plot $Q_{ext} = 10^7$.

Online Detuning Computation and Quench Detection for Superconducting Resonators

Andrea Bellandi[ID], Łukasz Butkowski[ID], Burak Dursun[ID], *Member, IEEE*, Annika Eichler[ID], *Member, IEEE*, Çagıl Gümüş, Michael Kuntzsch[ID], Ayla Nawaz, Sven Pfeiffer[ID], Holger Schlarb, Christian Schmidt[ID], Klaus Zenker[ID], and Julien Branlard

Abstract—**Superconducting cavities are responsible for beam acceleration in superconducting linear accelerators. Challenging cavity control specifications are necessary to reduce radio frequency (RF) costs and to maximize the availability of the accelerator. Cavity detuning and bandwidth are two critical parameters to monitor when operating particle accelerators. Cavity detuning is strongly related to the power required to generate the desired accelerating gradient. Cavity bandwidth is related to the cavity RF losses. A sudden increase in bandwidth can indicate the presence of a quench or multipacting event. Therefore, calculating these parameters in real time in the low-level RF (LLRF) system is highly desirable. A real-time estimation of the bandwidth allows for a faster response of the machine protection system in the case of quench events, whereas the estimation of cavity detuning can be used to drive piezoelectric tuner-based resonance control algorithms. In this article, a new field programmable gate array (FPGA)-based estimation component is presented. Such a component is designed to be used either in continuous wave (CW) or pulsed operation mode with loaded quality factors between 10^6 and 10^8. Results of this component with free-electron LASer in Hamburg (FLASH), European X-ray free electron laser (EuXFEL), cryo module test bench (CMTB), and electron linac for beams with high brilliance and low emittance (ELBE) are presented.**

Index Terms—**Continuous wave (CW), digital signal processing (DSP), field programmable gate arrays (FPGAs), parameter estimation, particle accelerators, superconducting cavities.**

I. INTRODUCTION

SUPERCONDUCTING radio frequency (SRF) accelerating cavities are the principal component of superconducting linear accelerators. Thanks to their low surface resistance, it is possible to generate accelerating fields of several tens of megavolts per meter with duty cycles of the radio frequency (RF) pulses that range from about 1% up to continuous wave (CW) mode of operation [1]. Many challenges have to be faced when operating superconducting cavities. First, the cavities are operated at very high *external quality factors* (Q_{ext}) to reduce the RF power requirements. For TESLA-type

superconducting cavities, the typical range of values for Q_{ext} used in particle accelerators is between 10^6 and 10^8 [2], [3]. Since TESLA cavities have a resonance frequency of 1.3 GHz, this results in cavity bandwiths between 1.3 kHz and 13 Hz. For these bandwidths values, superconducting cavities are susceptible to nanometer-scale mechanical vibrations and Lorentz force detuning (LFD) disturbances. Since detuning disturbances increase the required power to operate a cavity, a resonance controller is required to keep the cavity tuned at the desired resonance frequency. Present and future superconducting machines using TESLA cavities can be grouped into two categories:

1) Pulsed machines with $Q_{\text{ext}} < 10^7$. This is the current mode of operation for the free-electron LASer in Hamburg (FLASH) [4] and the European X-ray free electron laser (EuXFEL) [5]. For these machines, the detuning disturbances mainly originate from the periodic LFD effects caused by the time-varying RF accelerating gradient. The magnitude of the disturbances is in the order of magnitude of hundreds of hertz.

2) CW and semi-CW pulsed machines with a duty cycle > 10% and $Q_{\text{ext}} > 10^7$. This is the case for the proposed EuXFEL CW upgrade [6], the electron linac for beams with high brilliance and low emittance (ELBE) [7], the linac coherent light source-II (LCLS-II) [8] and the Shanghai hard X-ray FEL facility (SHINE) [9]. In this case, external vibrations and mechanical drifts are the principal detuning disturbances. Additionally, for generator-driven resonator (GDR) systems LFD can cause ponderomotive instabilities [10]. These detuning disturbances are uncorrelated with respect to the RF system timing and have amplitudes of tens of hertz [11].

In pulsed accelerators, the detuning estimation can be accomplished with offline algorithms that run between the occurrences of two RF pulses. Resonance control is then performed with iterative learning control (ILC) algorithms by actuating piezoelectric tuners [12]. For CW machines, since the disturbances are uncorrelated to the RF pulse structure, the low-level RF (LLRF) control system must perform the detuning estimation and control in real time.

Typically, the estimation of cavity detuning is performed using the detuning angle formula [13]

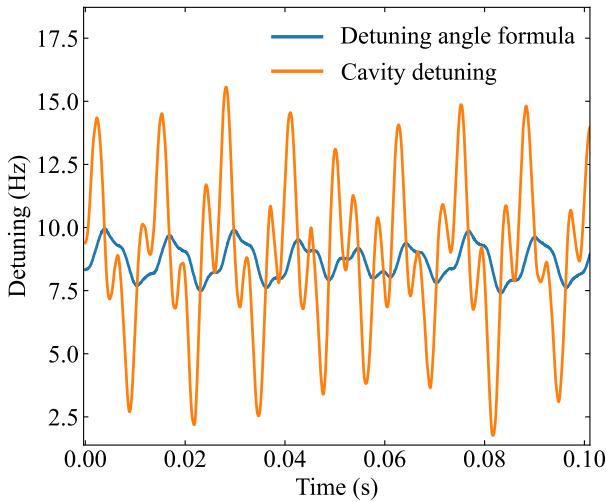$$\Delta \tilde{f} = f_{(1/2)} \tan(\Delta \theta) \qquad (1)$$

Fig. 1. Comparison between the cavity detuning and the detuning calculated with (1) for a superconducting cavity with $Q_L = 4.17 \cdot 10^7$ driven in CW. The cavity bandwidth is 31.1 Hz. The main detuning disturbance has a frequency of 79 Hz and presents an attenuation of 14 dB and a phase shift of 79° when calculated with the detuning angle.

with $\Delta \tilde{f}$ the cavity detuning estimation, $f_{(1/2)}$ the cavity half bandwidth, and $\Delta \theta$ the phase difference between the probe and forward cavity signal. However, when the spectrum of detuning disturbances lies at higher values than $f_{(1/2)}$, the detuning angle formula, which is valid only at steady state, ceases to be accurate due to the low-pass filter characteristic of RF cavities [14]. Such a condition is realized in pulsed mode due to the sharp signal transients or in CW at high *loaded quality factor* (Q_L) values (as in scenarios 1 and 2 described above). Fig. 1 shows the differences between the detuning calculated with a physical model of an SRF cavity and (1). Another challenge in the control of superconducting cavities is the detection of quench events. When a quench happens inside a cavity, the cavity loses its superconducting state, thus increasing the power dissipation. Since superconducting cavities must operate at cryogenic temperatures, a sudden increase in the dissipated power could result in a trip of the cryogenic system [15]. Therefore, a fast reaction of the interlock system is required to minimize the accelerator downtime. Electron multipacting inside the cavity has to be detected since it can increase heat dissipation in the cavity walls as well. A quench can be detected in pulsed machines by calculating the Q_L using the cavity gradient decay trace. Such an operation is performed by deriving the decay's time constant using an exponential cavity gradient fit. At EuXFEL and FLASH, the quench detection is done by software in the machine control system servers. Due to delays in data transmission and Q_L computations, the quench detection system can halt machine operation only after few more RF pulses are produced since a quench has happened. This corresponds to a quench detection delay of several hundreds of milliseconds. The threshold for the unloaded quality factor Q_0 to trigger the machine interlock for the actual quench detection system is $Q_0 < 5 \cdot 10^7$. For CW machines, the use of field decay is not possible. Furthermore, since the accelerating field is always present inside the cavities during operation, a delay

in detecting a quench has more severe consequences in terms of dissipated power. Therefore, an alternative way to detect quenches that is not dependent on a particular pulse structure is needed. A possible way to address the task of calculating both detuning and Q_L is to directly implement a model of the cavity dynamics in the field programmable gate array (FPGA) logic of the LLRF controller. This approach was already explored at DESY [16] and LBNL [17] and under study at HZB [18]. This article aims to present a new version of the component with the following improvements: " Fast quench detection system based on the cavity bandwidth magnitude threshold." Compact parallel parameter estimation of multiple cavities. This feature is required since the LLRF cavity control of FLASH and EuXFEL is based on vector sum (VS). This means that the algorithm has to manage up to 16 cavities at the same time. " Inclusion of beam current in the computations. " Use of cascaded integrator-comb (CIC) filters and finite impulse response (FIR) compensators to reduce the signal noise. The advantage of using such a filtering structure with respect to previous implementations is its flat passband characteristic and linear phase.

The initial target specifications for the presented component are to match the sensitivity of Q_0 variations of the current quench detection system used at EuXFEL and FLASH. Furthermore, the system must have a reaction time $\lesssim 200$ μs to avoid an excessive deposit of heat in the cryogenic system [19]. The error on detuning estimation has to be smaller than the cavity half bandwidth. Additional constraints are required to make the component work in the FPGA of the LLRF systems used in this study. The component clock speed must be at least 81.25 MHz and FPGA occupation should not exceed 20% for each kind of FPGA resource. To design the device, SpinalHDL [20] was used to describe the component logic. SpinalHDL is a Scala-based [21] embedded domain-specific hardware description language (HDL) that generates Verilog or VHDL sources. The main advantage of SpinalHDL is its capability of using Scala and Java libraries for simulation and procedural generation tasks. Additionally, SpinalHDL allows easy inter-operation with our existing VHDL code-base. In this article, Section II introduces the model used in the estimator and design considerations. Section III discusses the HDL implementation details. In Section IV, the component estimation capabilities are evaluated using data taken from the superconducting facilities FLASH and EuXFEL and tested at ELBE and cryo module test bench (CMTB) [22].

II. CAVITY MODEL

Since the component has to calculate both the cavity bandwidth and detuning independent of the RF pulse structure, its mathematical representation is derived directly from a general model of RF cavity dynamics. This model is described by a set of differential equations [14].

$$\dot{I}_p = 2\pi(-f_{(1/2)}I_p - \Delta f Q_p + B I_b + K I_f) \quad (2)$$

$$\dot{Q}_p = 2\pi(-f_{(1/2)}Q_p + \Delta f I_p + B Q_b + K Q_f) \quad (3)$$

$$K = \frac{f_0}{Q_{ext}}, \quad B = \frac{f_0}{2}\frac{r}{Q}, \quad f_{(1/2)} = \frac{f_0}{2Q_L} \quad (4)$$

with $(I/Q)_p$, $(I/Q)_f$, and $(I/Q)_b$ the in-phase and quadrature (I&Q) cavity signal components of the probe, forward, and beam current signals, f_0 the cavity resonance frequency, (r/Q) the geometrical shunt impedance, and Δf is the estimated detuning. For (2) and (3) to hold, the system is supposed to be calibrated. Therefore,

$$I_p = I_f + I_r, \quad Q_p = Q_f + Q_r \tag{5}$$

have to be valid. $(I/Q)_r$ are the I&Q reflected cavity signals. The loaded quality factor Q_L

$$Q_L = \frac{1}{\frac{1}{Q_0} + \frac{1}{Q_{ext}}} \tag{6}$$

depends on Q_0 and the external quality factor Q_{ext}. Superconducting cavities are normally driven in accelerators using a $Q_{ext} \ll Q_0$. Typically, in recent superconducting cavities, $Q_0 > 10^{10}$. Therefore, $Q_L \approx Q_{ext}$ when the cavity is in a superconducting state. When a quench happens, Q_0 can drop to values as low as 10^4. Then, when Q_0 reaches values of the same order of Q_{ext}, Q_L starts to decrease and a quench can be detected as an increase of $f_{(1/2)}$. To compute cavity bandwidth and detuning as function of time, (2) and (3) can be solved by $f_{(1/2)}$ and Δf,

$$f_{(1/2)} = \frac{I_p(KI_f - \dot{I}_p/2\pi + BI_b)}{I_p^2 + Q_p^2}$$
$$+ \frac{Q_p(KQ_f - \dot{Q}_p/2\pi + BQ_b)}{I_p^2 + Q_p^2} \tag{7}$$

$$\Delta f = \frac{Q_p(KI_f - \dot{I}_p/2\pi + BI_b)}{I_p^2 + Q_p^2}$$
$$- \frac{I_p(KQ_f - \dot{Q}_p/2\pi + BQ_b)}{I_p^2 + Q_p^2}. \tag{8}$$

Since the computation of (7) and (8) requires the derivative of the probe signal, the high-frequency part of the spectrum is amplified. As a consequence, the estimations of the parameters include an amount of noise several times higher than the cavity half bandwidth. For this reason, the RF signals have to be filtered out before being used in (7) and (8). Therefore, offline analysis is performed to optimize the filter cutoff value. Fig. 2 gives an estimation of the signal-to-noise ratio (SNR) of the cavity bandwidth using (7) at different cutoff frequencies. A Butterworth filter is used for the analysis due to its maximally flat response. Since the component is meant to be used in CW and pulsed mode, pulsed data were used to perform the analysis of Fig. 2 due to sharp signal transitions in this mode of operation. These transitions can compromise the bandwidth and detuning estimation if the filtering process leads to excessive overshoot or slow tracking of the signal. In applications where cavities are operated in CW mode only, using CW data to perform a similar analysis might improve the SNR of the estimated parameters.

For cutoff frequencies between 30 and 100 kHz, the SNR is maximum with a value of almost 20 dB. For the component, a cutoff frequency of 36.1 kHz was chosen. Such a value was chosen because it simplifies the development of a potential resonance controller that uses the detuning estimation. For a
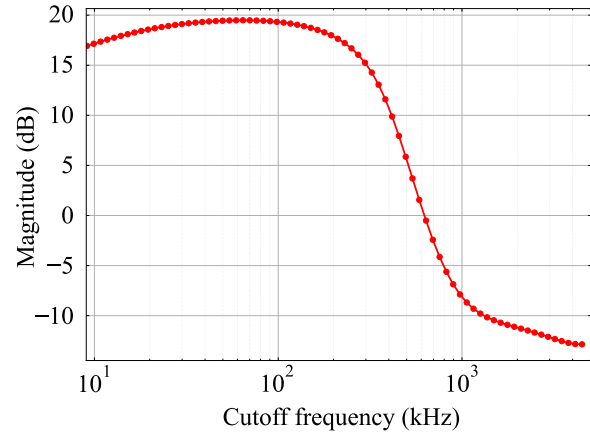

Fig. 2. Estimated bandwidth SNR as a function of the cutoff frequency of a second-order Butterworth filter. The optimal cutoff value is between 30 and 100 kHz with an SNR of almost 20 dB.

cutoff of 36.1 kHz, the SNR is within 2 dB below the absolute maximum of Fig. 2. The amount of filtering corresponds to a bandwidth reduction of 125 with respect to the original signal bandwidth of 4.512 MHz.

III. IMPLEMENTATION DETAILS

To perform an online calculation of $f_{(1/2)}$ and Δf, (7) and (8) have to be implemented in the FPGA-configurable logic. Furthermore, before performing the bandwidth and detuning estimation, the cavity signals have to be pre-filtered, and the probe derivative has to be calculated. All the calculations are performed with 18 bits wide signals to take advantage Xilinx FPGAs digital signal processing (DSP) resource characteristics [23].

A. Filtering Block

Two different types of low-pass filters are cascaded to realize the desired bandwidth reduction. This choice allows us to realize a flat passband and linear phase, and, at the same time, minimize the FPGA resource usage. First, the signals are decimated and filtered by a CIC structure [24] by a factor of 25. Such a method allows realizing a filter that works at the original sample rate of 9.025 MHz and does not require hardware multipliers. The normalized transfer function in dB of the CIC filter is

$$H_{CIC} = 10 \log_{10}\left[\frac{\sin(\pi M f_{CIC})}{\pi M f_{CIC}}\right]^{2N} \tag{9}$$

with N the CIC filter order, M the differential delay, and f_{CIC} the frequency normalized to the CIC output sample rate of 361 kHz. $N = 2$ is chosen to match the filter order of the Butterworth filter used in the previous section. Moreover, $M = 2$ is chosen to further increase the stopband attenuation of the filter. The CIC has a latency of six clock cycles. For the second filtering stage, an FIR-based low-pass filter is used to reduce the signal bandwidth by a factor 5. Finally, the signals are down-sampled to 72.2 kHz. Using an FIR filter allows compensating for the CIC passband droop and realizing the probe signal's derivative operation. A multiplying-ACcumulate (MAC) structure is chosen to implement the FIR
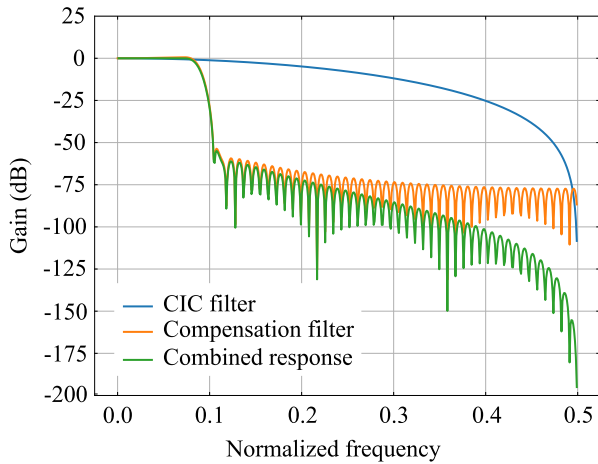
Fig. 3. Transfer function of the CIC filter, the FIR compensator, and their combined response.

filter [25] to reduce the DSP resources utilization. Such a structure requires only one hardware multiplier and two look-up tables (LUTs) to store the FIR coefficients and the signal values, and it is optimized to operate at low sample rates. The generation of the FIR coefficients is realized with a bandwidth-limited inverse CIC transfer function, as described in [26]. Additionally, for the channel that provides the probe derivative, the FIR transfer function is multiplied by $j\omega$. In Fig. 3, the final combined transfer function of the CIC and FIR filter is shown. Since in particle accelerators with VS control, multiple cavities are managed by a single LLRF control system, the resource usage can further be optimized when multiple cavity channels are needed in the same FPGA. Because of this and to avoid unnecessary structural replication, the control logic of both CIC and FIR filters and the FIR coefficient tables of the filtering block is shared between the cavity signals of all channels. The FIR and the final signal down-sampling computations require four and one clock cycles to complete.

Further improvements in FPGA DSP resource usage of the MAC unit could be possible by serializing the signals after the CIC decimator. Then a single MAC that works on a stream of serialized values can be implemented to reduce the FPGA occupation. However, such a modification is possible at the cost of a more complex MAC control and pipeline units. Therefore, since the final component usage was compatible with the amount of available resources in our LLRF systems, it was decided not to implement further optimizations of the MAC.

B. Estimation Block

The symmetry in the equations of (7) and (8) can be used to generate a compact FPGA component that computes the cavity bandwidth and detuning with a pipelined architecture. Defining the quantities

$$T_{\mathrm{I}} = K I_{\mathrm{f}} - \dot{I}_{\mathrm{p}}/2\pi + B I_{\mathrm{b}} \tag{10}$$

$$T_{\mathrm{Q}} = K Q_{\mathrm{f}} - \dot{Q}_{\mathrm{p}}/2\pi + B Q_{\mathrm{b}} \tag{11}$$

$$A^2 = I_{\mathrm{p}}^2 + Q_{\mathrm{p}}^2 \tag{12}$$

TABLE I
SYNTHESIS RESULTS ON XC7K420T

Cavity channels	1	2	8	16	Total available resources
Lookup tables (%)	0.8	1.6	6.5	12.2	260600
Distribuited RAMs (%)	0.3	0.6	2.4	3.6	108600
Flip flops (%)	0.6	1.3	4.9	9.7	521200
Block RAMs (%)	0.1	0.1	0.1	1.6	835
DSP slices (%)	1.2	1.7	4.5	8.3	1680
Clock cycle delay	40	43	49	57	-

(7) and (8) can be redefined as

$$f_{(1/2)} = \frac{I_{\mathrm{p}} T_{\mathrm{I}} + Q_{\mathrm{p}} T_{\mathrm{Q}}}{A^2} \tag{13}$$

$$\Delta f = \frac{Q_{\mathrm{p}} T_{\mathrm{I}} - I_{\mathrm{p}} T_{\mathrm{Q}}}{A^2} \tag{14}$$

thus reducing the needed hardware multiplications from 16 to 10. To save even more FPGA resources when there is a need to manage multiple cavities, the cavity signals are serialized in a single stream. The stream of cavity signals is then used to evaluate the numerators and denominators of (13) and (14) by a single estimator block. This optimization is simple to implement due to the state-less nature of the estimator block pipeline. Finally, Δf and $f_{(1/2)}$ are computed by deserializing the stream of partial results and performing the final division operation in (13) and (14). The division is performed using an iterative divider component that takes 18 clock cycles to complete the operation. The estimator block latency delay is 29 clock cycles. Also, when using more than one cavity channel, an additional computation delay of one clock cycle plus a number of cycles equal to the number of cavity channels is required for the execution of serialization/de-serialization operations. The full block diagram of the estimation component is shown in Fig. 4.

The component was synthesized with different numbers of cavity channels to estimate the FPGA resource utilization. For this test, the default synthesis strategy of Vivado [27] is used. The target FPGA is the XC7K420T, which equips the DAMC-TCK7 board [28]. Such a board is currently in use in the LLRF system of FLASH and EuXFEL. The FPGA occupation results in different configurations are listed in Table I.

Even when 16 cavity channels are used, the occupancy is less than 13% for every type of resource. The estimated maximum clock frequency for the component in every configuration is 290 MHz. The analyses are performed using an out-of-context implementation approach. These results show that it is possible to implement the component in our LLRF systems even when the expected maximum number of channels is used. The final component's group latency is 170 μs.

IV. COMPONENT VERIFICATION

In this section, the estimator correctness is tested with simulated data and data taken from European XFEL and FLASH. The scope is to verify the agreement of the component estimations with those calculated using an offline model implemented with floating-point math. Results of online tests
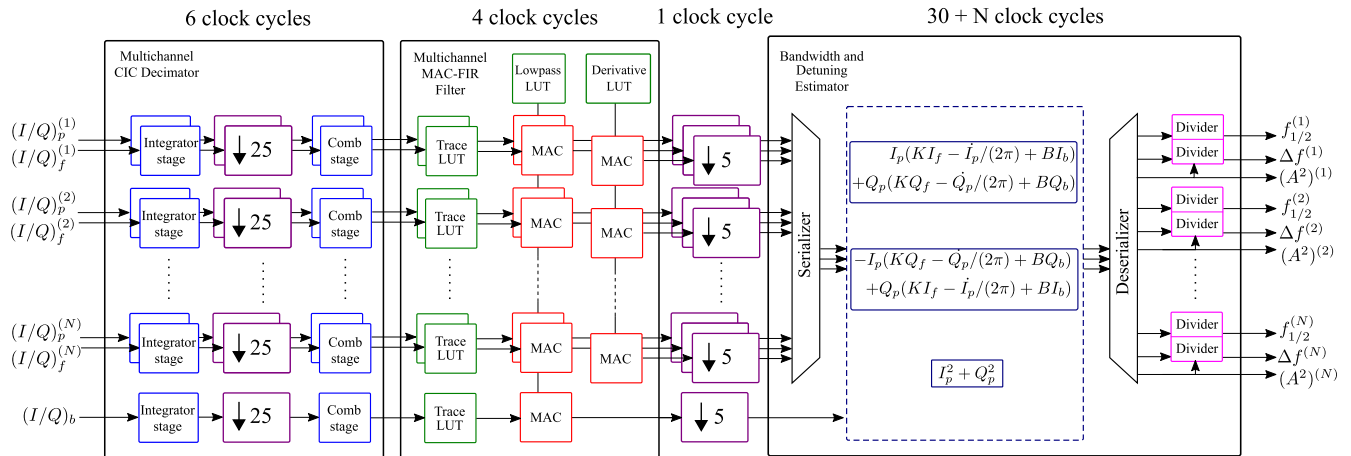
Fig. 4. Block diagram of the estimator component.

at CMTB and ELBE are also discussed, and the final errors on the estimated parameters are given.

A. Offline Verification

The functional verification of the estimation component is done using SpinalSim, the SpinalHDL simulation interface. Such an interface uses Verilator [29], a high-performance simulator, and HDL-to-C transpiler backend. SpinalSim allows defining the testbenches as elements of a test suite, thus simplifying the functional verification of the estimator's sub-components. The correctness of the component in estimating the bandwidth and detuning is checked by feeding cavity signal data to the HDL simulator and comparing the results with those calculated offline with (7) and (8). For the pulsed operation mode, data taken from the LLRF system of FLASH and XFEL is used. As shown in Fig. 5, an agreement exists between the traces calculated with the two methods. The root mean square error (RMSE) between the traces is 9.05 Hz. Due to the filter characteristics and the increased noise level at low probe amplitudes, only the last 70% of the trace is used in the analysis.

A discrepancy in the first part of the filling is caused by the signal noise at low probe amplitudes. The component behavior during quenches is also verified by observing the bandwidth growth from the nominal value (Fig. 6). In Fig. 6(a), an increment of cavity bandwidth happens for the orange trace at the end of the flattop, suggesting the presence of a quench event as opposed to the blue trace. The quench effect on the corresponding cavity amplitude can be observed in Fig. 6(b), with the affected trace showing a gradient loss at the end of the flattop when compared to the unaffected one.

For the CW mode of operation, there was not readily available offline data to use. Therefore, the RF data of an SRF cavity is generated doing a numerical integration of (2) and (3). Δf and $f_{1/2}$ are chosen to mimic common detuning and bandwidth disturbances, such as microphonics and quenches (see Fig. 7). For the microphonic disturbance, two sinusoidal disturbances, with a frequency of 30 and 49 Hz and an amplitude of 1.5 and 3.5 Hz, were chosen. The average
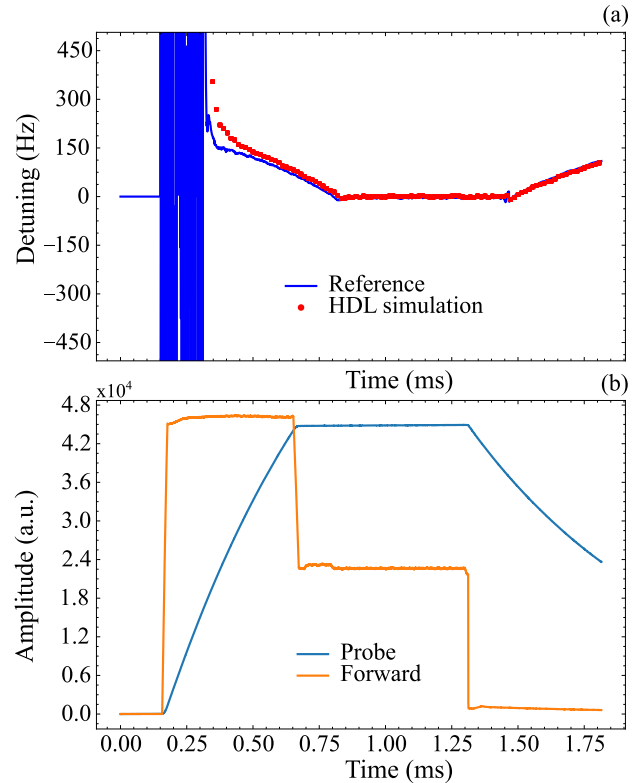

Fig. 5. Comparison between the detuning trace estimated from a previously recorded cavity pulse at FLASH and the reference one generated by the diagnostic server (a). $Q_L = 3.00 \cdot 10^6$ and the RF bandwidth is 230.08 Hz. The amplitudes of the signals for the forward and probe signals are shown in (b).

detuning is 5 Hz. These microphonic disturbance parameters are compatible with the noise characteristic observed at our CW test facility. Additionally, after 60 ms, a decay of Q_0 is triggered to simulate a quench. This variation in Q_0 lowers the loaded quality factor from $Q_L = 6 \cdot 10^7$ to $Q_L = 3 \cdot 10^7$. The component can estimate cavity parameters with an RMSE of 1.55 Hz for the bandwidth and 0.79 Hz for the detuning with respect to an initial cavity bandwidth of 21.67 Hz. This
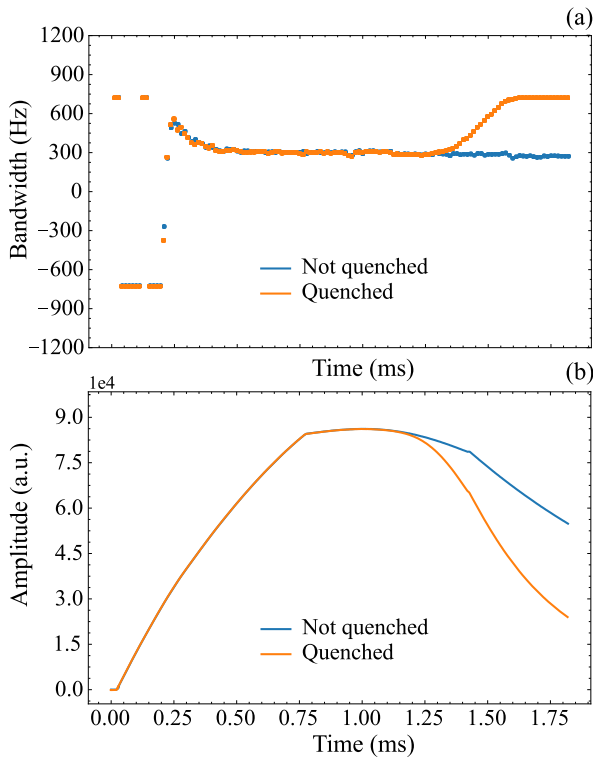
Fig. 6. Comparison of bandwidth traces (a) estimated from previously recorded cavity pulses of EuXFEL. The corresponding accelerating field is shown in (b).

test suggests that the estimator component can discriminate between quench and microphonic effects.

B. Experimental Verification for Pulsed Mode of Operation

Pulsed tests were performed at CMTB using an MTCA.4-based LLRF single-cavity system equipped with an SIS-8300L2 controller board [30]. During the tests, it was discovered that the isolation of the waveguide coupler that provides the forward and reflected cavity signals was less than 20 dB. This resulted in a drift of the bandwidth and detuning estimations by more than 10%. Therefore, to improve the component's estimation capabilities, the calibration method described in [31] was used. With such a method, the cross-coupling terms for the forward and reflected signals are calculated and can be used to correct the effects of the waveguide coupler's finite isolation. Therefore, the firmware was changed to use a corrected version of the forward channel

$$\begin{bmatrix} I_f \\ Q_f \end{bmatrix} = \begin{bmatrix} \Re(a) & -\Im(a) \\ \Im(a) & \Re(a) \end{bmatrix} \begin{bmatrix} I_f^m \\ Q_f^m \end{bmatrix} + \begin{bmatrix} \Re(b) & -\Im(b) \\ \Im(b) & \Re(b) \end{bmatrix} \begin{bmatrix} I_r^m \\ Q_r^m \end{bmatrix}$$
(15)

with $(I^m/Q^m)_f$ and $(I^m/Q^m)_r$ the uncorrected forward and reflected I&Q values as measured by the ADCs and a and b the calibration coefficients as defined in [31]. Decoupling forward and reflected cavity signals adds two additional clock cycles to the component delay.

To test the estimator, different gradients between 6.0 and 15.0 MV m^{-1}, were used to verify the component capability to estimate detuning at different amounts of LFD. The RF
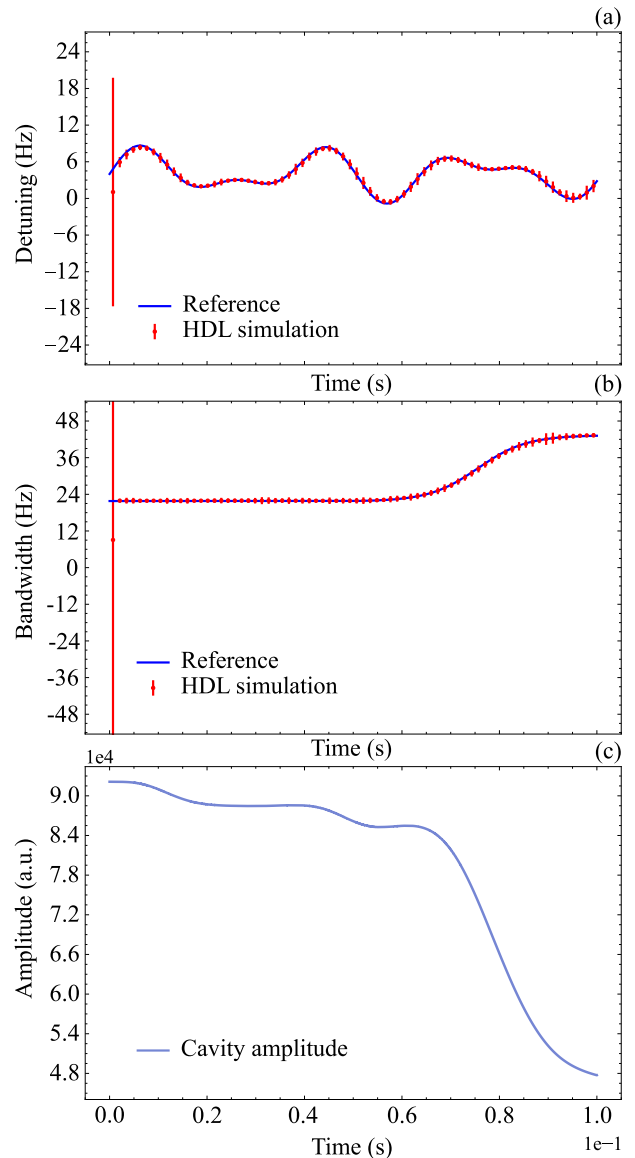

Fig. 7. Estimation of the detuning (a) and bandwidth (b) on simulated CW data of a cavity affected by microphonics. The computed detuning (a) and bandwidth (b) are compared to the reference values (blue traces). The cavity probe amplitude is shown in (c).

pulselength was 1 ms. An offline model is used to compare the component results. As in the previous sections, only the last 70% of the pulse was used to calculate these errors. During the tests, the flattop region length was set to zero with the decay phase immediately following the filling phase. The cavity bandwidth was set to 53 Hz ($Q_L = 2.45 \cdot 10^7$). Results of these tests (see Fig. 8) show that the FPGA estimator can compute the detuning value with an RMSE $\lesssim$ 15 Hz with respect to the offline model in all measurements. Even though systematic errors are present, probably caused by RF chain effects not included in our model, the RMSE value still allows the use of our component in resonance control.

Additional measurements were performed for different Q_L values at a fixed gradient of 12 MV/m^{-1}. Table II lists the mean error (ME), and the RMSE for the FPGA computed detuning, and the ME and peak-to-peak error (PP) for the
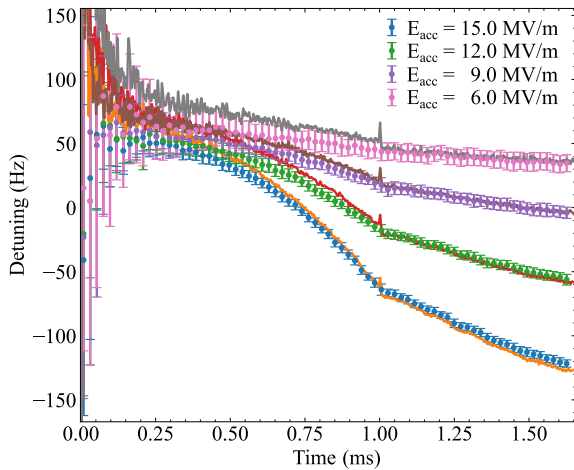
Fig. 8. Estimated detuning of a cavity driven in pulsed mode for $Q_L = 2.45 \cdot 10^7$. The dependence of the detuning with respect to the cavity gradient reveals the presence of LFD. Solid lines represent the computed offline estimation using the same equations, while the error bars represent the detuning mean and standard deviation calculated on the FPGA.

TABLE II
ESTIMATION ERRORS FOR PULSED MODE OF OPERATION

Q_L ($\cdot 10^7$)	0.62	1.23	2.47	4.88
Bandwidth (Hz)	209.7	105.7	52.6	26.6
Bandwidth ME (Hz)	-10.36	-1.50	-1.89	0.00
Bandwidth PP (Hz)	42.33	45.08	43.64	58.00
Q_0^q ($\cdot 10^7$)	6.14	5.77	5.96	4.48
Detuning ME (Hz)	-5.54	0.16	-1.85	1.54
Detuning RMSE (Hz)	7.38	4.50	6.82	5.91

computed bandwidth at over one pulse. In all cases, the ME is less than 6% of the respective cavity bandwidths. The half value of the bandwidth PP indicates how far away a threshold has to be set to detect a quench occurrence. Using (4), it is possible to calculate the Q_0 value that corresponds to a variation of the bandwidth equal to the half PP value

$$Q_0^q = \frac{f_0}{\delta f_{PP/2}} \qquad (16)$$

with $\delta f_{PP/2}$ the half of the bandwidth PP, and Q_0^q the Q_0 value resulting from a bandwidth variation of $\delta f_{PP/2}$. In (16), it is assumed that the initial Q_0 is much higher than Q_0^q. In Table II, the Q_0^q values are similar to the sensitivity of the actual quench detection system of EuXFEL and FLASH. In particle accelerators with millisecond-long pulses and $Q_L \gtrsim 2 \cdot 10^7$, a decay-based quench detector may have better sensitivity. However, accelerators with RF pulses long enough ($\gtrsim$10 ms) for the quench to fully develop, the presented technique can still be used to catch a quench before the field decay can be measured. Since the cavity used for the tests is affected by multipacting, it is possible to evaluate how the estimated bandwidth signal changes at different gradients. In such a test, as shown in Fig. 9, the estimated cavity bandwidth increases as a consequence of a drop in Q_0. The traces that show an increment in cavity bandwidth present faster-decaying probe
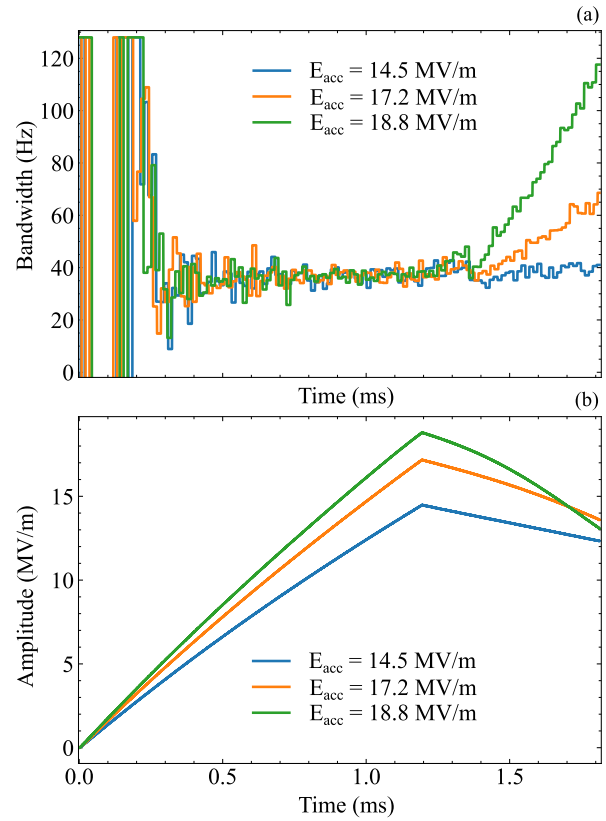

Fig. 9. Estimated cavity bandwidth in pulsed mode of a cavity experiencing multipacting at different maximum gradients (a). $Q_L = 3.42 \cdot 10^7$. The corresponding cavity amplitude is shown in (b).

TABLE III
ESTIMATION ERRORS FOR THE CW MODE OF OPERATION

Q_L ($\cdot 10^7$)	0.50	1.00	2.02	4.17
Bandwidth (Hz)	260.0	130.0	64.4	31.2
Bandwidth ME (Hz)	-0.61	1.51	-1.43	0.91
Bandwidth PP (Hz)	30.05	27.45	21.78	36.60
Q_0^q ($\cdot 10^7$)	8.65	9.47	11.93	7.10
Detuning ME (Hz)	0.01	-0.02	0.02	0.00
Detuning RMSE (Hz)	3.08	2.65	2.26	3.43
Filtered detuning RMSE (Hz)	0.87	0.77	0.69	0.98

signals when compared to the trace unaffected by multipacting at $E_{acc} = 14.5$ MV/m^{-1}. Additionally, a heat load increase of several watts was observed once the bandwidth signal starts to increase, thus showing the component capability in detecting anomalous power losses in real time.

C. Experimental Verification for CW Mode of Operation

For the CW tests, the system is first calibrated in the pulsed mode as in the previous paragraph and then switched to CW mode of operation to perform the measurements at different Q_L values. In Table III, the reported errors for bandwidth and detuning are lower than the values measured in the pulsed mode. A possible explanation for such a result is that, compared to the pulsed mode, the CW mode of operation lacks RF signal discontinuities and presents smaller transients. Therefore, the estimator in the CW mode of operation is less subjected to the filtering process's effects.
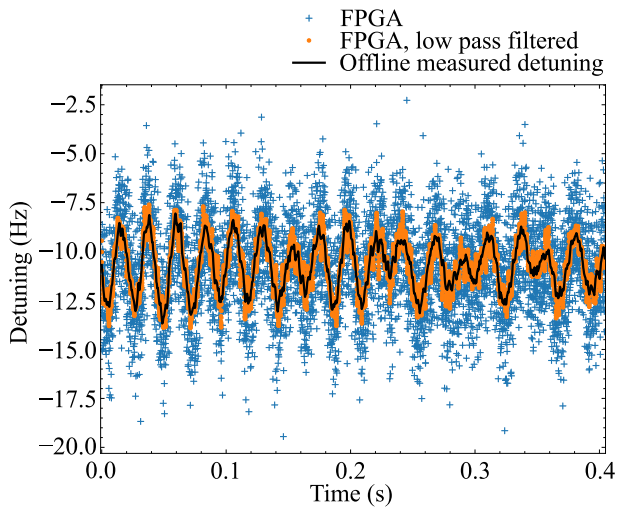
Fig. 10. Comparison between the detuning estimated by the FPGA and the offline model of a cavity driven in CW. The cavity is affected by a microphonic signal with a PP amplitude of 5 Hz. The low-pass-filtered FPGA detuning trace with a cutoff of 1.0 kHz is also shown.
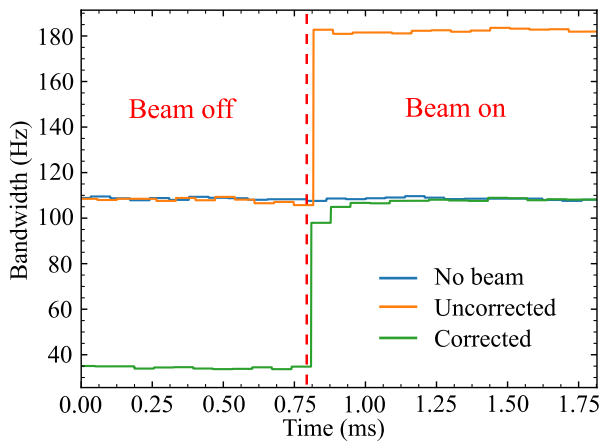

Fig. 11. Effects of the beam loading on the FPGA estimated bandwidth at ELBE. The beam current is 450 μA.

Detuning disturbances in CW have a spectrum that does not exceed 1 kHz [32], [33]. Furthermore, in our machines, the piezoelectric tuner bandwidth is $\simeq 1$ kHz. Therefore, it is of interest to calculate the RMSE error once the detuning estimations are filtered by such an amount. Fig. 10 and Table III show a reduction in the detuning RMSE to less than 1 Hz after a Butterworth filter with a cutoff of 1 kHz is applied.

Finally, the estimator's ability to compensate for the beam loading-induced effects is tested at the ELBE accelerator. A beam-based calibration is used to set up the estimator in the presence of the beam. While maintaining the CW mode of operation, a 4.5 ms long bunch train is generated. Using (7) and (8), it is possible to find the beam current value that minimizes the discrepancy between the mean bandwidth and detuning values computed with and without the presence of beam loading. For the successive measurements, the current value set in the estimator component is varied proportionally to the current drawn from the thermionic gun of ELBE. The

TABLE IV
BANDWIDTH ERRORS IN THE PRESENCE OF BEAM LOADING

Gun current (µA)	600	450	300	150
Bandwidth ME (Hz)	-0.88	0.62	-0.39	-0.19

effects of the correction on the bandwidth estimation are shown in Fig. 11. The uncorrected bandwidth trace jumps when the beam is switched on, resulting in an incorrect bandwidth estimation. Therefore, the beam loading term in (7) has to be set to get a correct bandwidth estimation. Since there was no way to directly feed a beam-synchronized current value in the estimator in the setup used during the tests, a constant correction is used. Therefore, the corrected trace in this plot is valid only in the presence of the beam. Table IV reports the bandwidth ME at different gun current values compared to a measure without beam loading. Such ME results to be less than 1 Hz for all measurements.

V. CONCLUSION

In this article, an FPGA-based detuning and bandwidth estimator for superconducting cavities is presented. Such a component is optimized to manage multiple cavities simultaneously, thus enabling its usage in accelerators that use VS control. Moreover, compared to preexisting solutions, using a cascaded CIC-FIR pre-filtering stage allows us to realize a compact component with flat passband characteristics. The synthesis results show that the FPGA resources needed to implement the component are low enough to allow its use in DAMC-TCK7- and SIS8300-L2-based LLRF systems. These LLRF controllers are currently in use at DESY and HZDR. The ability to estimate the cavity parameters online is demonstrated in simulations and experiments. These tests were conducted in pulsed and CW mode of operation at Q_L values between $5 \cdot 10^6$ and $5 \cdot 10^7$ in the presence of LFD, microphonics, and, in the case of ELBE, with a beam current of several hundreds of µA. Due to the limitations of the current setup at ELBE, it was not possible to feed the component with beam loading values measured directly from beam diagnostics. Instead, a fixed beam loading correction was set in the component for each test. Future experiments will be needed to understand if streaming beam loading values in the component from a beam measurement device are viable during accelerator operation. These results show that the component is able to detect quenches and multipacting with a delay of 170 µs. Additionally, given the measured bandwidth PP error, the component can be used in detecting quenches in CW and pulsed machines. The component delay value is three orders of magnitude smaller than the delay of the software-based quench detection system currently in use at EuXFEL, thus enabling a much faster reaction to quench events. The potential RMSE of the estimated detuning in CW was measured to be less than 1 Hz with no significant offset with respect to the values estimated with an offline cavity model. Therefore, it is planned to use the HDL component's detuning estimations as input for future CW resonance controllers to compensate for detuning disturbances.

ACKNOWLEDGMENT

REFERENCES

[1] H. Padamsee *et al.*, *RF Superconductivity for Accelerators*, vol. 2011. Hoboken, NJ, USA: Wiley, 2008.

[2] M. Altarelli *et al.*, "The European X-ray free-electron laser. Technical design report," *Desy*, vol. 97, p. 4, Jul. 2006.

[3] T. Raubenheimer, "The LCLS-II-HE, A high energy upgrade of the LCLS-II," in *Proc. 60th ICFA Adv. Beam Dyn. Workshop Future Light Sources*. Shanghai, China: JACOW, Mar. 2018, pp. 6–11.

[4] V. Ayvazyan *et al.*, "LLRF control system upgrade at FLASH," in *Proc., 8th Int. Workshop Pers. Comput. Part. Accel. Controls (PCaPAC)*. Saskatoon, Saskatchewan: JACOW, 2010, pp. 150–152.

[5] J. Branlard *et al.*, "The European XFEL LLRF system," in *Proc. 3th Int. Part. Accel. Conf. (IPAC)*, vol. 12. New Orleans, LA, USA: JACOW, May 2012, pp. 55–57.

[6] J. Sekutowicz *et al.*, "Feasibility of CW and LP operation of the XFEL linac," in *Proc. 35th Free–Electron Laser Conf. (FEL)*. New York, NY, USA: JACOW, Aug. 2013, pp. 189–192.

[7] P. Michel *et al.*, "The rossendorf IR-FEL ELBE," in *Proc. 28th Free-Electron Laser Conf. (FEL)*. Berlin, Germany: JACOW, 2006, p. 488.

[8] L. Doolittle *et al.*, "LLRF Control of high QL Cavities for the LCLS-II," in *Proc. 7th Int. Part. Accel. Conf. (IPAC)*. Busan, South Korea: JACOW, Jun. 2016.

[9] C. Feng and H.-X. Deng, "Review of fully coherent free-electron lasers," *Nucl. Sci. Techn.*, vol. 29, no. 11, p. 160, Nov. 2018.

[10] D. Schulze, "Ponderomotive stability of RF resonators and resonator control systems," Ph.D. dissertation, Institut für Experimentelle Kernphysik, Univ. Karlsruhe, Karlsruhe, Germany, Dec. 1972.

[11] A. Bellandi, J. Branlard, A. Eichler, and S. Pfeiffer, "Integral resonance control in continuous wave superconducting particle accelerators," presented at the IFAC World Congr., Berlin, Germany, 2020.

[12] M. Grecki *et al.*, "Piezo control for XFEL," 2018, *arXiv:1803.09042*. [Online]. Available: http://arxiv.org/abs/1803.09042

[13] T. P. Wangler, *RF Linear Accelerators*. Hoboken, NJ, USA: Wiley, 2008.

[14] T. Schilcher, "Vector sum control of pulsed accelerating fields in lorentz force detuned superconducting cavities," Ph.D. dissertation, Dept. Fachbereich Physik, Univ. Hamburg, Hamburg, Germany, Mar. 1998. [Online]. Available: https://cds.cern.ch/record/380230

[15] J. Branlard, V. Ayvazyan, O. Hensler, C. Schmidt, H. Schlarb, and W. Cichalewski, "Superconducting cavity quench detection and prevention for the European XFEL," in *Proc. 16th Int. Conf. RF Supercond. (SRF)*. Paris, France: JACOW, Sep. 2013, pp. 1–3.

[16] R. Rybaniec *et al.*, "Real-time estimation of superconducting cavities parameters," in *Proc. 5th Int. Part. Accel. Conf. (IPAC)*. Dresden, Germany: JACOW, Jun. 2014, pp. 2456–2458.

[17] (2019). *Bedrock Project*. Accessed: Oct. 16, 2020. [Online]. Available: https://github.com/BerkeleyLab/Bedrock

[18] P. Echevarria, B. G. Arruabarrena, A. Ushakov, J. Jugo, and A. Neumann, "Simulation of quench detection algorithms for Helmholtz Zentrum Berlin SRF cavities," *J. Phys., Conf. Ser.*, vol. 1350, no. 1, Nov. 2019, Art. no. 012187.

[19] J. Sekutowicz, private communication, Jan. 2021.

[20] C. Papon. (2020). *Spinal HDL Documentation*. Accessed: Mar. 26, 2020. [Online]. Available: https://spinalhdl.github.io/SpinalDoc-RTD/

[21] M. Odersky *et al.*, "An overview of the Scala programming language," Ecole Polytechnique Fédérale de Lausanne (EPFL), Lausanne, Switzerland, Tech. Rep. LAMP-REPORT-2006-001, 2004.

[22] J. Branlard *et al.*, "Highlights of the XM-3 cryomodule tests at DESY," in *Proc., 29th Linear Accel. Conf. (LINAC)*. Beijing, China: JACOW, Sep. 2018, pp. 388–390.

[23] Xilinx. (Mar. 2018). *7 Series DSP48E1 Slice*. Accessed: Feb. 16, 2021. [Online]. Available: https://www.xilinx.com/support/documentation/user_guides/ug479_7Series_DSP48E1.pdf

[24] E. Hogenauer, "A class of digital filters for decimation and interpolation," in *Proc. IEEE Int. Conf. Acoust., Speech, Signal Process.*, vol. 5, Apr. 1980, pp. 271–274.

[25] U. Meyer-Baese and U. Meyer-Baese, *Digital Signal Processing With Field Programmable Gate Arrays*, vol. 65. New York, NY, USA: Springer, 2007.

[26] J. Arzi. (Dec. 2015). *Small Tutorial on CIC Filters*. Accessed: Feb. 9, 2021. [Online]. Available: http://www.tsdconseil.fr/log/scrip/tscilab/cic/cic-en.pdf

[27] T. Feist. (Apr. 2012). *Vivado Design Suite*. Accessed: Feb. 9, 2021. [Online]. Available: https://www.xilinx.com/products/design-tools/vivado.html

[28] D. Makowski *et al.*, "High-speed data processing module for LLRF," in *Proc. 19th IEEE-NPSS Real Time Conf.*, Nara, Japan: IEEE, May 2014, pp. 1–2.

[29] W. Snyder. (2010). *Verilator: Fast, Free*. Accessed: Feb. 9, 2021. [Online]. Available: https://www.veripool.org/papers/verilator_systemperl_nascug.pdf

[30] M. Kuntzsch *et al.*, "Microtca. 4-based llrf for cw operation at elbe–status and outlook," in *Proc., 6th Int. Beam Instrum. Conf. (IBIC)*, Grand Rapids, MI, USA: JACOW, Aug. 2018, pp. 101–103.

[31] S. Pfeiffer *et al.*, "Virtual cavity probe generation using calibrated forward and reflected signals," in *Proc., 6th Int. Part. Accel. Conf. (IPAC)*. Richmond, VA, USA: JACOW, May 2015, pp. 200–202.

[32] T. Czarski, K. T. Pozniak, R. S. Romaniuk, and S. Simrock, "TESLA cavity modeling and digital implementation in FPGA technology for control system development," *Nucl. Instrum. Meth. Phys. Res. A, Accel. Spectrom. Detect. Assoc. Equip.*, vol. 556, no. 2, pp. 565–576, Jan. 2006.

[33] J. Branlard *et al.*, "Status of cryomodule testing at CMTB for CW R&D," in *Proc. 19th Int. Conf. RF Supercond. (SRF)*. Dresden, Germany: JACOW, Jun. 2019, pp. 1129–1132.

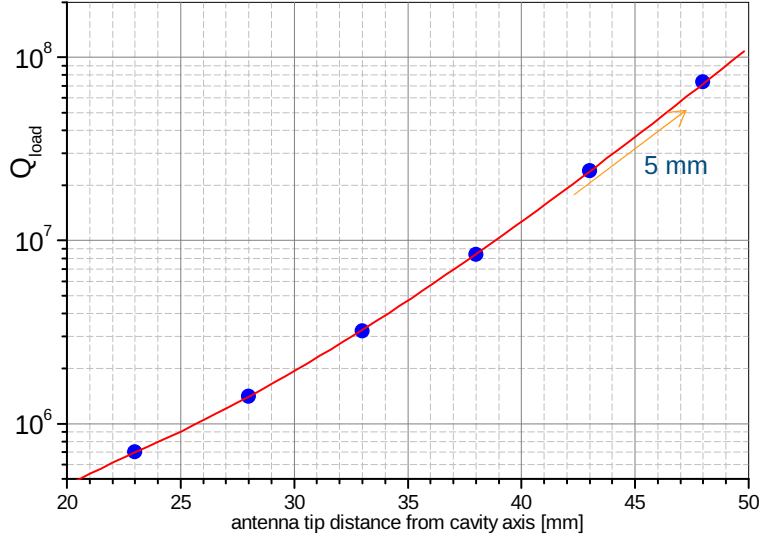## 4.2 Effects of Q_{ext} variation on LLRF calibration

Figure (4.2) Simulation of Q_L sensitivity of cavity couplers with respect to the antenna insertion depth [61]. For $Q_L = 10^7$ - 10^8 an increased sensitivity is expected compared to the range $Q_L = 10^6$ - 10^7.

For the quench detector and detuning estimator to work, it was assumed in [19] that the cavity system ADC chain is calibrated. This condition means that a constant linear transformation of the forward and reflected voltage measured by the LLRF system is found, so equation (4) of [19] holds. The general transformation that takes into account the finite directivity of the bidirectional waveguide coupler that provides the cavity signals to the LLRF is defined as [91]

$$\begin{bmatrix} V_f \\ V_r \end{bmatrix} = \begin{bmatrix} a & b \\ c & d \end{bmatrix} \begin{bmatrix} V_f^m \\ V_r^m \end{bmatrix}, \tag{4.1}$$

with V_f^m and V_r^m the measured forward and reflected voltage by the LLRF system, a,b,c,d the complex calibration constants and V_f and V_r the calibrated forward and reflected signal that fulfills the condition

$$V_c = V_f + V_r. \tag{4.2}$$

Please note that the definitions of a,b,c,d of (4.1) and [19] are different. The system remains calibrated if Q_{ext} does not change in time. However, experimental tests showed that Q_{ext} could change by more than 10% when a multi-kilowatt driving signal is used (Fig. 3.5). Such an effect is caused by the thermal expansion of the coupler inner conductor due to RF heating (Fig. 4.2). Since a recalibration requires the accelerating system to be put in pulsed mode [91], a periodic halt of CW operations might be necessary to adjust the LLRF system parameters. Even though the necessity to recalibrate the accelerating system might be negligible after the couplers reach their equilibrium temperature, alternative ways to correct the LLRF system calibration without decreasing the accelerator availability in CW are possible. To evaluate the effect of a varying Q_{ext}, a lumped model of the cavity accelerating system is used. (Fig 4.3).
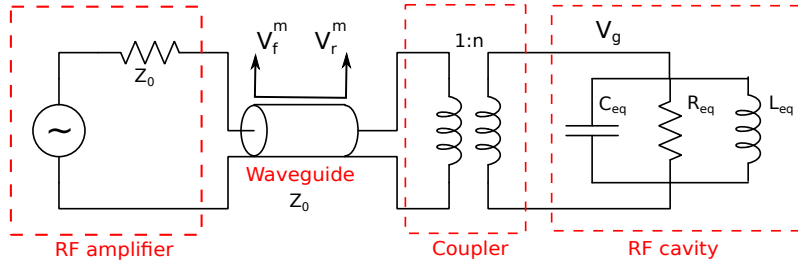
Figure (4.3) Lumped model of an RF cavity accelerating system. The RLC parallel circuit represents the RF cavity. The transformer represents the coupler with ratio $1 : n$, V_f^m, and V_r^m are the forward and reflected voltage signals read by the LLRF from a bidirectional waveguide coupler, and V_g is the generator voltage forward component that excites the RLC.

For the model, perfect directivity of the bidirectional coupler, zero electric length of the system, and no attenuation are assumed. V_f^m then represents the forward voltage of the equivalent transmission line. V_f^m is then increased by the cavity coupler, represented by a transformer, by

$$V_g = nV_f^m, \tag{4.3}$$

with n the equivalent transformer ratio of the amplifier. From [60], the relation

$$\beta = \frac{\frac{r}{Q}Q_0}{n^2 Z_0}, \tag{4.4}$$

with the waveguide impedance Z_0 and the coupling factor β

$$\beta = \frac{Q_0}{Q_{ext}} \tag{4.5}$$

gives with (4.3)

$$V_g = \sqrt{\frac{\frac{r}{Q}Q_{ext}}{Z_0}} \tilde{V}_f. \tag{4.6}$$

.

The source term for equation (2) of [19] can be corrected using (4.6)

$$I_f = \sqrt{\frac{\frac{r}{Q}Q_{ext}}{Z_0}} \, \mathrm{Re}\{V_f^m\}, \tag{4.7}$$

$$Q_f = \sqrt{\frac{\frac{r}{Q}Q_{ext}}{Z_0}} \, \mathrm{Im}\{V_f^m\}. \tag{4.8}$$

The above equations can be used when Q_{ext} changes in time as an alternative to system recalibration. In cases where differences exist in the attenuation between the two channels and the waveguide bidirectional coupler has a finite directivity, (4.6) can still be used by varying the calibration coefficients of (4.1) proportionally to $\sqrt{Q_{ext}}$. The last issue to address to correct the LLRF calibration in CW is how to calculate Q_{ext} while operating the accelerator.

One possibility could be to correlate the variations of Q_{ext} with the coupler temperature (Fig. 4.4). In the figure, two different kinds of behavior can be observed for cavities 1,3,5 and cavities 2,4,6. For cavities 1,3 and 5, the measured Q_{ext} has its maximum between $80\,\mathrm{K}$ and $90\,\mathrm{K}$, while for cavities 2,4 and 6, Q_{ext} decreases for an increasing temperature. Future tests will have to define if it is possible to derive a general relation between temperature and Q_{ext}, or if a calibration curve has to be measured for each cavity. Another possibility is to evaluate the ratio between the cavity voltage V_c and the virtual probe $V_f + V_r$. Since

$$\frac{|V_c|}{|V_f + V_r|} \propto n \propto \sqrt{Q_{ext}}, \tag{4.9}$$
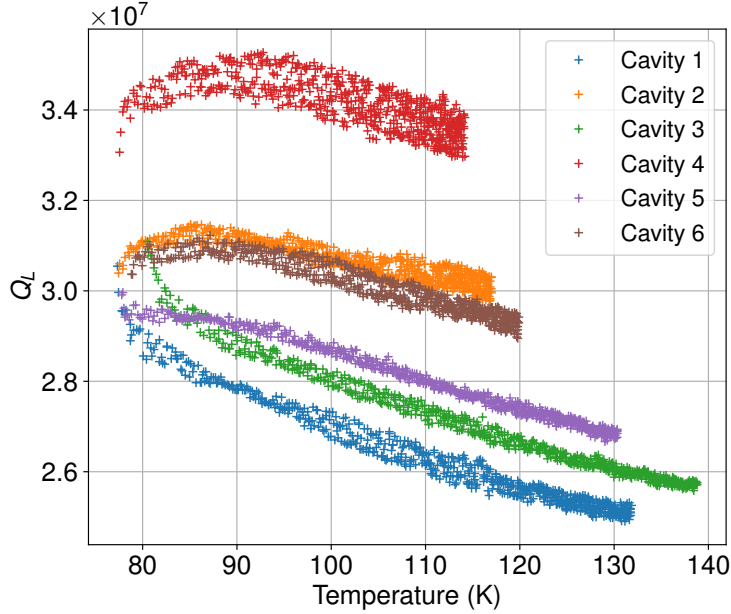
Figure (4.4)   Variation of Q_L with respect to the main coupler inner conductor temperature on six cavities. The cavities are unquenched, therefore $Q_L \simeq Q_{ext}$. The measurements were performed in pulsed mode at $P_f = 4\,\text{kW}$ and a duty factor of 50%. The Q_L was measured using the cavity field decay.

Q_{ext} can be extrapolated by varying the coupler insertion while recording pulse traces. Measurements performed at EuXFEL with $1\,\text{ms}$ long traces have shown the validity of the approach (Fig. 4.5), even though a corrected version of the virtual probe was required to improve the linearity of the estimated value

$$\frac{|V_c|}{\left|V_f + V_r e^{i\theta_r(Q_{ext})}\right|} \propto \sqrt{Q_{ext}}. \tag{4.10}$$

$\theta_r(Q_{ext})$ is the reflected signal phase correction value and is found minimizing the standard deviation of (4.10). The minimization is done by assuming that Q_{ext} does not change significantly along a single measured trace. The justification for this correction is that the electrical length of the equivalent transmission line in Fig. 4.3 depends on coupler geometry and has to be adapted for different values of the coupler insertion. The MSE error of the corrected estimation of Fig. 4.3 with respect to a linear fit is 2.5%.
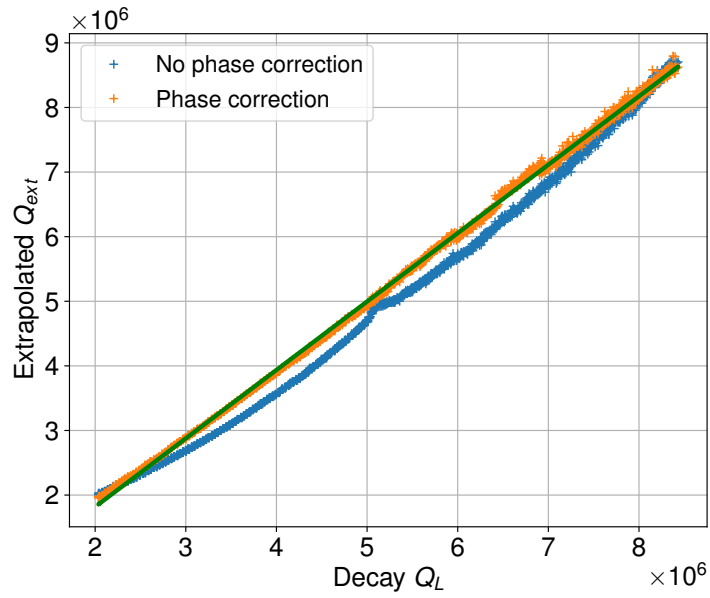
Figure (4.5)   Extrapolation of Q_{ext} using (4.9) and (4.10). The measurement was done at EuXFEL in pulsed mode. The Q_{ext} is changed by varying the coupler insertion.

Chapter 5

Ponderomotive instabilities

5.1 Cavity electromechanical model

As stated in the previous sections, one of the main challenges to overcome for the EuXFEL CW/LP upgrade is the resonance control of cavities with a $Q_L > 10^7$. Furthermore, contrary to the SP mode of operation, LP and CW mode allow ponderomotive effects to develop due to a pulse length longer than the cavity's mechanical relaxation timescale. These effects are generated by the electromechanical feedback between cavity deformations and cavity accelerating field [76]. To understand the mechanism that generates these effects, a model that describes an accelerating cavity's mechanical and electrical dynamics is needed. The RF dynamics can be calculated by a system of two differential equations that describes the in In-Phase and Quadrature (I&Q) components of the field [92].

$$\dot{V}_i = -\omega_{1/2}V_i + \Delta\omega V_q + \omega_{1/2}(V_g)_i, \tag{5.1}$$

$$\dot{V}_q = -\omega_{1/2}V_q - \Delta\omega V_i + \omega_{1/2}(V_g)_q, \tag{5.2}$$

with $V_{i/q}$ the I&Q components of the cavity accelerating voltage and $\omega_{1/2}$ and $\Delta\omega$ the cavity half bandwidth and detuning in angular frequency. For simplicity, the
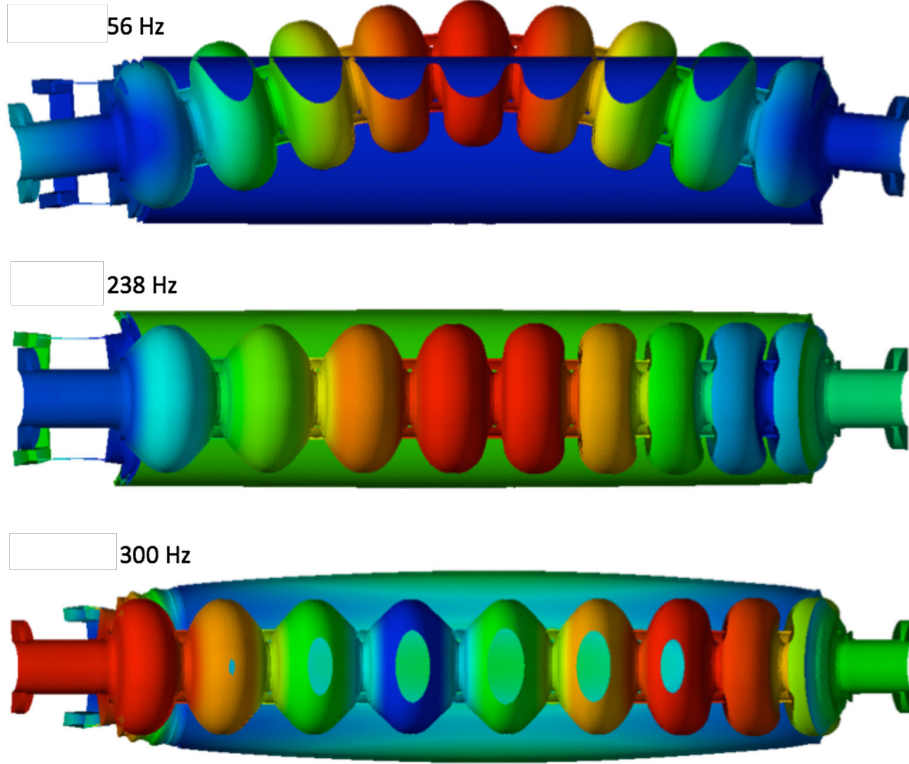
Figure (5.1) Illustrations of the structural displacements for three selected modes. The magnitudes of the displacements (a.u.) are color coded with a linear scale [93].

beam loading term is neglected. From (5.1) and (5.2) it is also possible to derive (3.16) at steady state.

For the mechanical dynamics, the cavity deformations can be decomposed in a set of cavity mechanical modes. When a mode is excited, a mode displacement $\Delta L^{(\mu)}$ is produced. Since the magnitude of these deformations is within the linear elastic limit, the modes are represented as a set of damped harmonic oscillators (Fig. 5.1,5.2)

$$\Delta \ddot{L}^{(\mu)} + \frac{\omega^{(\mu)}}{Q^\mu}\Delta \dot{L}^{(\mu)} + (\omega^{(\mu)})^2 \Delta L^{(\mu)} = (\omega^{(\mu)})^2 (F_{int}^{(\mu)} + F_{ext}^{(\mu)}). \qquad (5.3)$$

The superscript μ identifies each mode, and $\omega^{(\mu)}$ and Q^μ are the mode angular resonance frequency and quality factor. The normalized external and internal
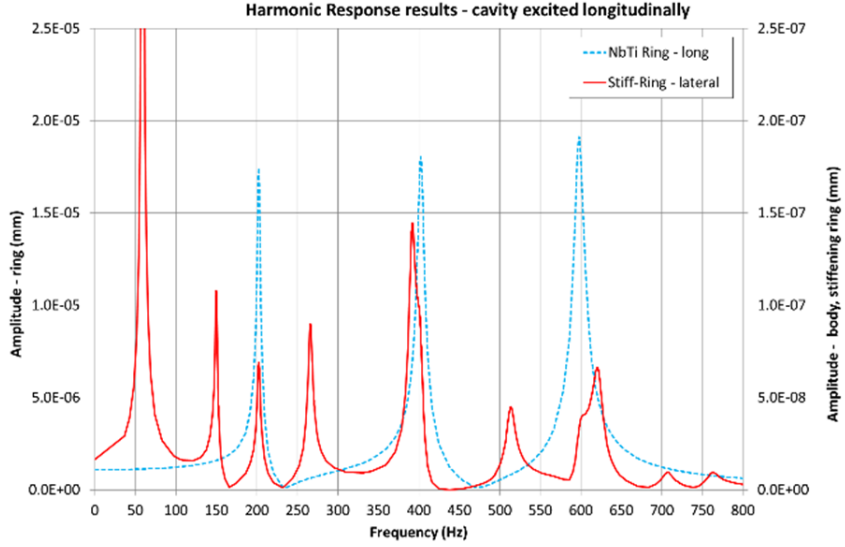
Figure (5.2)   Simulation of cavity response to a longitudinal mechanical force at different frequencies. Each peak correspods to the excitation of a cavity mode [73].

forces that drive the cavity mode are represented by $F_{ext}^{(\mu)}$ and $F_{int}^{(\mu)}$. The external forces acting on the cavity comprise the cavity tuners effect and the unwanted microphonics excitation or pressure drifts. For the internal forces, the gradient-dependent radiation pressure acts on cavity walls

$$P_{rad} = \frac{1}{4}(\epsilon_0|E|^2 + \mu_0|H|^2) \propto E_{acc}^2. \tag{5.4}$$

Therefore

$$F_{int}^{(\mu)} = \kappa^{(\mu)} E_{acc}^2. \tag{5.5}$$

When a mode is not at rest, its displacement $\Delta L^{(\mu)}$ can result in a variation of cavity volume $\Delta V^{(\mu)}$. Using Slater theorem it is possible to calculate the resulting change in cavity frequency [94, 95]

$$\frac{\Delta\Omega^{(\mu)}}{\omega_0} = \frac{\int_{\Delta V^{(\mu)}} \epsilon_0|E|^2 + \mu_0|H|^2 d\underline{\nu}}{2\int_V \epsilon_0|E|^2 + \mu_0|H|^2 d\underline{\nu}} = D^{(\mu)}\Delta L^{(\mu)}, \tag{5.6}$$

with $\Delta\Omega^{(\mu)}$ the mode detuning contribution in angular frequency and ω_0 the cavity

57

driving signal angular frequency. The cavity detuning is then

$$\Delta\omega = \Omega_\star + \sum_\mu \Omega^{(\mu)} \qquad (5.7)$$

with $\Omega_\star$ the cavity predetuning. The equations (5.5) and (5.6) define the coupling between (5.1) and (5.2), and (5.3): a cavity voltage variation results in a variation of the pressure on the cavity walls that in turns produces an excitation of the cavity mechanical modes. The displacement $\Delta L^{(\mu)}$ results in a change in the cavity RF volume that induces a detuning $\Omega^{(\mu)}$. Using (5.6) and (5.5), the mechanical dynamics equation in (5.3) can be written in terms of the RF cavity parameters

$$\ddot{\Omega}^{(\mu)} + \frac{\omega^{(\mu)}}{Q^\mu}\dot{\Omega}^{(\mu)} + (\omega^{(\mu)})^2\Omega^{(\mu)} = \omega_0 D^{(\mu)}(\omega^{(\mu)})^2\left[\kappa^{(\mu)}\frac{(V_i^2 + V_q^2)}{L^2} + F_{ext}^{(\mu)}\right], \quad (5.8)$$

with L the cavity length. With (5.8) it is possible to evaluate how the accelerating gradient variations and mechanical excitation modify the cavity tune. Additionally, (5.8) and (5.1), (5.2) are normalized with respect to the cavity RF bandwidth by dividing $\Omega^{(\mu)}$ and $\Omega_\star$ by $\omega_{(1/2)}$ as in (3.14). The transformed equations are

$$\begin{aligned}
\dot{V}_i &= \omega_{1/2}\left[-V_i + yV_q + (V_g)_i\right], \\
\dot{V}_q &= \omega_{1/2}\left[-V_q - yV_i + (V_g)_q\right], \\
y &= y_\star + \sum_\mu y^{(\mu)},
\end{aligned} \qquad (5.9)$$

$$\ddot{y}^{(\mu)} + \frac{\omega^{(\mu)}}{Q^\mu}\dot{y}^{(\mu)} + (\omega^{(\mu)})^2 y^{(\mu)} = (\omega^{(\mu)})^2\left[u_m^{(\mu)} + K_{lfd}^{(\mu)}(V_i^2 + V_q^2)\right],$$

with

$$y_\star = \frac{\Omega_\star}{\omega_{1/2}}, \qquad (5.10)$$

$$y^{(\mu)} = \frac{\Omega^{(\mu)}}{\omega_{1/2}}, \qquad (5.11)$$

$$K_{lfd}^{(\mu)} = \frac{\omega_0}{\omega_{1/2}L^2}D^{(\mu)}\kappa^{(\mu)}, \qquad (5.12)$$

$$u_m^{(\mu)} = \frac{\omega_0}{\omega_{1/2}}D^{(\mu)}F_{ext} \qquad (5.13)$$

The equation system (5.9) is nonlinear due to the coupling terms yV_i, yV_q and $K_{lfd}^{(\mu)}(V_i^2 + V_q^2)$. Due to difficulties in finding an analytical solution of (5.9), the

electromechanical cavity model has to be approximated to simpler systems when studying ponderomotive effects that are present in SRF resonators.

5.2   Monotonic instability

From (5.9) it is possible to derive the monotonic instability by studying the equations at steady state. Therefore all time derivatives are set to zero and

$$V_{acc}^2(y^2 + 1) = V_g^2, \tag{5.14}$$

$$y = y_\star + \sum_\mu K_{lfd}^{(\mu)} V_{acc}^2 = y_\star + K_{lfd} V_{acc}^2. \tag{5.15}$$

Using (5.15) in (5.14) gives a quadratic equation in $y_\star$

$$y_\star^2 V_{acc}^2 + 2y_\star K_{lfd}^2 V_{acc}^4 + V_{acc}^2(1 + K_{lfd}^2 V_{acc}^4) - V_g^2 = 0. \tag{5.16}$$

Solving (5.16) for $y_\star$ gives

$$y_\star^\pm = -K_{lfd} V_{acc}^2 \pm \sqrt{\frac{V_g^2}{V_{acc}^2} - 1}. \tag{5.17}$$

(5.17) relates the predetuning with the cavity accelerating gradient (Fig. 5.3).

The two solutions of (5.17) are connected at resonance where $V_g = V_{acc}$ and $y_\star^+ = y_\star^- = -K_{lfd} V_g^2$. $y_\star^+$ and $y_\star^-$ represent the left and right sides of the resonance curve. For increasing values of V_g, and a negative value of K_{lfd}, $y_\star^+$ bends until a minimum is generated. When such condition happens $y_\star^+$ is not mathematically monotonic and multiple values of V_{acc}^2 are possible for a certain $y_\star$. This coincides with the presence of the motonic instability. To evaluate the occurrence of such an instability, the derivative $\frac{dy_\star^+}{dV_{acc}}$ has to be tested for the presence of a zero

$$0 = \frac{dy_\star^+}{dV_{acc}} = -\frac{V_g^2}{V_{acc}^3 \sqrt{\frac{V_g^2}{V_{acc}^2} - 1}} - 2K_{lfd} V_{acc} \rightarrow \tag{5.18}$$

$$0 = 4K_{lfd} V_{acc}^8 + 4K_{lfd} V_{acc}^6 V_g^2 - V_g^4. \tag{5.19}$$
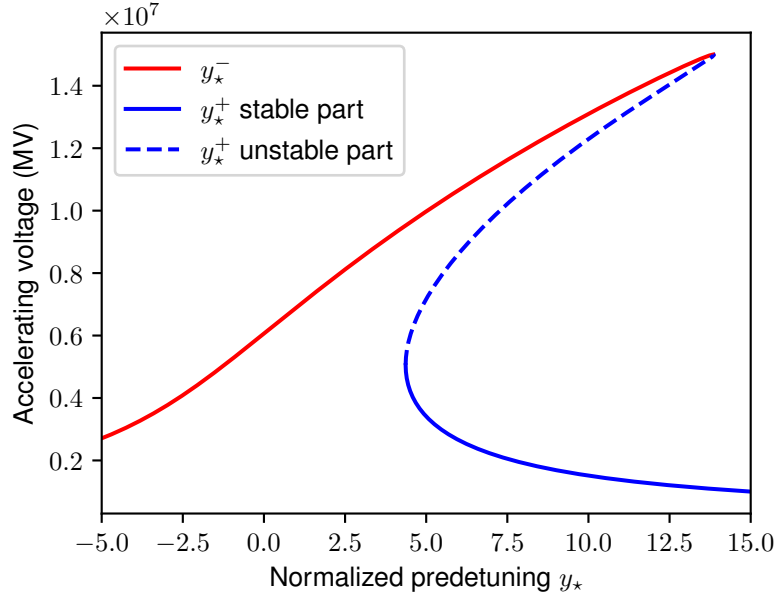
Figure (5.3) Resonance curve affected by monotonic instability. $Q_L = 4 \cdot 10^7$ and $V_g = 15\,\text{MV}$. The $y_\star^-$ and $y_\star^+$ parts of the curve are highlighted.

The condition for having a real root in (5.19) for V_{acc} is

$$27K_{lfd}^8 V_g^{16} - 64K_{lfd}^6 V_g^{12} > 0 \rightarrow \qquad (5.20)$$

$$-K_{lfd}V_g^2 > \sqrt{\frac{64}{27}} \simeq 1.54. \qquad (5.21)$$

When the above condition is valid, an instability interval in the resonance curve is present. In this interval three values of V_{acc} are possible for $y_\star$: one comes from $y_\star^-$ and two from $y_\star^+$. Schulze [76] demonstrated that the part of $y_\star^+$ at the highest gradient is an unstable solution, whereas the lowest gradient part of $y_\star^+$ and $y_\star^-$ are stable solutions for (5.9). Such a result is found by studying the potential of the cavity mechanical modes(Fig. 5.4). It is also possible to show that $y_\star^-$ in the proximity of the resonance has a higher mechanical potential than the stable part of $y_\star^-$ and a vanishing energy well. As a consequence, a mechanical excitation can make the system jump from $y_\star^-$ to $y_\star^+$. Such jump is referred in the literature as a *static drop*.

When a static drop happens, the cavity is detuned by $y \simeq -K_{lfd}V_g^2$. Since, for a TESLA cavity with a $Q_L = 3 \cdot 10^7$, $K_{lfd} \simeq 0.046\,(\text{MV})^{-2}$ and for $V_g = 15\,\text{MV}$,
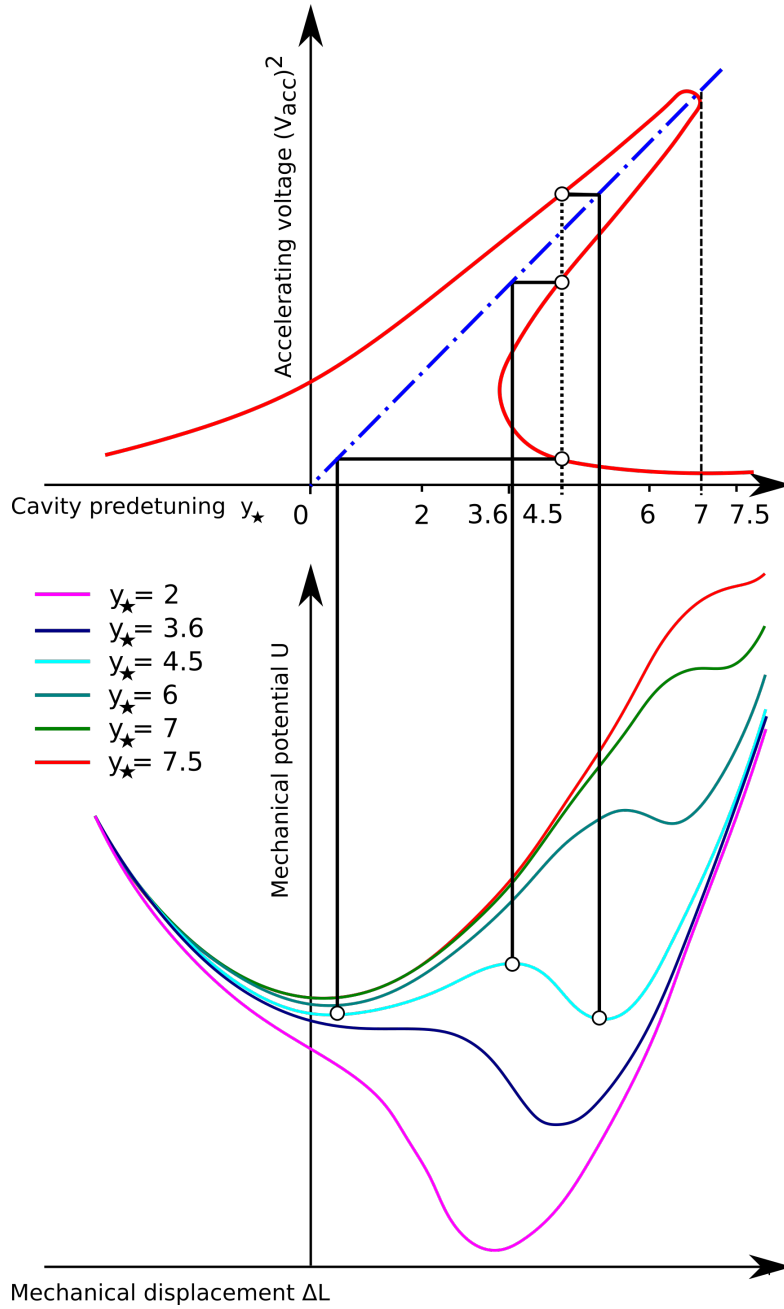
Figure (5.4)   Elastic potential for a cavity system affected by the monotonic instability [76]. The potential is a function of the mechanical displacement ΔL. $K_{lfd}V_g^2 = -7$.

$-K_{lfd}V_g^2 \simeq 10$. Therefore if the cavity experiences a static drop, then it gets detuned by around ten times its cavity half-bandwidth.

5.3 Integral Resonance Control in Continuous Wave Superconducting Particle Accelerators

The monotonic instability in superconducting cavities has severe consequences for the particle accelerator availability if triggered since it results in an unacceptable increase in driving power. Therefore machine operations must be stopped to retune the resonators. It is mandatory to find a method to reduce the occurrence of such an issue. In the following proceeding, a technique that uses the fast piezoelectric tuner of the TESLA superconducting cavities installed at EuXFEL to prevent triggering the monotonic instability is presented.

Integral Resonance Control In Continuous Wave Superconducting Particle Accelerators

A. Bellandi * J. Branlard * A. Eichler * S. Pfeiffer *

* Deutsches Elektronen-Synchrotron (DESY), Hamburg 22607
Germany
(andrea.bellandi@desy.de, julien.branlard@desy.de,
annika.eichler@desy.de, sven.pfeiffer@desy.de)

Abstract: Superconducting accelerating cavities for continuous wave low-current particle accelerators requires a tight resonance control to optimize the RF power costs and to minimize the beam delivery downtime. When the detuning produced by radiation pressure becomes comparable to the RF bandwidth, the monotonic instability starts to affect the cavity operation. When this instability is triggered by external vibrations or drifts, the accelerating field amplitude drops rapidly, and the beam acceleration has to be stopped. Past experiments showed that using an integral control of the piezoelectric tuners installed on the cavity prevents the adverse effects of the monotonic instability. This paper derives theoretically why an integral controller is an effective way to counteract the monotonic instability. To perform the study a linearized state-space model of the cavity is derived. Simulations and experiments in a superconducting test facility indicate that the use of this kind of control has the additional benefit of bringing the cavities to the resonance condition automatically.

Keywords: Particle accelerators, Control systems, Parametric resonances, Electromagnetic devices

1. INTRODUCTION

Superconducting Radio-Frequency (SRF) Continuous Wave (CW) electron linear accelerators are increasingly interesting for their scientific and industrial applications ranging from X-ray and UV laser generation for experimental and medical uses (Sekutowicz et al. (2015); Zhu et al. (2017); Raubenheimer (2018); Serafini et al. (2019)), short-lived isotope production for medicine and industry (Habs and Köster (2011)), and semiconductor lithography (Nakamura et al. (2015)). The main components of this kind of machines are the superconducting resonant RF cavities. When an electron bunch passes through an RF cavity, it gets accelerated by the inner electric field, thus absorbing part of the stored electromagnetic energy. To maximize the RF efficiency accelerating cavities are driven at or near the resonance frequency of the accelerating mode. Superconducting cavities possess an RF surface resistance of a factor 10^5 lower compared to their normal conducting counterparts. Therefore, they can operate continuously at fields over $10\,\mathrm{MV\,m^{-1}}$ without enduring a mechanically damaging thermal dissipation or needing excessive RF power expenditures. Cryogenic temperatures are needed to maintain the superconducting state of this kind of cavities. Therefore to maximize the thermal exchange, the superconducting cavities are operated in a liquid or superfluid helium bath. The ability of a certain cavity to retain the RF field with low power dissipation is usually given in terms of the *intrinsic quality factor* (Q_0). The Q_0 is equal to the cavity stored electromagnetic energy multiplied by two times Pi over the amount of energy dissipated in one

RF period. TESLA is one of the type of superconducting cavities, which is most frequently used in electron accelerators. This type of resonator has a design resonant frequency of $1.3\,\mathrm{GHz}$, and state-of-the-art TESLA cavities have a Q_0 that exceed $2 \cdot 10^{10}$. To match the cavity with the beam loading and to optimize the RF budget, the required quality factor for operations or *loaded quality factor* (Q_L) is usually lower than the intrinsic one. In low-current SRF CW accelerators based on TESLA cavities a Q_L higher than 10^7 is generally used, that results in a system bandwidth of some tens of Hertz (Padamsee et al. (2008)). Such a narrow bandwidth makes the cavity field very sensitive to disturbances that deforms its geometry in the micron range. These detuning disturbances can originate from the accelerating field radiation pressure, the Lorentz Force Detuning (LFD), and external mechanical disturbances (microphonics). Detuning disturbances make it harder to keep the cavity resonance frequency at a fixed value and have to be compensated. Moreover, when the LFD is comparable to the cavity bandwidth, an instability, the monotonic instability, might cause a loss of gradient if the resonance frequency is not tightly controlled (Schulze (1972)). Therefore, piezoelectric tuners are used when an online correction of the cavity resonance frequency is required. In Section 2, the impact of the monotonic instability on operations is explained and a electromechanical state-space model of a resonant cavity (useful to design a resonance controller) is derived. The parameters used in the model are the ones that are foreseen for the CW upgrade of the European X-Ray Free Electron Laser (EuXFEL), a short pulse superconducting accelera-

tor used to produce high intensity hard X-rays to perform various physical, chemical and biological investigations. In Section 3, the stability conditions of the system, when an integral control on the piezoelectric tuner is applied, are presented. An evaluation of the controller behavior for heavily detuned systems is also presented. In Section 4, the capability of the controller of bringing the system to resonance and preventing the occurrence of the monotonic instability disturbances is evaluated experimentally on multiple TESLA acceleration cavities.

2. CAVITY MODEL

To understand how detuning affects the operation of superconducting cavities, an electro-mechanical model of the cavity has to be derived.

2.1 Electrical model

The following first-order matrix differential equation represents an electrical baseband description of an RF cavity (Schilcher (1998))

$$\dot{\underline{\mathbf{v}}} = \omega_{1/2} \begin{bmatrix} -1 & y \\ -y & -1 \end{bmatrix} \underline{\mathbf{v}} + \begin{bmatrix} \omega_{1/2} \\ 0 \end{bmatrix} V_g, \qquad (1)$$

with

$$\underline{\mathbf{v}} = \begin{bmatrix} V_r \\ V_i \end{bmatrix}, \quad |\underline{\mathbf{v}}| = E_{acc}L, \quad y = 2Q_L\frac{\Delta f}{f_0} \qquad (2)$$

Here, V_r and V_i are the in-phase and quadrature part of the cavity accelerating voltage $\underline{\mathbf{v}}$, E_{acc} is the accelerating field, L is the cavity length, y is the detuning factor, f_0 is the design resonant frequency and Δf is the detuning. The generator induced voltage V_g is supposed to be constant and in-phase to simplify the derivations. The detuning factor y can be written as the sum of the cavity predetuning $y_\star$ and the contributions of the cavity mechanical modes driven by LFD or other external forces

$$y = y_\star + \sum_{\mu=1}^{N} y^{(\mu)} = \frac{(2\pi f_0 - \omega_u)}{\omega_{1/2}} + \frac{(\omega_u - \omega_c)}{\omega_{1/2}},$$

$$y_\star = \frac{(2\pi f_0 - \omega_u)}{\omega_{1/2}}, \quad \sum_{\mu=1}^{N} y^{(\mu)} = \frac{(\omega_u - \omega_c)}{\omega_{1/2}}, \qquad (3)$$

with the angular resonant frequency of the cavity ω_c, the resonant frequency of the predetuned cavity at rest ω_u, the cavity half bandwidth $\omega_{1/2}$, and $y^{(\mu)}$ the detuning contribution produced by the mode $\mu \in [1, \dots, N]$.

2.2 Mechanical model

The mechanical model of the cavity can be represented by a a set of second-order differential equations (Schulze (1972)). Each equation is a particular mechanical mode of the resonator structure:

$$\dot{\underline{\mathbf{y}}}^{(\mu)} = \mathbf{A_m}^{(\mu)}\underline{\mathbf{y}}^{(\mu)} + \mathbf{B_m}^{(\mu)}(u_m^{(\mu)} + K_{lfd}^{(\mu)}|\underline{\mathbf{v}}|^2),$$

$$\underline{\mathbf{y}}^{(\mu)} = \begin{bmatrix} y^{(\mu)} \\ \dot{y}^{(\mu)} \end{bmatrix}, \quad \mathbf{A_m}^{(\mu)} = \begin{bmatrix} 0 & 1 \\ -(\omega^{(\mu)})^2 & -\frac{\omega^{(\mu)}}{Q^{(\mu)}} \end{bmatrix}, \qquad (4)$$

$$\mathbf{B_m}^{(\mu)} = \begin{bmatrix} 0 \\ (\omega^{(\mu)})^2 \end{bmatrix}, \quad K_{lfd}^{(\mu)} = \frac{2\pi k_{lfd}^{(\mu)}}{L^2\omega_{1/2}}.$$

In the above equation $\omega^{(\mu)}$ is the mechanical mode angular resonant frequency, $Q^{(\mu)}$ is the mode quality factor,

$K_{lfd}^{(\mu)}$ is the normalized LFD constant, $k_{lfd}^{(\mu)}$ is the LFD constant in Hz/(MVm^{-1})^2. The input $u_m^{(\mu)}$ represents the time-dependent external mechanical forces produced by microphonics and the fast tuner on the cavity. For SRF cavities $K_{lfd}^{(\mu)}$ and $k_{lfd}^{(\mu)}$ are always less than zero because of the Slater's theorem and radiation pressure (Slater (1946); Liepe (2001)). The electrical and mechanical model, (1) and (4), are coupled through the detuning factor y and the squared amplitude of the cavity voltage $|\underline{\mathbf{v}}|^2$.

2.3 Zero-order approximation

A first step towards understanding the effects arising from the coupling of (1) and (4) is to perform a steady-state analysis: the derivative terms are set to zero, whereas the steady-state values are denoted with the zero ("0") subscript. For (1) the following equations are obtained

$$|\underline{\mathbf{v}}_0|^2 = \frac{V_g^2}{1 + y_0^2}, \quad y_0 = -\frac{V_{i0}}{V_{r0}} = -\tan(\theta_0), \qquad (5)$$

with θ_0 as the phase angle of the cavity voltage. For the mechanical equations of (4) it results in

$$K_{lfd} = \sum_{\mu=1}^{N} K_{lfd}^{(\mu)}, \quad \sum_{\mu=1}^{N} y_0^{(\mu)} = K_{lfd}|\underline{\mathbf{v}}_0|^2, \qquad (6)$$

where K_{lfd} is the total normalized LFD constant of the cavity. Using (5) and (6) with the definition of the detuning parameter in (3) leads to the following equation

$$y_\star = -K_{lfd}|\underline{\mathbf{v}}_0|^2 \pm \sqrt{\frac{V_g^2}{|\underline{\mathbf{v}}_0|^2} - 1}, \qquad (7)$$

and evaluating (7) at resonance ($|\underline{\mathbf{v}}_0| = V_g$, $y_0 = 0$) gives

$$(y_\star)_{res} = -K_{lfd}V_g^2, \qquad (8)$$

with $(y_\star)_{res}$ the predetuning that has to be applied to the cavity to achieve the resonance condition.

2.4 Monotonic instability

The result of (8) shows that the steady-state cavity behaviour is driven by the term $K_{lfd}|V_g|^2$:

case I: $|K_{lfd}V_g|^2 \ll 1$. The LFD has a low impact and the cavity resonant frequency can be considered independent from the accelerating gradient.

case II: $|K_{lfd}V_g|^2 \gg 1$. The LFD frequency deviation is higher than the cavity half bandwidth and a variation in cavity gradient produces a sensible variation in the detuning.

In Fig. 1 resonance curves for different values of $K_{lfd}V_g^2$ are displayed. As it can be seen, above a threshold of $K_{lfd}V_g^2$ multiple steady-state solutions of the amplitude and phase for a singular value of y appear for (7). Such threshold is $K_{lfd}V_g^2 < -1.54$ and determines the presence of the *monotonic instability* (Schulze (1972)). Due to the presence of the instability, the system may experience significant amplitude and phase jumps if the detuning is changed in a way that a discrete variation of the cavity parameters is required to reach a stable solution of (7) (Fig. 3). One consequence is that if the cavity is driven
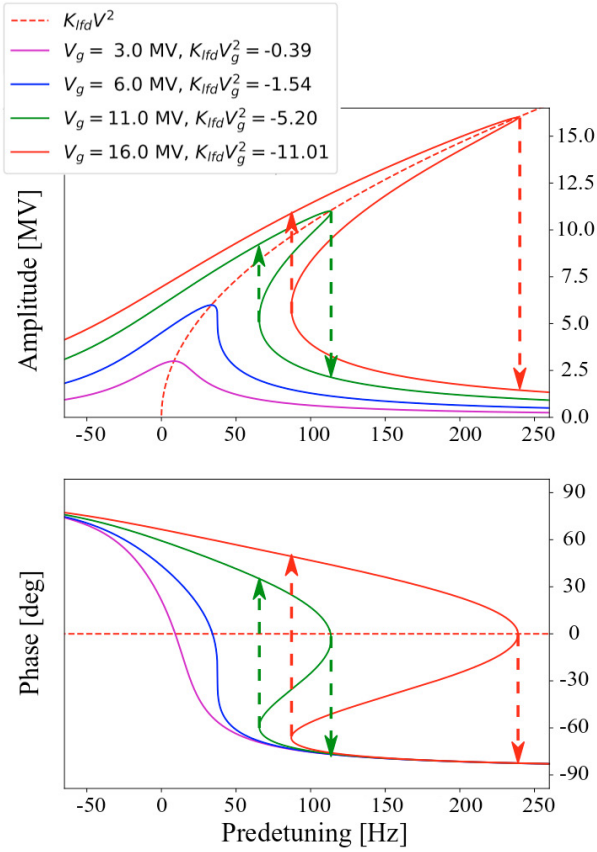
Fig. 1. Static LFD effects on SRF TESLA cavities with $Q_L = 3 \times 10^7$ and the LFD constant $k_{\text{lfd}} = -1\,\text{Hz}/(\text{MVm}^{-1})^2$. For $K_{\text{lfd}}V_g^2 < -1.54$ the cavity is affected by the monotonic instability. Monotonic drop thresholds are indicated by arrows that points downwards. Inverse monotonic drops point upwards.

near resonance, an external disturbance can trigger the instability and make the cavity gradient to incur in a *static drop*. Such an effect is unwanted due to the need to recover the gradient inside the cavity to continue the beam acceleration. A jump in the opposite direction is the *inverse static drop*. For the EuXFEL CW upgrade TESLA cavities have a target design value of k_{lfd} equal to $-1\,\text{Hz}/(\text{MV})^2$, $L = 1.038\,\text{m}$, Q_L higher than $3 \cdot 10^7$ and a maximum E_{acc} of $16\,\text{MV}\,\text{m}^{-1}$. For these parameters it is $K_{lfd}V_g^2 < -11.8$ and the presence of the monotonic instability is expected.

2.5 First order approximation

A way to find out when a monotonic drop happens is to derive a small-signal state-space representation of (1) and (4) and study when the stability conditions are met. In the following, the small gain quantity of a variable x is denoted by δx.

The small-gain representation of (1) is given by

$$\delta \dot{\underline{\mathbf{v}}} = \omega_{1/2} \begin{bmatrix} -1 & y_0 \\ -y_0 & -1 \end{bmatrix} \delta \underline{\mathbf{v}} - \frac{\omega_{1/2} V_g}{1+y_0^2} \begin{bmatrix} y_0 & 0 \\ 1 & 0 \end{bmatrix} \sum_{\mu=1}^{N} \delta \underline{\mathbf{y}}^{(\mu)}, \quad (9)$$

and that of (4) by

$$\delta \dot{\underline{\mathbf{y}}}^{(\mu)} = \mathbf{A}_{\mathbf{m}}^{(\mu)} \delta \underline{\mathbf{y}}^{(\mu)} + \mathbf{B}_{\mathbf{m}}^{(\mu)} u^{(\mu)} + \mathbf{G}^{(\mu)} \delta \underline{\mathbf{v}} \quad (10)$$

with

$$\mathbf{G}^{(\mu)} = \frac{2(\omega^{(\mu)})^2 K_{\text{lfd}}^{(\mu)} V_g}{1+y_0^2} \begin{bmatrix} 0 & 0 \\ 1 & -y_0 \end{bmatrix}. \quad (11)$$

$\mathbf{G}^{(\mu)}$ is a matrix that couples the field variations to the detuning variations. Then, using (9) and (10), a state transformation is applied to get an amplitude-phase representation with the following transformation matrix

$$\mathbf{T_{ap}} = \begin{bmatrix} \dfrac{\partial a}{\partial V_r} & \dfrac{\partial a}{\partial V_i} \\ \dfrac{\partial \theta}{\partial V_r} & \dfrac{\partial \theta}{\partial V_i} \end{bmatrix} = \frac{1}{V_g} \begin{bmatrix} 1 & -y_0 \\ y_0 & 1 \end{bmatrix}, \quad (12)$$

such that

$$\begin{bmatrix} \delta a \\ \delta \theta \end{bmatrix} = \mathbf{T_{ap}} \delta \underline{\mathbf{v}}, \quad (13)$$

where δa is the amplitude variation normalized to its steady-state value. Using the derived small-signal equations it is possible to write a state-space system in the form

$$\dot{\underline{\mathbf{x}}} = \mathbf{A}\underline{\mathbf{x}} + \mathbf{B}\underline{\mathbf{u}}. \quad (14)$$

The state matrix $\mathbf{A} \in \mathbb{R}^{2(N+1) \times 2(N+1)}$ is defined as

$$\mathbf{A} = \begin{bmatrix} \mathbf{A_e} & \mathbf{H} & \mathbf{H} & \dots & \mathbf{H} \\ \hat{\mathbf{G}}^{(1)} & \mathbf{A_m^{(1)}} & \mathbf{0} & \dots & \mathbf{0} \\ \hat{\mathbf{G}}^{(2)} & \mathbf{0} & \mathbf{A_m^{(2)}} & \ddots & \vdots \\ \vdots & \vdots & \ddots & \ddots & \mathbf{0} \\ \hat{\mathbf{G}}^{(N)} & \mathbf{0} & \dots & \mathbf{0} & \mathbf{A_m^{(N)}} \end{bmatrix}, \quad (15)$$

with

$$\mathbf{A_e} = \omega_{1/2} \begin{bmatrix} -1 & y_0 \\ -y_0 & -1 \end{bmatrix}, \quad \mathbf{H} = \omega_{1/2} \begin{bmatrix} 0 & 0 \\ -1 & 0 \end{bmatrix}, \quad (16)$$

and

$$\hat{\mathbf{G}}^{(\mu)} = \frac{2(\omega^{(\mu)})^2 K_{\text{lfd}}^{(\mu)} V_g^2}{1+y_0^2} \begin{bmatrix} 0 & 0 \\ 1 & 0 \end{bmatrix}. \quad (17)$$

The input matrix $\mathbf{B} \in \mathbb{R}^{2(N+1) \times N}$ is

$$\mathbf{B} = \begin{bmatrix} \mathbf{0} & \mathbf{0} & \dots & \mathbf{0} \\ \mathbf{B_m}^{(1)} & \mathbf{0} & \dots & \mathbf{0} \\ \mathbf{0} & \mathbf{B_m}^{(2)} & \ddots & \vdots \\ \vdots & \ddots & \ddots & \mathbf{0} \\ \mathbf{0} & \dots & \mathbf{0} & \mathbf{B_m}^{(N)} \end{bmatrix}. \quad (18)$$

$\underline{\mathbf{x}} \in \mathbb{R}^{2(N+1)}$ and $\underline{\mathbf{u}} \in \mathbb{R}^N$ represent the state and the input vector, by

$$\underline{\mathbf{x}} = \begin{bmatrix} \delta a \\ \delta \theta \\ \delta \underline{\mathbf{y}}^{(1)} \\ \vdots \\ \delta \underline{\mathbf{y}}^{(N)} \end{bmatrix}, \quad \underline{\mathbf{u}} = \begin{bmatrix} u^{(1)} \\ \vdots \\ u^{(N)} \end{bmatrix}. \quad (19)$$

Measuring $Q^{(\mu)}$ and $k_{\text{lfd}}^{(\mu)}$ for each cavity is not straightforward and instead of relying on a precise model of the cavity, a further assumption is made to simplify the system: the mechanical resonant frequencies are supposed to be at approximately an order of magnitude larger than the resonance half bandwidth of the cavity. Such an assumption is supported by the values reported in literature (Czarski et al. (2006)). Then, for frequencies lower than $\omega_{1/2}$ the derivative terms of the mechanical detuning contributions

$\delta\dot{\mathbf{y}}^{(\mu)}$ can be approximated to zero and the detuning error contributions $\delta\mathbf{y}^{(\mu)}$ can be redefined as

$$\delta\mathbf{y}^{(\mu)} = -\left(\mathbf{A_m}^{(\mu)}\right)^{-1}\left[\hat{\mathbf{G}}^{(\mu)}\underline{\mathbf{x_r}} + \mathbf{B}^{(\mu)}u^{(\mu)}\right] \quad (20)$$

with

$$\underline{\mathbf{x_r}} = \begin{bmatrix} \delta a \\ \delta\theta \end{bmatrix}. \quad (21)$$

As a consequence, (19) can be reduced to a second order system incorporating the terms that depends on K_{lfd} in the electrical part of the system matrix given as

$$\dot{\underline{\mathbf{x}}}_{\mathbf{r}} = \mathbf{A_e}\underline{\mathbf{x_r}} - \mathbf{H}\sum_{\mu=1}^{N}\left(\mathbf{A_m}^{(\mu)}\right)^{-1}\left[\hat{\mathbf{G}}^{(\mu)}\mathbf{x_r} + \mathbf{B}^{(\mu)}u^{(\mu)}\right]. \quad (22)$$

With (3), (11) and (16), the reduced system (22) can be defined as

$$\dot{\underline{\mathbf{x}}}_{\mathbf{r}} = \mathbf{A_r}\mathbf{x_r} + \mathbf{B_r}u_r \quad (23)$$

with

$$\mathbf{A_r} = \mathbf{A_e} - \mathbf{H}\sum_{\mu=1}^{N}\left(\mathbf{A_m}^{(\mu)}\right)^{-1}\hat{\mathbf{G}}^{(\mu)}, \quad (24)$$

$$= \mathbf{A_e} - \omega_{1/2}\frac{2K_{\text{lfd}}V_g^2}{1+y_0^2}\begin{bmatrix} 0 & 0 \\ 1 & 0 \end{bmatrix} \quad (25)$$

and

$$\mathbf{B_r} = \mathbf{H}\sum_{\mu=1}^{N}\left(\mathbf{A_m}^{(\mu)}\right)^{-1}\mathbf{B}^{(\mu)} = \omega_{1/2}\begin{bmatrix} 0 \\ 1 \end{bmatrix}. \quad (26)$$

The term u_r represents the total mechanical perturbation and is defined as

$$u_r = \sum_{\mu=1}^{N}u^{(\mu)} \quad (27)$$

The system in (23) is stable if the eigenvalues of $\mathbf{A_r}$ have a negative real part. This is equivalent to satisfy the following inequality

$$\beta = y_0\left(y_0 + \frac{2K_{\text{lfd}}V_g^2}{1+y_0^2}\right) \geq -1. \quad (28)$$

A stability limit can be found studying (28) near the resonance. In such case a small value of the detuning and a big contribution of LFD is assumed ($|y_0| \ll 1 \ll |2K_{\text{lfd}}V_g^2|$). This simplification leads to the monotonic stability condition

$$y_0 \leq -\frac{1}{2K_{\text{lfd}}V_g^2}. \quad (29)$$

This means that for the EuXFEL CW upgrade, an increase of the detuning of 0.96 Hz can trigger a monotonic drop when driving the cavities at resonance. Therefore, given that such stability can hardly be assured due to pressure drifts, a controller has to be added to prevent the occurrence of monotonic drops.

3. INTEGRAL CONTROL

Using piezo tuners with an integral control policy was already experimentally reported as a successful technique to compensate detuning errors for $Q_L = 1.5 \cdot 10^7$ (Rybaniec et al. (2017)). Here, we want to theoretically derive stability conditions for such a controller and study its

behavior in the presence of a strong monotonic instability. The usage of a pure integral control is justified by the presence of high mechanical resonances $Q^{(\mu)}$ that limit the usage of a proportional controller. For this analysis (23) can be used as a starting point to derive the stability conditions. For the piezo tuners an integral control policy is given by

$$p = p_{t=t_0} + K_I\omega_{1/2}\int_{t_0}^{t}\delta\theta dt. \quad (30)$$

In the equation above p the piezoelectric tuner input and K_I the gain of the integrating feedback. The produced mechanical effect on each mechanical mode of the cavity can be described defining $u^{(\mu)}$ as

$$u^{(\mu)} = g^{(\mu)}p + m^{(\mu)}, \quad (31)$$

where $g^{(\mu)}$ is the coupling constant of the mechanical tuner to the mode μ, and $m^{(\mu)}$ is the microphonic contribution. In the following pages, the coupling constant $g^{(\mu)}$ is assumed to be larger than zero. For the model of the cavity system controlled by the feedback the total amount of mechanical coupling g and the total microphonic contribution m have to be taken into account, given as

$$g = \sum_{\mu=1}^{N}g^{(\mu)}, \quad m = \sum_{\mu=1}^{N}m^{(\mu)}. \quad (32)$$

Substituting the integral control law (31) into (27) and then into (23) gives the following closed-loop matrix differential equation

$$\dot{\underline{\mathbf{x}}}_{\mathbf{f}} = \mathbf{A_f}\underline{\mathbf{x_f}} + \mathbf{B_f}m \quad (33)$$
$$\quad (34)$$

with

$$\mathbf{A_f} = \omega_{1/2}\begin{bmatrix} -1 & y_0 & 0 \\ \beta/y_0 & -1 & g \\ 0 & K_I & 0 \end{bmatrix}, \quad \mathbf{x_f} = \begin{bmatrix} \delta a \\ \delta\theta \\ p \end{bmatrix}, \quad (35)$$

and

$$\mathbf{B_f} = \omega_{1/2}\begin{bmatrix} 0 \\ 1 \\ 0 \end{bmatrix}. \quad (36)$$

The stability of (33) can be derived studying the eigenvalues of the system matrix $\mathbf{A_f}$. Then, given the following assumptions

A.1: the electric source term V_g is constant,

A.2: the dynamics of the cavity is described by (14),

A.3: $\omega_{1/2} \ll \omega^{(\mu)}$,

A.4: the feedback delay is negligible compared to $1/\omega_{1/2}$,

a stability condition can then be expressed by

$$K_I \geq \begin{cases} 0 & \text{for} \quad (\beta+1) > 0 \\ -2\frac{(\beta+1)}{g} & \text{for} \quad (\beta+1) \leq 0 \end{cases}. \quad (37)$$

The solution above shows that the system stability is achieved only for positive values of K_I. An attractive property of the closed-loop system is that with a non-zero value of the integrator gain K_I, the system is stable for values of β that are lower than minus one. Therefore, using an appropriate integral gain K_I, it is possible to drive the cavities at otherwise unstable conditions (see (28)).
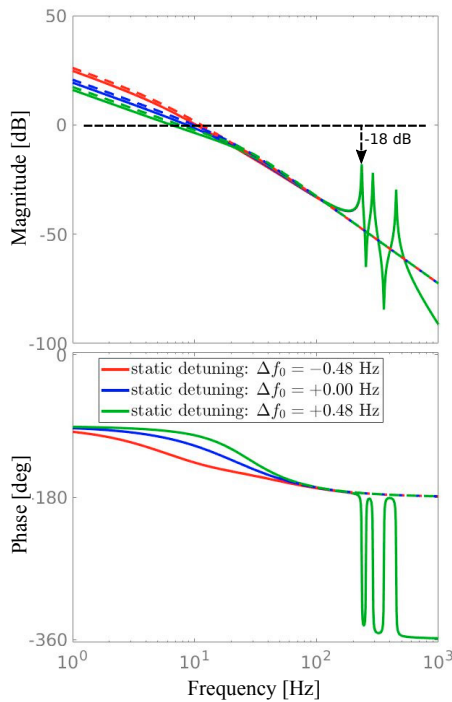
Fig. 2. Loop transfer functions for (14) (continuous lines) and simplified mode-less one (23) (dotted lines). $Q_L = 3 \cdot 10^7$
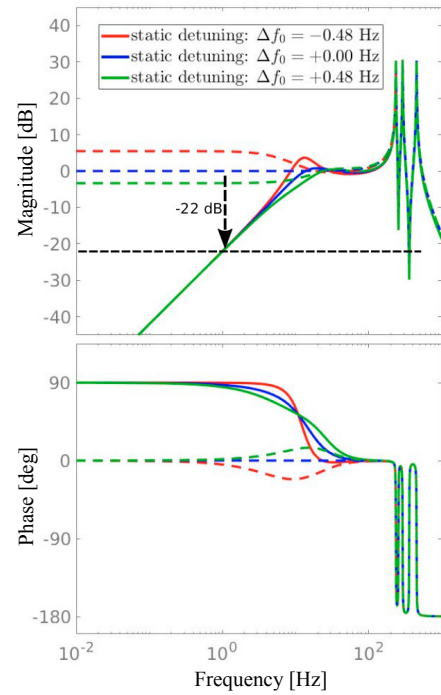

Fig. 3. Comparison between open-loop (dotted lines) and closed-loop (continuous lines) transfer functions from the external mechanical disturbance to the detuning factor y.

Nonetheless, one should keep in mind that the mechanical resonances neglected in the derivation of (33) limit the maximum value of the feedback gain and may make the feedback loop unstable. With the mechanical resonances an additional phase shift of $-180°$ is introduced (4). Thus, to satisfy bode's stability criteria, the integral gain K_I has to be chosen small enough, such that the magnitude of the open loop transfer function is less than one at the eigenfrequency of each mechanical resonance. At the same time, it is desirable to obtain a magnitude of the open loop transfer function as large as possible for frequencies lower than the cavity half bandwidth $\omega_{1/2}$. For the values of Q_L and E_{acc} foreseen in the EuXFEL CW upgrade and using the mechanical values of TESLA cavities listed in Czarski et al. (2006) a good compromise is to set the unit gain on the feedback at values that are approximately one order of magnitude less than the lowest value mechanical eigenfrequency. For $\frac{\omega_{1/2} g K_I}{2\pi} = 10.8 \, \text{Hz}$ ($g K_I = 0.5$ for $Q_L = 3 \cdot 10^7$) the maximum magnitude in the open loop transfer function of about $-18 \, \text{dB}$ for $y_0 = 0$ at frequencies above $200 \, \text{Hz}$ (Fig. 2). Such significant gain margin is required to address the uncertainties in the mechanical modes quality factors, couplings, and cavity detuning. At the same time, the closed-loop transfer function shown in Fig. 3 is attenuated by more than $-22 \, \text{dB}$ at $1 \, \text{Hz}$.

3.1 Considerations over the nonlinear model

All the derivations on the controller stability presented so far use a linearized model of the cavity. A proof of stability on the linearized model is a necessary but not sufficient condition for the stability of the nonlinear

model represented by (1) and (4). Furthermore, it has to be tested if the controller can bring the cavity back to a determined setpoint starting from an arbitrary initial detuning value. To do this, the cavity system has to be simulated under the effect of the integral controller. Before, a steady-state analysis is performed, where the time-scale of the controller is assumed to be small compared to the RF timescale of the system. To do this the controller action timescale is supposed to be slow compared to the RF timescale of the system. Such an assumption holds because $|g K_I| < 1$ was chosen. Therefore it is possible to approximate the instantaneous values of cavity status to the steady-state case described by (7) and represented by Fig. 1. Because of this the action of the piezoelectric tuner can be supposed to directly change the zero gradient detuning. Such a study, represented in Fig. 4, shows that the cavity system always returns to the setpoint, independently of the initial detuning condition. If the system starts from the low gradient side of the monotonic instability, first the controller brings it to the high gradient side pushing it through the inverse static drop and then tunes it to the setpoint. In the graphical study, it turns out that the controller brings the cavity back to the phase setpoint independently of the initial detuning even when the system experiences a static drop. A numerical closed-loop simulation of the nonlinear cavity model confirms the behavior derived by the steady-state evaluation and shows that the system converges to the setpoint.

4. EXPERIMENTAL RESULTS

The ability of the designed controller to prevent static drops is verified experimentally on TESLA-type super-
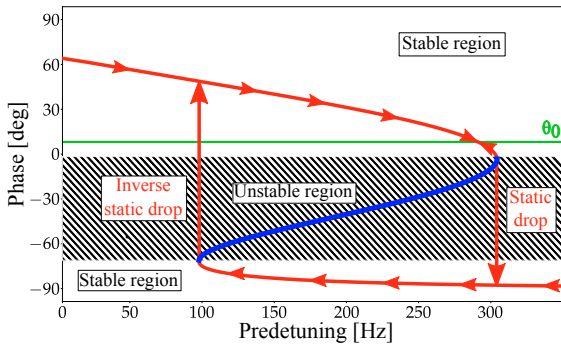
Fig. 4. Trajectory of the cavity phase using the feedback controller. The arrows denote the direction of the trajectory. The red part of the curve constitutes the stable steady-state solutions of (7).
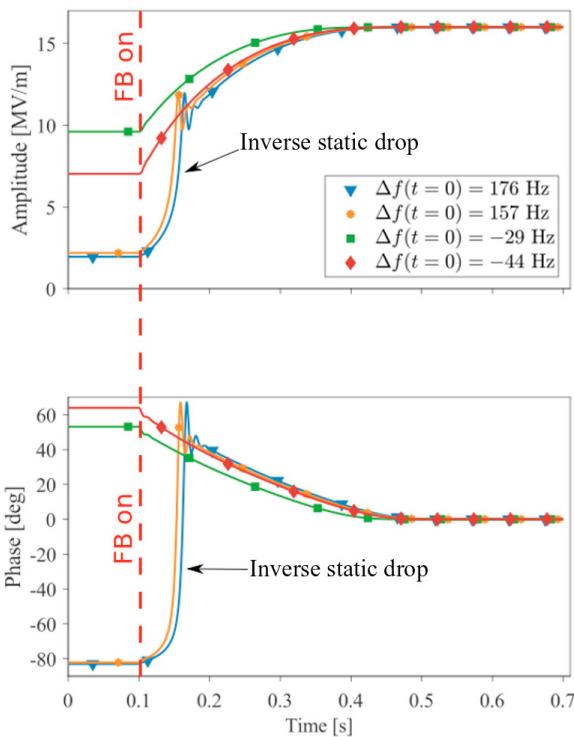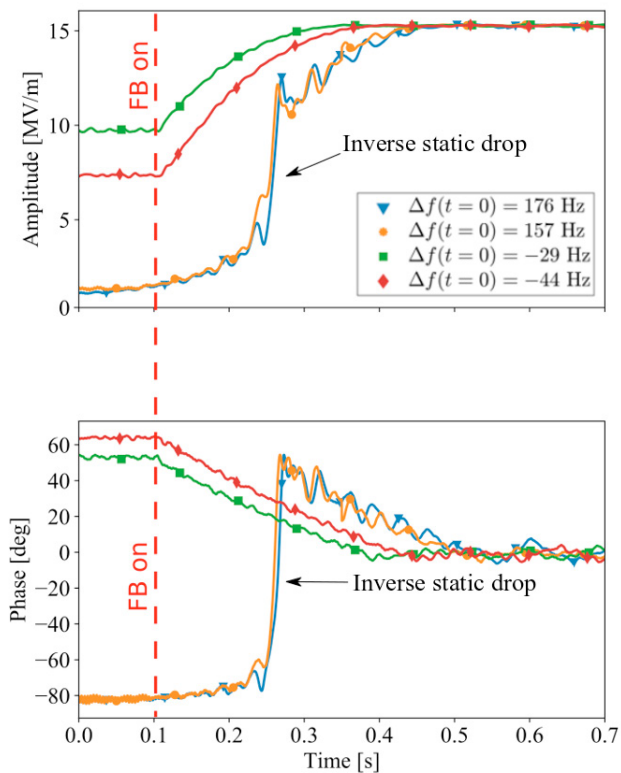

Fig. 5. Simulated closed-loop response of the cavity amplitude and phase with $V_g/L = 16\,\mathrm{MV\,m^{-1}}$ and $Q_L = 3 \times 10^7$. The complete nonlinear model, constituted by (1) and (4) with mechanical data from Czarski et al. (2006), was used.

conducting cavities. All tests were performed at the Cryo Module Test Bench (CMTB) using a EuXFEL-like cryomodule prototype, XM50.1 (Branlard et al. (2019)) First, the stability of the static detuning is evaluated (Fig. 6). It turned out that every 45 s some event triggers a decrease of the detuning of 4 Hz. This effect originates probably from a subsystem that is used to regulate the helium bath or cavity vacuum. Even though investigations are on-going to determine the cause of such repetitive detuning event, a way to maintain the cavity frequency at a fixed value is helpful to avoid static drops. Then a simultaneous drive of eight cavities in resonance was achieved. An additional Active Noise Controller (ANC) (Rybaniec et al. (2017)) was
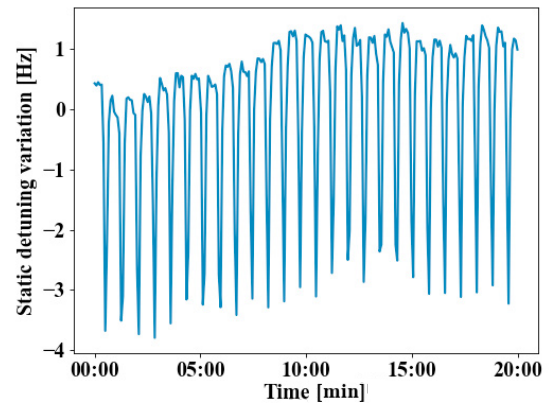
Fig. 6. Measured stability of the static detuning over twenty minutes. A periodic 4 Hz detuning effect is present. The measurement was performed in open loop at $V_g/L = 4\,\mathrm{MV\,m^{-1}}$

used to compensate for repetitive noise with frequencies higher than 1 Hz. The objective was to evaluate how much the monotonic instability impacts the cavity operations at the target gradients of EuXFEL upgrade. All tests were done at $Q_L = 3 \cdot 10^7$ For gradient values of higher than $10\,\mathrm{MV\,m^{-1}}$ it was hard to achieve good stability or even to reach the cavity resonance without incurring a static drop after some minutes of operation. The severity of the instability effects increased at higher gradients. At gradients around $16\,\mathrm{MV\,m^{-1}}$, the interlock system made the operation of the module impossible due to the large gradient variations correlated to static drops. Successive tests, done with the fast tuner feedback switched on, showed substantial improvement compared to the previous attempts to raise the field inside the cavities to the resonance condition. The controller used in these tests is a CW adaptation of the current EuXFEL LLRF controller, which includes a Proportional-Integral (PI) feedback on the fast tuners. During the tests, only the integral part of the PI controller was used. The unit gain was set to 10.8 Hz as in the simulations. Then, switching on the feedback controller, it was possible to achieve a stable resonance condition on all the cavities inside the module at the same time for gradients up to $16\,\mathrm{MV\,m^{-1}}$. Past studies (Branlard et al. (2018)) confirm the effectiveness of the discussed feedback controller at even higher values of Q_L and E_{acc}. The ability of the controller to bring back the cavity to the desired tune with an arbitrary large initial detuning was also confirmed (Fig. 7). When the system starts from the overtuned case ($\Delta f > 0$, $\theta < 0$), there is an initial delay of about 100 ms which was not seen in the simulations. The reason for this delay could be explained by the presence of backlash in the piezo actuator. Such an effect did not affect the final performance of the feedback controller in keeping the cavity resonance at the desired value.

5. CONCLUSION

In this article, the monotonic instability is studied to see how it would impact the operations of high Q_L SRF cavities driven in CW mode of operation. It is found that such instability would prevent to operate the cavities in stable conditions at high gradients ($> 10\,\mathrm{MV\,m^{-1}}$) because

Fig. 7. Experimental closed-loop response of the cavity amplitude and phase with $V_g/L = 16\,\mathrm{MV\,m^{-1}}$ and $Q_L = 3 \times 10^7$. The controller is able to bring the cavity to resonance for either for positive or negative initial value of the detuning.

of the proximity of the RF resonance to the monotonic drop threshold. Therefore, the behaviour of an integral control law of the piezo tuners to mitigate this issue was studied and tested. The analytical explanation why a pure integrating feedback controller on the fast piezo-electric tuner of the cavities is an effective way to prevent monotonic drops was derived theoretically, demonstrated by simulations and verified experimentally. Eight cavities were driven at previously unstable conditions ($E_{\mathrm{acc}} = 13\,\mathrm{MV\,m^{-1}}$, $Q_L = 3 \times 10^7$) thanks to the use of the controller. An added benefit of using the controller derived in this work is the ability to tune the cavities the resonance without the manual intervention of an operator. Some questions remain about the impact of the nonidealities of the piezo actuator (backlash, nonlinearity) and the possible limitations of of the proposed solution. Another aspect to be studied is how drifts in the RF detection chain affect the operations because the fast tuner feedback controller uses the detected RF phase of the cavity signals. Due to changes in humidity and temperature, a variation in the delay of the signals could induce the feedback controller to trip the cavity operating point over the static drop threshold. Finally, the effects that the beam induces on the accelerating field were neglected. Therefore, it has to be studied if more refined detuning estimation techniques are needed rather than relying only on the cavity RF phase to correct the effects produced by LFD. Nevertheless, the electro-mechanical cavity model derived in this paper, and the approach used to correct the monotonic instability can

be used as a starting point for further development of the fast tuner feedback controller.

REFERENCES

Branlard, J. et al. (2018). Highlights of the XM-3 cryomodule tests at DESY. In *Proceedings of LINAC2018*, 388–390. JACOW Publishing, Geneva, Switzerland.

Branlard, J. et al. (2019). Status of cryomodule testing at CMTB for CW R&D. In *Proceedings of SRF 2019*.

Czarski, T., Pozniak, K.T., Romaniuk, R.S., and Simrock, S. (2006). TESLA cavity modeling and digital implementation in FPGA technology for control system development. *Nuclear Instruments and Methods in Physics Research Section A: Accelerators, Spectrometers, Detectors and Associated Equipment*, 556(2), 565–576.

Habs, D. and Köster, U. (2011). Production of medical radioisotopes with high specific activity in photonuclear reactions with γ-beams of high intensity and large brilliance. *Applied Physics B*, 103(2), 501–519.

Liepe, M.U. (2001). Superconducting multicell cavities for linear colliders. Technical report, DESY.

Nakamura, N. et al. (2015). Design Work of the ERL-FEL as the High Intense EUV Light Source. In *Proceedings of ERL 2015*, MOPCTH010.

Padamsee, H., Knobloch, J., Hays, T., et al. (2008). *RF superconductivity for accelerators*, volume 2011. Wiley Online Library.

Raubenheimer, T.O. (2018). The LCLS-II-HE, a high energy upgrade of the LCLS-II. In *Proceedings of FLS2018*, 6–11. JACOW Publishing, Geneva, Switzerland.

Rybaniec, R. et al. (2017). FPGA-based rf and piezocontrollers for SRF cavities in CW mode. *IEEE Transactions on Nuclear Science*, 64(6), 1382–1388.

Schilcher, T. (1998). *Vector sum control of pulsed accelerating fields in Lorentz force detuned superconducting cavities*. Ph.D. thesis.

Schulze, D. (1972). *Ponderomotive stability of RF resonators and resonator control systems*. Ph.D. thesis, Universitt Karlsruhe.

Sekutowicz, J. et al. (2015). Research and development towards duty factor upgrade of the European X-Ray Free Electron Laser linac. *Physical Review Special Topics-Accelerators and Beams*, 18(5).

Serafini, L. et al. (2019). Marix, an advanced mhz-class repetition rate x-ray source for linear regime time-resolved spectroscopy and photon scattering. *Nuclear Instruments and Methods in Physics Research Section A: Accelerators, Spectrometers, Detectors and Associated Equipment*, 930, 167–172.

Slater, J.C. (1946). Microwave electronics. *Reviews of Modern Physics*, 18, 441–512.

Zhu, Z. et al. (2017). SCLF: An 8 GeV cw scrf linac-based x-ray fel facility in shanghai. In *Proceedings of FEL2017*, 20–25. JACOW Publishing, Geneva, Switzerland.

5.4 Oscillatory instability

Another instability present in superconducting high Q_L cavities driven in CW is the oscillatory instability. Such instability is triggered when the cavity is negatively detuned and an accelerating gradient threshold is surpassed. When the instability is present, the stored RF energy gets converted to mechanical energy, and the accelerating gradient and detuning start to oscillate with increasing amplitude. The amplitude growth of the oscillations is limited by nonlinear effects (Fig. 5.5). The oscillatory instability is detrimental to the RF accelerating field stability [96].

To study the occurrence of the oscillatory instability, (5.9) is linearized around the steady state as in equation 14 of [20]. The stability of the system can be derived from the system matrix of the linearized cavity model

$$\mathbf{A} = \begin{bmatrix} \mathbf{A_e} & \mathbf{H} & \mathbf{H} & \dots & \mathbf{H} \\ \widehat{\mathbf{G}}^{(1)} & \mathbf{A_m^{(1)}} & \mathbf{0} & \dots & \mathbf{0} \\ \widehat{\mathbf{G}}^{(2)} & \mathbf{0} & \mathbf{A_m^{(2)}} & \ddots & \vdots \\ \vdots & \vdots & \ddots & \ddots & \mathbf{0} \\ \widehat{\mathbf{G}}^{(N)} & \mathbf{0} & \dots & \mathbf{0} & \mathbf{A_m^{(N)}} \end{bmatrix}, \tag{5.22}$$

with

$$\mathbf{A_e} = \omega_{1/2} \begin{bmatrix} -1 & y_0 \\ -y_0 & -1 \end{bmatrix}, \tag{5.23}$$

$$\mathbf{H} = \omega_{1/2} \begin{bmatrix} 0 & 0 \\ -1 & 0 \end{bmatrix}, \tag{5.24}$$

$$\widehat{\mathbf{G}}^{(\mu)} = \frac{2(\omega^{(\mu)})^2 K_{\mathrm{lfd}}^{(\mu)} V_g^2}{1 + y_0^2} \begin{bmatrix} 0 & 0 \\ 1 & 0 \end{bmatrix}, \tag{5.25}$$

$$\mathbf{A_m^{(\mu)}} = \begin{bmatrix} 0 & 1 \\ -(\omega^{(\mu)})^2 & -\frac{\omega^{(\mu)}}{Q^{(\mu)}} \end{bmatrix}. \tag{5.26}$$
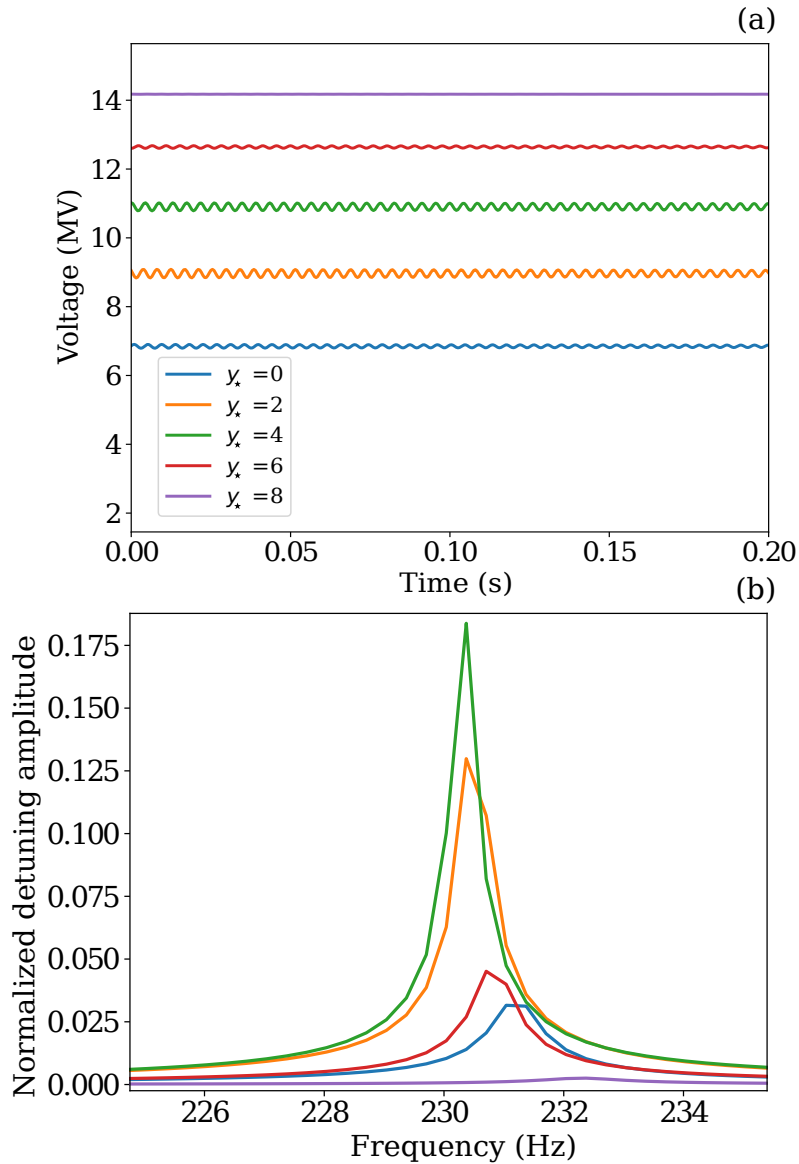
Figure (5.5)   Simulation of oscillatory instability effects on accelerating voltage (a) at different values of $y_\star$. $Q_L = 3 \cdot 10^7$ and the mechanical parameters are taken from [97]. At $y_\star = 8$, the system is near resonance and the oscillatory instability is not present. For lower values of $y_\star$, the cavity is negatively detuned thus triggering the oscillatory instability. The effect of the instability on the detuning FFT is also shown around the frequency of the lowest mechanical resonance (b).
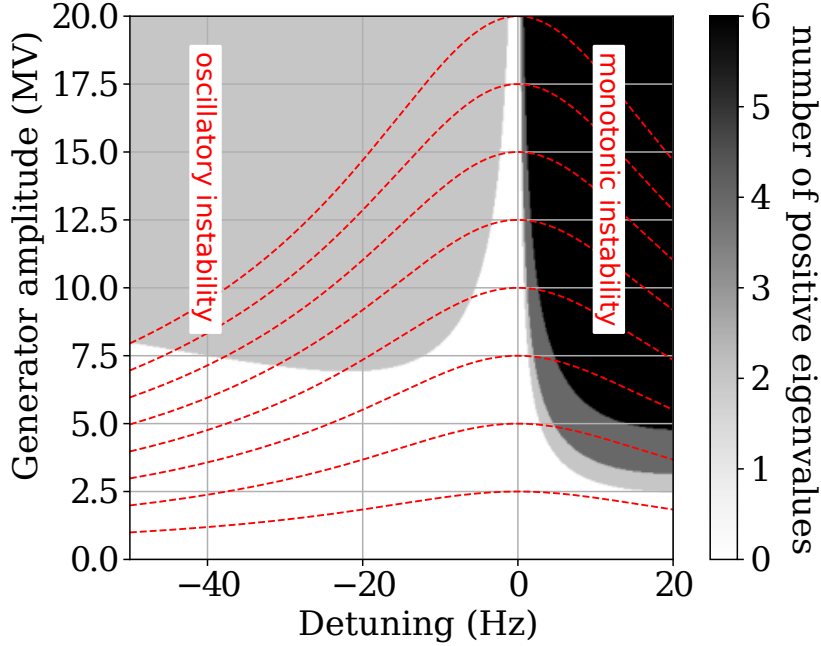
Figure (5.6)   Ponderomotive stability map for different cavity accelerating voltages and detuning values. $Q_L = 3 \cdot 10^7$. The dashed lines represents cavity resonance curves.

$f^{(\mu)}$ (Hz)	$Q^{(\mu)}$	$k^{(\mu)}$ (Hz/(MV/m)^2)
235	100	0.4
290	100	0.3
450	100	0.2

Table (5.1)   Mechanical parameters for Fig. 5.6 [97]

y_0 is the normalized detuning around which the small-signal derivation is performed. To achieve stability, all the eigenvalues of (5.22) must have a negative real part. Such a study can be done numerically by counting the unstable modes of (5.22). In Fig. 5.6 is shown the stability map of a superconducting TESLA cavity driven in CW for $Q_L = 3 \cdot 10^7$.

The mechanical parameters that were used for Fig. 5.6 are listed in Tab. 5.1.

At $E_{acc} = 15\,\mathrm{MV\,m^{-1}}$, a cavity detuning of less than $-2.5\,\mathrm{Hz}$ is enough to trigger the oscillatory instability, which is equal to $y = -0.12$. Since some tuning margin is required to not incur into the monotonic instability, driving the

system in unstable oscillatory conditions might be necessary. The control of oscillatory instability in generator-driven high Q_L cavity systems is still an open issue. The main problems are the difficulty to realize a controller for complex cavity mechanical transfer functions and the difference in cavity dynamics at different working points due to nonlinearities. Different approaches to overcome the oscillatory instability in TESLA cavities are currently under study [98, 99]. At CMTB, oscillatory instabilities have prevented in the past long term stable operations at $E_{acc} > 15\,\mathrm{MV\,m^{-1}}$. Future studies will determine the necessity of using new resonance control algorithms to prevent the growth of oscillatory instability disturbances for the EuXFEL CW/LP upgrade.

Chapter 6

Linearization of High-Power RF amplifiers

6.1   RF power sources for EuXFEL

For the EuXFEL upgrade, new RF power sources will be required to operate
the accelerator in CW and LP mode. The power requirements can be evaluated
using (3.3). For LP mode of operation at $14\,\mathrm{GeV}$ (Tab. 3.1) the L3 cavities will
be driven at $15\,\mathrm{MV\,m^{-1}}$ (Tab. 3.8). Therefore, considering a $Q_L = 10^7$ for L3, at
least $5.8\,\mathrm{kW}$ has to be provided to the cavities. Moreover, to achieve the required
accelerating field stability, the amplifiers have to provide a low noise RF output.
Finally, cost and size constraints have to be taken into account. The existing VS
RF distribution system (Fig. 6.1) makes it difficult to realize individual cavity
control, so multiple cavities have to be driven by a single amplifier. For L-band
and S-band cavities, three kinds of amplifiers are commonly used: Solid State
Amplifiers (SSA), IOTs, and klystrons.

SSA   Due to the rapid development of solid-state electronics, SSAs usage in
accelerators saw an increase in recent years. As notable examples, future hard
X-ray FEL projects such as LCLS-II [102] and SHINE [17] plan to use SSAs as
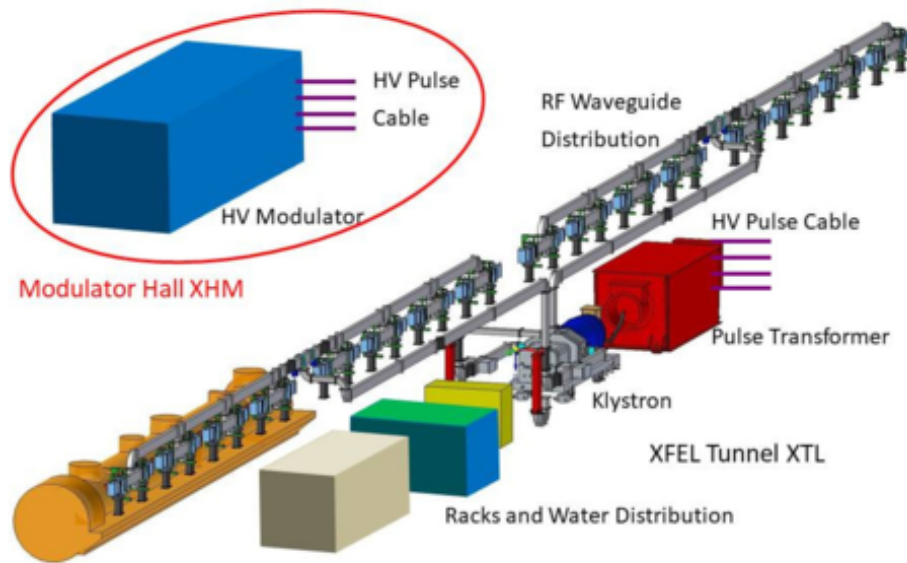
Figure (6.1)   Current pulsed-mode EuXFEL RF power system [100]. A single klystron provides the power to 32 superconducting accelerating cavities in vector-sum.

Figure (6.2)   A 10 kW rack-mounted L-band SSA amplifier [101]. The rack consists of eight separate 1.25 kW modules.

power sources. SSAs provide high efficiency, low noise, and, unlike vacuum tube-based amplifiers, low drive voltage and excellent linearity compared to IOTs and klystrons [103]. Moreover, SSAs are available as rack modules(Fig. 6.2). A single rack can provide tens of kilowatts of RF power and allows easy maintenance and repair operations. Even with these key advantages, SSAs are not considered the main choice for the EuXFEL CW upgrade because, at the required power levels per cavity, this kind of amplifier is not compact enough to fit in the accelerator tunnel. However, since the CW third-harmonic module will require at maximum $1\,\mathrm{kW}$ of RF power per cavity (Fig. 3.11) and will not require a VS power distribution, the use of S-band SSAs is under evaluation.
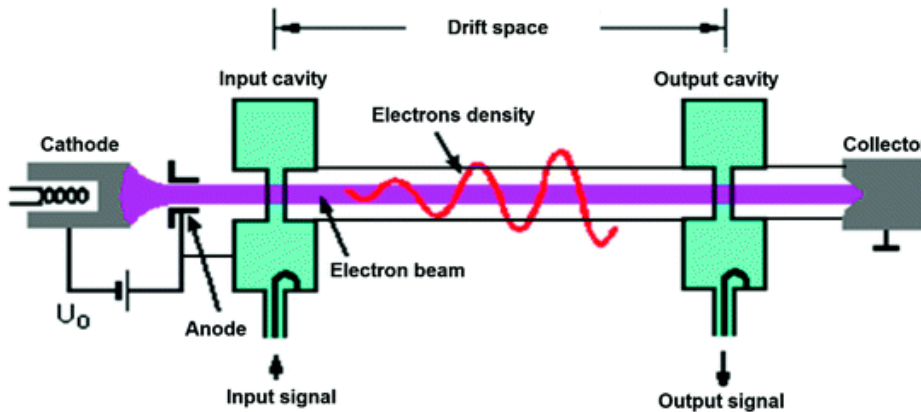
Figure (6.3)   Two cavity klystron scheme [104].

Klystron   The klystron is a tube-based RF amplifier. Its simplest form consists of a cathode, a *buncher* cavity in the proximity of the cathode, and a *catcher* cavity in the proximity of the anode. A drifting space connects the two cavities. The cathode produces a continuous beam of electrons due to a voltage between the cathode itself and the anode. When an RF signal is applied to the buncher cavity, the electron beam is modulated in velocity. Such velocity modulation results in the formation of a density modulation in the drift space. Finally, the catcher cavity collects the RF power of the modulated beam. The beam energy that is not absorbed by the catcher cavity is dissipated on the klystron anode. Therefore the anode has to sustain the full power of the beam when no current modulation is present. Fig. 6.3 shows a scheme of a two-cavity klystron. The klystron power

output is ideally described by [104]

$$P_{out} \propto J_1(\alpha V_{mod})^2, \tag{6.1}$$

with P_{out} the output RF power, J_1 the first-order Bessel function of the first kind, V_{mod} the modulating voltage in the launcher cavity, and α a proportionality constant.

Manufacturer	Canon
Model	E37750
Frequency (GHz)	1.3
Output power (kW)	300
Maximum efficiency (%)	63
Gain (dB)	40
Beam voltage (kV)	49
Length (m)	1.8

Table (6.1)   Specifications for a recent L-band CW klystron for particle accelerator applications [105]

Manufacturer	Toshiba
Model	E3736
Frequency (GHz)	1.3
Output power (MW)	10
Maximum efficiency (%)	65
Saturation gain (dB)	47
Beam voltage (kV)	49
Length (m)	2.27

Table (6.2)   Specifications for high peak power multi beam klystron for particle accelerator applications [106]

Current state-of-the-art L-band klystrons for particle accelerators can have a power output from several hundreds of kilowatts (Tab. 6.1) in CW to several megawatts for pulsed Multi-Beam Klystrons (MBK) with duty cycles of $\approx 1\%$ (Tab. 6.2). Currently, CW klystrons are not the primary choice for the EuXFEL CW upgrade due to their size and efficiency compared to IOTs. Moreover, in the LP mode of operation, the klystron beam power is totally lost when there is no particle acceleration, while the use of a high-voltage pulse modulator will impact space occupancy. Nevertheless, the actual MBK klystron installed at EuXFEL will be kept to maintain the ability to operate in SP.
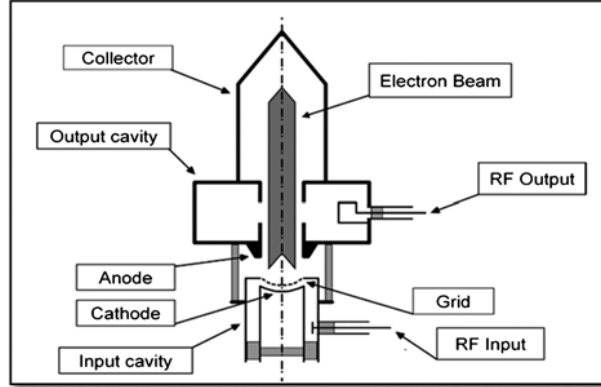
Figure (6.4)   IOT scheme [107].

IOT   The IOT is a tube-based RF amplifier. As for the klystron, a catcher cavity is present. However, unlike the klystron, the current modulation is achieved with a control grid. This grid is positioned in front of the cathode, and it is connected to the IOT input port (Fig. 6.4). An advantage of such a method of achieving beam modulation is a much shorter drift space than klystrons, which reduces the amplifier overall size. Moreover, contrary to the klystron, the generated beam current depends on the grid voltage, resulting in an increased efficiency when the IOT is operated far from its maximum power output limit. When no RF power is required, the IOT beam current is ideally zero. This characteristic is particularly appealing for the LP mode of operation. Due to their efficiency, IOTs need smaller collectors compared to klystrons with similar power ratings, thus increasing their compactness even further. The output power of an ideal IOT far from the saturation limit follows the *Child-Langmuir law* [108, 109]

$$P_{out} \propto (V_g + V_a/\mu)^3, \tag{6.2}$$

with V_g and V_a the grid and anode voltage in respect to the cathode and μ a constant that depends on the geometry. The IOT is usually operated as class-B amplifier in particle accelerators, so V_g is biased to cancel the V_a/μ term in 6.2.

IOTs with an output power of hundreds of kilowatts are commercially available (Tab. 6.3). IOTs are considered the primary CW RF-amplifier source candidate for the EuXFEL CW upgrade due to their characteristics.

Manufacturer	CPI
Frequency (GHz)	1.3
Output power (kW)	120
Maximum efficiency (%)	> 60
Gain (dB)	22
Beam voltage (kV)	49
Length (m)	1.0

Table (6.3)   Specifications for an IOT for particle accelerator applications [50]

6.2   Results on FPGA-Based High-Power TubeAmplifier Linearization at DESY
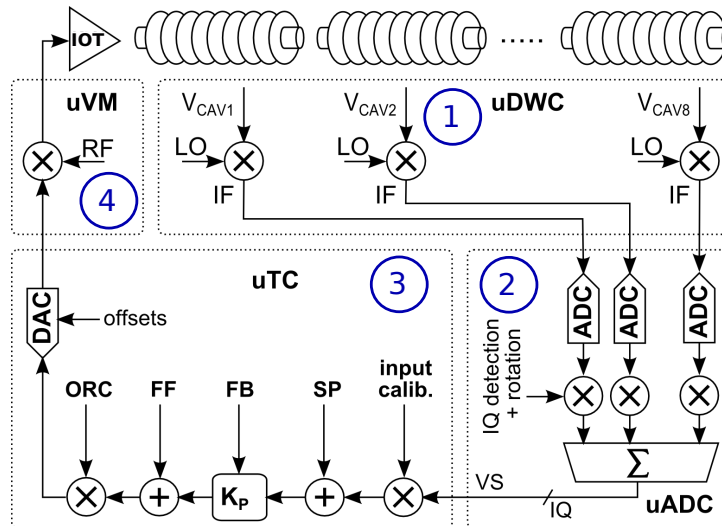
Figure (6.5)   Depiction of an RF closed-loop scheme for vector-sum control [69]. (1) The individual cavity probe signals are down-converted to a lower frequency. (2) The signals are digitalized and in an I&Q representation and summed together. (3) The control value is calculated with respect to a setpoint and converted to an analog signal. (4) The analog control signal is up-converted to 1.3 GHz before being sent to the high power amplifier that drives the cavities.

To achieve the required cavity field stability of 0.01% and 0.01° in amplitude and phase, EuXFEL has to operate in closed-loop [41] (Fig. 6.5). Therefore the high power chain, which represents the controller actuator, directly affects the accelerator operation.

Klystrons and IOTs show significant nonlinearities in their output amplitudes, as can be derived taking the square root of (6.1) and (6.2). Therefore the gain
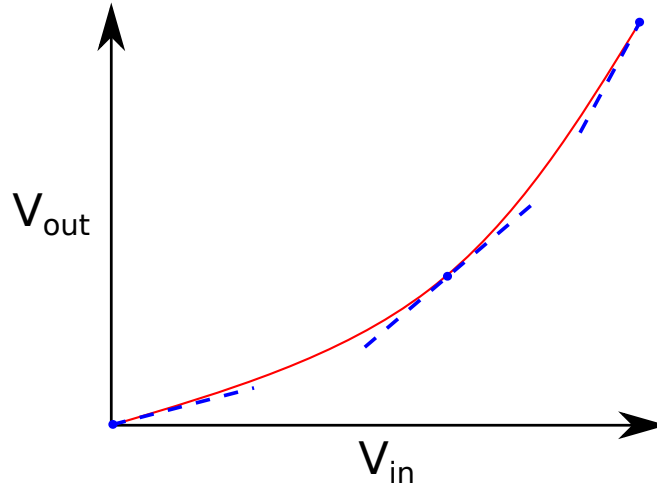
Figure (6.6)   Example of a nonlinear input-to-output amplifier characteristics (red curve). The differential gain $\frac{dV_{out}}{dV_{in}}$ (blue lines) depends on the working point.

is dependent on the controller working point (Fig. 6.6). An amplitude-dependent phase rotation of the output signal is also present. These effects limit the maximum achievable loop gain and might impact the overall system stability. Additionally, the presence of nonlinearities complicates the system setup procedures. The FF and LFF partially reduce the impact of amplifier nonlinearities by making the feedback controller operate in the proximity of the desired working point. However, the use of a feedforward correction does not solve the issue of having an amplitude-dependent amplifier gain. Therefore different types of correction techniques were developed in the years, mainly for telecommunication purposes [110]. Here the performance of a predistortion-based component used with klystrons and IOT is reported. The tests were conducted with the RF amplifiers of CMTB, EuXFEL, and FLASH.

Results on FPGA-Based High-Power Tube Amplifier Linearization at DESY

Andrea Bellandi[ID], Valeri Ayvazyan, Łukasz Butkowski[ID], Wojciech Cichalewski, Burak Dursun[ID], Çağıl Gümüş, Mathieu Omet, Sven Pfeiffer[ID], Rüdiger Onken, Radoslaw Rybaniec[ID], Christian Schmidt, Vladimir Vogel, and Julien Branlard

Abstract— **Vacuum-tube amplifiers are the most widespread type of radio frequency (RF) sources used to produce high-power signals needed for beam acceleration in superconducting cavities. At Deutsches Elektronen-Synchrotron (DESY), megawatt-rated klystrons are used to produce millisecond-long RF shots for pulsed operation in particle accelerators. In contrast, inductive output tubes (IOTs) are used to provide a continuous RF signal for continuous-wave (CW) operation. In both cases, the amplifiers suffer from amplitude-dependent nonlinearity between the driving and generated signals. This nonlinearity complicates the setup operations of the low-level RF (LLRF) system and makes it harder to regulate the accelerating field. Therefore, a way to linearize the amplifier is highly valuable. This article covers the design, implementation, and test of a field-programmable gate array (FPGA)-based predistortion linearization unit. The first results on the performance of this component in linearizing the amplifiers of running CW and pulsed superconducting accelerators are presented. Such a component uses programmable interpolating lookup tables (LUT) that are addressed using the squared value of the requested signal amplitude. This component only adds 64-ns latency to the RF control system without relying on any vendor-dependent FPGA component. Other benefits of using programmable interpolating LUT are low usage of FPGA resources and flexibility in terms of the type of amplifier to be corrected. The benefits of using this linearizer for klystrons and IOTs are presented and quantified.**

Index Terms— **Inductive output tube (IOT), klystron, low-level radio frequency (LLRF), particle accelerators.**

I. INTRODUCTION

HIGH-POWER radio frequency (RF) amplifiers are an essential component in many modern particle accelerators as they provide the energy for beam acceleration [1]. A scheme of an RF drive chain for particle accelerators is shown in Fig. 1; here, a field-programmable gate array (FPGA)-based digital low-level RF (LLRF) controller [2] produces a drive signal through a digitally controlled vector
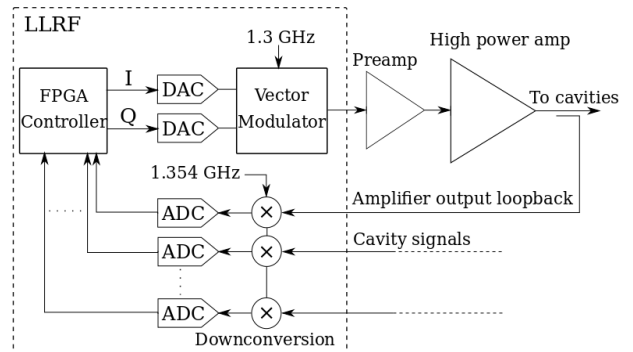
Fig. 1. Scheme of an RF drive chain for particle accelerators. The modulation frequency of 1.3 GHz is the design resonance frequency of the superconducting TESLA-type [7] cavity model. Such kind of cavity equips every superconducting linac at DESY.

modulator (VM). Then, after a preamplification stage, a high-power amplifier raises the RF signal to its final amplitude level and sends it to the accelerating cavities. At Deutsches Elektronen-Synchrotron (DESY), there are two main kinds of high-power amplifiers for linear superconducting accelerators. Klystrons are used for pulsed applications and tests at European X-ray free-electron laser (EuXFEL) [3], Free-electron-LASer in Hamburg (FLASH) [2], accelerator module test facility (AMTF) [4], and Cryo Module Test Bench (CMTB) [5]. Inductive output tubes (IOTs) or klystrodes are used for continuous-wave (CW) acceleration R&D at CMTB [6]. For these devices, the amplified RF signal is produced in an output cavity that extracts electromagnetic power from a bunched beam. The main difference between klystrons and IOTs is how the beam modulation is achieved. In klystrons, the input signal generates a standing wave in an input cavity. Such a field interacts with a dc electron beam, thus producing a velocity modulation of the particles. Then, the beam passes through a drift space where beam bunching is achieved. For this reason, klystrons reach a saturation point when the beam bunching reaches its maximum level. After the saturation of the beam bunching, the amplifier output power decreases with an increment in the input signal power. In IOTs, the modulation of the beam density is obtained through the use of an electrically controlled grid. In our case, the IOT is operated in a region where the gain increases as the input voltage increases. Another effect present in IOTs and klystrons is a phase rotation between the input and output signals. Such rotation depends on the driving amplitude. Fig. 2 shows a
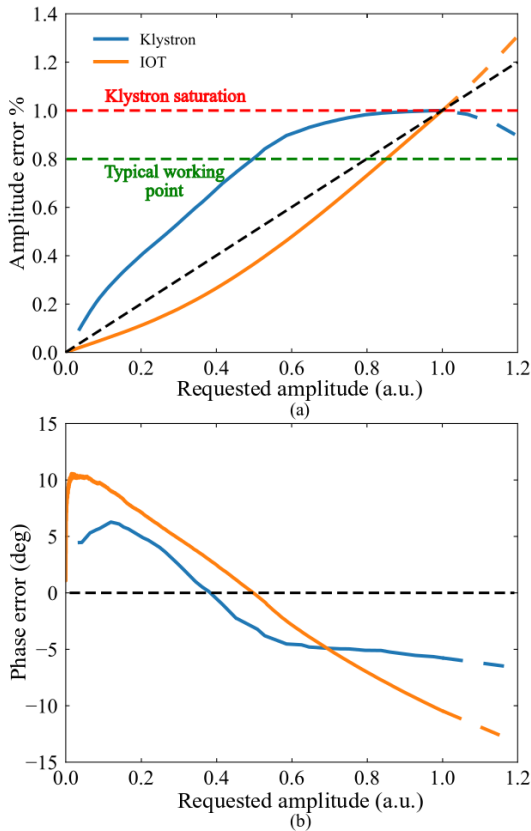
Fig. 2. Qualitative comparison between (a) input–output amplitude and (b) phase characteristics of a klystron and an IOT. The traces are normalized to one. The black dotted trace represents a perfectly linear behavior. The saturation of the IOT (not shown in the picture) happens at values much higher than the typical working point used in our facilities.

qualitative comparison between the input–output amplitude and phase characteristics of klystrons and IOTs. The nonlinearity and phase rotation of the amplifiers impacts the accelerator operations in the following ways.

1) It complicates the system setup procedures when a different power level is required. A linear change in the input signal does not correspond to an equal variation of the amplifier output.

2) The feedback algorithms of the LLRF controller must take into account that the gain of the amplifier changes as the input signal strength changes and adjust their model parameters accordingly.

3) At different amplitude levels, a counterrotation of the driving signal that matches the amplifier-generated phase shift has to be applied.

All the problems listed earlier worsen when a rapid transition between different power levels is required. Even though feedback [8] and learning control algorithms [9] mitigate these issues, a fast compensation of the amplifier distortions could still reduce the setup time and potentially improve the regulation characteristics. A method to correct the amplifier output is to predistort the driving signal implementing a dedicated component in the LLRF reconfigurable logic to obtain an overall linear RF chain [10]. In this article, we report the performances that we achieved on different kinds of klystrons and IOTs using this linearization method. Section II

introduces the working principle of the used predistorter algorithm. Section III shows a simulation of the predistorter correction capabilities. Section IV exposes how the algorithm is implemented in DESY LLRF controllers and the FPGA logic resources used. Finally, in Section V, the linearization performance of different kinds of RF tube amplifiers at CMTB, FLASH, and EuXFEL is reported.

II. ALGORITHM DESCRIPTION

The concept of using predistortion to correct for amplifier nonlinearities is extensively explained in [11] and [12], where a performance comparison between different algorithms is also made. The basic idea is to modify the amplifier input signal to compensate for the amplifier generated distortions. To achieve such an effect, the predistorter applies an amplitude-dependent complex multiplication to the original drive signal. In our implementation, we decided to use a lookup table (LUT)-based predistortion with the first-order interpolation between table entries to store the signal corrections. The advantages of using this kind of linearization are as follows.

1) Both amplitude and phase distortions of the RF chain can be corrected.

2) The programmable LUTs store the correction to be applied to the drive signal at a certain amplitude level. Therefore, the predistorter is not designed for a particular type of amplifier and can be used either with klystrons or IOTs, only updating the LUT.

3) It requires no additional hardware modification to our LLRF system.

4) It requires low FPGA resources in terms of digital signal processing (DSP) multipliers and block RAMs.

5) The interpolating LUT predistortion gives the best results in terms of quantization error and precision [12].

To avoid a square root computation, we decided to use the squared amplitude to generate the index of the LUT tables. Even if this choice results in an uneven distribution of the correction values with respect to the requested amplitude, it uses fewer FPGA resources and lowers the signal delay. To understand the effect of the predistorter component on the RF chain, the RF amplifier is modeled as

$$|y| = f_A(|x_{\mathrm{VM}}|)$$
$$\Delta\theta_y = f_\theta(|x_{\mathrm{VM}}|) \tag{1}$$

where x_{VM} is the VM output signal, y is the RF amplifier output signal, and $\Delta\theta_y$ is the phase shift between x_{VM} and y. f_A and f_θ can be measured by varying the VM output amplitude and recording the generated signal at the end of the chain. $f_A(|x_{\mathrm{VM}}|)$ is assumed to be invertible in the range where the amplifier is operated. The predistorter model is

$$|x_{\mathrm{VM}}| = P_G(|x_R|^2)|x_R|$$
$$\Delta\theta_S = P_\theta(|x_R|^2) \tag{2}$$

where x_R is the requested amplitude and $\Delta\theta_S$ is the predistorter-produced phase shift between x_R and x_{VM}. $P_G(|x_R|)$ and $P_\theta(|x_R|)$ represent the amplitude gain and phase shift produced by the predistorter. Using the above equations,
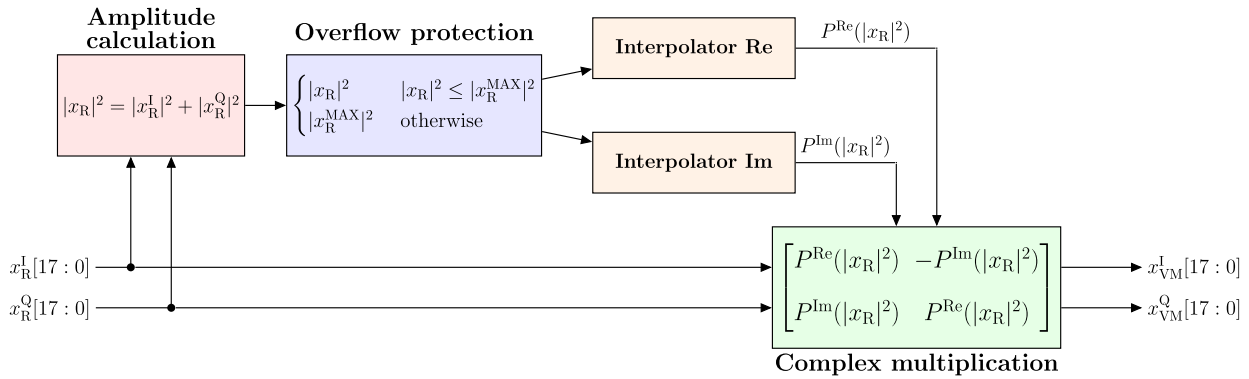
Fig. 3.   Functional scheme of the linearizer. $x_R^{I/Q}$ and $x_{VM}^{I/Q}$ are the requested and predistorted I&Q signals, $|x_R^{MAX}|$ is the maximum amplitude managed by the component, and $P^{Re/Im}$ is the complex rotation components.

the RF chain is linear when P_G and P_θ are set to obtain an amplifier output proportional to $|x_R|$ with a constant phase shift. These conditions are equal to impose

$$G_C \cdot |x_R| = f_A(P_G(|x_R|^2) \cdot |x_R|)$$
$$\Delta\theta_C = f_\theta(P_G(|x_R|^2) \cdot |x_R|) + P_\theta(|x_R|^2) \qquad (3)$$

with G_C and $\Delta\theta_C$ being the desired gain and constant phase shift of the RF chain. Solving (3) for P_G and P_θ gives

$$P_G(|x_R|^2) = \frac{f_A^{-1}(G_C|x_R|)}{|x_R|}$$
$$P_\theta(|x_R|^2) = \Delta\theta_C - f_\theta\big(f_A^{-1}(G_C|x_R|)\big). \qquad (4)$$

$P_G(|x_R|)$ and $P_\theta(|x_R|)$ can be then used to find the compensation values as real and imaginary components

$$P^{Re}(|x_R|^2) = P_G(|x_R|^2) \cos\left(P_\theta(|x_R|^2)\right)$$
$$P^{Im}(|x_R|^2) = P_G(|x_R|^2) \sin\left(P_\theta(|x_R|^2)\right). \qquad (5)$$

Finally, the values of the LUT tables can be found by taking into account that the index of the table elements is i and is proportional to the squared value of the requested amplitude

$$|x|_i = |x_R^{MAX}|\sqrt{\frac{i}{N_{LUT}}} \quad \text{for } i = 0, 1, \ldots, N_{LUT} \qquad (6)$$

$$D_i^{Re/Im} = P^{Re/Im}(|x|_i^2) \qquad (7)$$

$$I_i^{Re/Im} = N_{LUT}\frac{P^{Re/Im}\big(|x|_{i+1}^2\big) - P^{Re/Im}\big(|x|_i^2\big)}{|x_R^{MAX}|^2} \qquad (8)$$

where $|x_R^{MAX}|$ is the maximum possible requested amplitude, N_{LUT} is the number of LUT values, and $D_i^{Re/Im}$ and $I_i^{Re/Im}$ are the values of the decimated and derivative LUTs at index i. The discretization of the requested amplitude in (6) results in a quadratic distribution of the correction tables along $|x_R|$. Because of this, the correction capability of the predistorter is maximal at values of $|x_R|$ near $|x_R^{MAX}|$. Fig. 3 shows the block diagram of the predistorter component.

III. SIMULATION OF THE ALGORITHM PERFORMANCES

To assess the performances of the predistorter component, a simulation of the predistorter capabilities was performed using the model derived in (4).
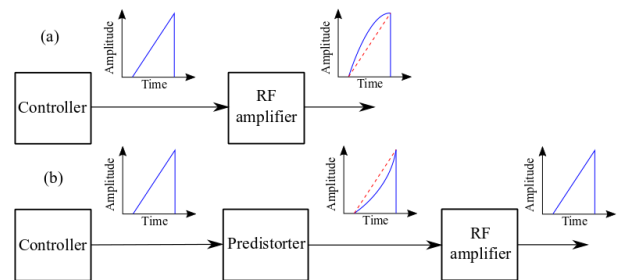
Fig. 4.   Block diagram of the RF chain (a) without and (b) with the predistortion active. In (a), a triangular pulse generates a distorted signal at the end of the amplifier chain. In (b), the same triangular pulse is predistorted before being sent to the amplifier to obtain an overall linear system.

The amplifier model data of (2) were recorded driving CMTB IOT with a one-second-long triangular pulse, as shown in Fig. 4(a). The peak amplifier output power during the characterization was set to be 35 kW. The trace was also averaged 256 times to reduce its noise. Using the data trace and (8) and (7), the LUT tables were computed. Even though the trace averaging resulted in smooth LUT values for $D_i^{Re/Im}$, due to the noise-enhancing properties of the derivative computation, additional filtering was required for $I_i^{Re/Im}$. Therefore, the zero-phase Savitzky–Golay [13] smoothing filter of order two was applied to the measured trace to remove the high-frequency part of the noise without distorting the original trace tendency. The filter implementation present in the *scipy* [14] software package was used. Fig. 5 shows a comparison between the derivative tables produced with and without the smoothing filter.

With the computed tables, a simulation of the predistorted chain, as shown in Fig. 4(b), was performed. Due to the quadratic distribution of the LUT values and the increased sensitivity of the phase to the noise at low amplitude levels in all the simulations and measurements performed, the first 10% of the requested amplitude range is not evaluated when computing the error. The simulation results show that the usage of the predistorter lowers the amplitude linearity mean absolute error (MAE) from 2.75% to $2.41 \cdot 10^{-3}$% and the phase MAE from 6.07° to $4.92 \cdot 10^{-3}$° (see Fig. 6). A simulation without using the interpolation was also performed. As can be seen in Table I, the amplitude linearity and phase MAE when the interpolation tables are not used increase by approximately
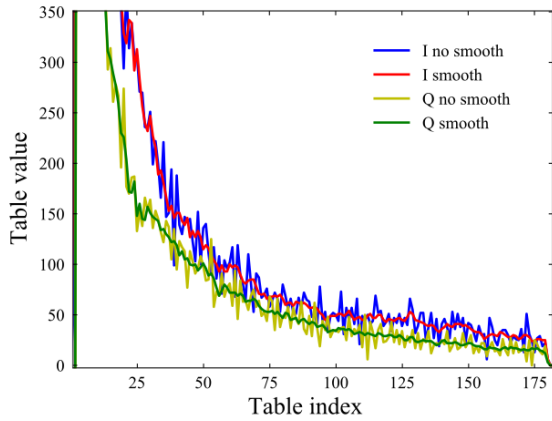
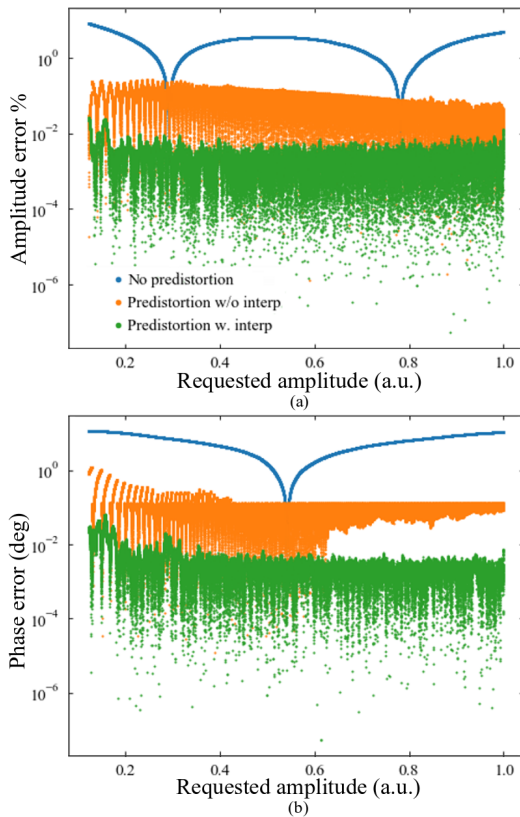Fig. 5. Effect of using a smoothing filter on the generation of the predistorter derivative tables.

Fig. 6. (a) Simulated absolute linearity and (b) phase error for the IOT.

TABLE I
SIMULATION RESULTS

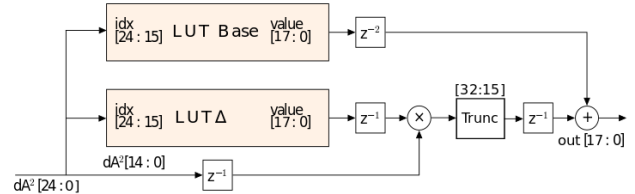|	Amplitude linearity MAE %	Phase MAE (deg)
No predistortion	2.75	6.07
Predistortion w/o derivative tables	$6.81 \cdot 10^{-2}$	$11.24 \cdot 10^{-2}$
Predistortion w. derivative tables	$2.41 \cdot 10^{-3}$	$4.92 \cdot 10^{-3}$

Fig. 7. Interpolator scheme. LUT base contains the downsampled version of the correction, whereas LUT Δ contains the derivative terms used to interpolate the output values between two indices. Note that a truncation on the lowest significance bits is performed after the multiplier to obtain an 18-bit value.

TABLE II
SYNTHESIS RESULTS

Toolchain	Vivado 2017.4	ISE 14.7
Target FPGA	Kintex 7	Virtex 6
Slice LUTs	203 / 260600	209 / 80000
Slice registers	275 / 521200	175 / 160000
BRAM tiles	4 / 835	4 / 264
DSP tiles	10 / 1680	8 / 480

an order of magnitude. Given that these simulation results represent an estimate of the maximum achievable linearization, the usefulness of the derivative tables depends on how well the measured amplifier transfer function represents the RF chain.

IV. IMPLEMENTATION

The LLRF controllers in operation at DESY in superconducting linacs use either the SIS8300L [15] or the DAMC-TCK7 [16] as the main control board. Systems based on SIS8300L are equipped with a Xilinx Virtex 6 FPGA and are intended to control a single resonator. Systems based on DAMC-TCK7 are equipped with a Xilinx Kintex 7 FPGA and can control multiple cavities at the same time using a vector sum (VS) scheme [4]. Because the Virtex 6 and Kintex 7 FPGA families are supported by different synthesis toolchains, namely, ISE 14.7 and Vivado 2017.4, care was taken to write the Hardware Description Language (HDL) code in a platform-independent fashion. In addition, no proprietary Intellectual Properties (IPs) were used in the realization of the algorithm. First, the 25-bit square amplitude of the I&Q signal is calculated, and its value is tested for overflow. Then, the upper 10 bits of this signal are used to address the correction values of two interpolators. Each interpolator is constituted by two 1024-entry LUTs with a word length of 18 bit. One LUT stores a decimated version of the correction values, while the other one stores their derivatives. The interpolated result is obtained summing the value contained in the first LUT with the second one multiplied by the lower 15 bits of the squared I&Q signal (see Fig. 7). Then, the correction values produced by the two interpolators are used to perform a complex multiplication with the original I&Q signal. Finally, the resulting values are sent to the VM for the analog conversion. The synthesized component adds a delay of eight clock cycles, which corresponds to an increase in the total delay between 8% and 13% depending on the used LLRF controller configuration. Table II lists the used resources over the total available ones.

In the tests, the default implementation strategy of each toolchain was used for synthesis. In the cases (Virtex 6 and Kintex 7), the predistorter used not more than 1% of the available resources, and it is capable of running at 125 MHz.
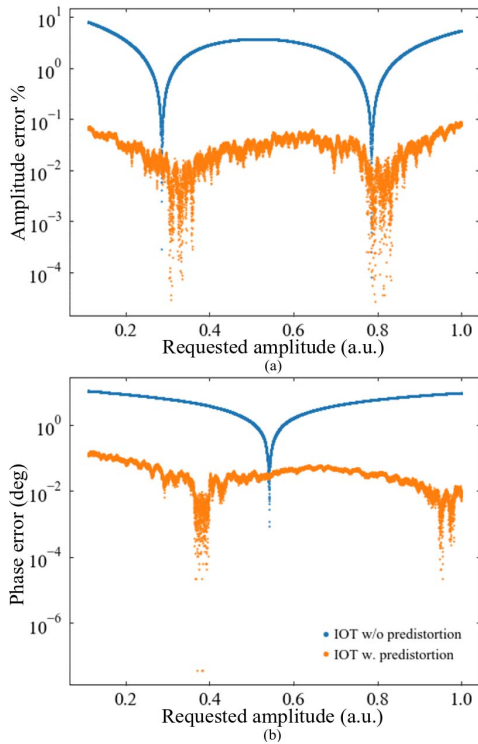
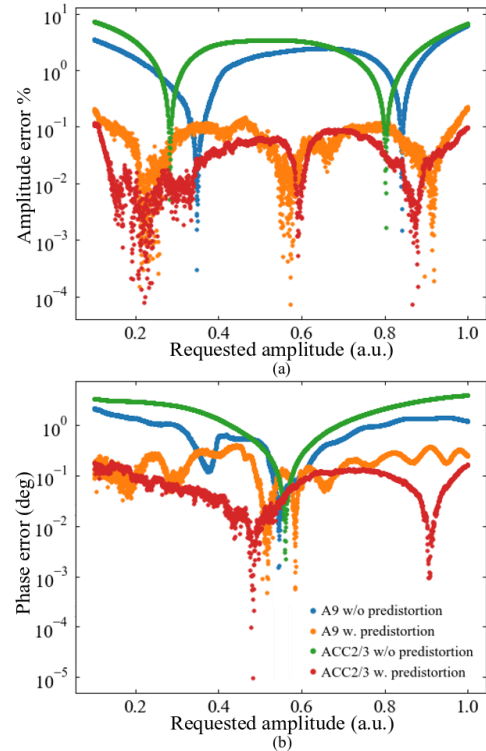Fig. 8. (a) IOT absolute linearity and (b) phase error in function of the requested amplitude.

Fig. 9. (a) XFEL A9 and FLASH ACC2/3 absolute linearity and (b) phase error in function of the requested amplitude.

V. EXPERIMENTAL TESTS

A. IOT

For IOT tests, Communication & Power Industries (CPI) 1.3-GHz 49-kV prototype amplifier installed at CMTB with a rated power of 120 kW was used. During the measurements, the peak power output was limited to 35 kW to avoid incurring thermal issues on the IOT itself. The produced power was dumped on a resistive load. The characterization was performed, as described in Section III. Here, again, the first 10% VM range was not used to estimate the final linearity and phase error. As can be seen in Fig. 8 and Table III, the predistorter component can improve the linearity of the IOT RF chain by a factor 94 and lower the phase error by a factor 96. The final amplitude linearity and phase MAE are $2.95 \cdot 10^{-2}\%$ and $5.46 \cdot 10^{-2\circ}$. Given the considerations of Section III, the usage of the interpolation is necessary to achieve the minimum possible error in the correction of the nonlinearities.

B. Klystron

For klystron tests, the measurements were done at EuXFEL accelerating stations A9, A16, and A24, and at FLASH accelerating stations ACC2/3, ACC4/5, and ACC6/7. Each EuXFEL station is equipped with a horizontal 10-MW 117-kV multibeam klystron [3], FLASH ACC6/7 is equipped with a vertical klystron 10-MW 117-kV multibeam klystron, and FLASH ACC2/3 and ACC4/5 are equipped with a vertical 5-MW 128-kV klystron. All the klystrons were produced by Thales. The tests were performed with the klystrons waveguides attached to the accelerating modules. The amplifiers were

measured up to a peak requested amplitude 20% higher than the one used during normal operation. Such a decision was taken to allow the LLRF controller to have some margins of operation around its nominal working point. Therefore, special care was taken during the characterization of the amplifiers to avoid quenching by overdriving the superconducting cavities. Part of this constraint is fulfilled by using a triangle pulse, which results in an inefficient gradient filling of the resonators compared to a square one. In addition, the pulselength was set to 300 μs, which is shorter than the filling time of both EuXFEL and FLASH. Therefore, the VS gradient produced by the triangle pulse was less than one half the gradient produced in regular operation although the peak klystron amplitude was 20% higher. The first test was done on A16 and resulted in amplitude linearity and phase MAE of 0.41% and 0.61° or a relative error improvement of factors 12 and 4. Even though the predistorter produced a tangible improvement, this was one order of magnitude less than the one achieved on IOT at CMTB. Further experiments showed that distortions produced by the beginning of the modulator pulse, where the characterization is performed, limited the achievable linearity.

Therefore, the characterization pulse was shifted by 200 μs after the startup of the klystron to avoid such an issue. Successive tests on A9, A24, and ACC6/7, done with the modified characterization procedure, resulted in an amplitude linearity MAE of less than 0.1% and a phase MAE still between 1° and 0.1°. For ACC2/3 and ACC4/5, a particularly good linearization of the RF chain was obtained with a phase MAE, respectively, of $7.64 \cdot 10^{-2\circ}$ and $4.81 \cdot 10^{-2\circ}$, substantially lower than the values measured in the other stations (Fig. 9). The main

TABLE III
PREDISTORTION RESULTS

	Amplitude linearity MAE %	Phase MAE (deg)
IOT w/o predistortion	2.79	5.25
IOT w. predistortion	$2.95 \cdot 10^{-2}$	$5.46 \cdot 10^{-2}$
EuXFEL A9 w/o predistortion	2.04	$3.93 \cdot 10^{-1}$
EuXFEL A9 w. predistortion	$7.71 \cdot 10^{-2}$	$18.31 \cdot 10^{-2}$
FLASH ACC2/3 w/o predistortion	2.77	1.94
FLASH ACC2/3 w. predistortion	$3.83 \cdot 10^{-2}$	$7.64 \cdot 10^{-2}$

difference between ACC2/3 and ACC4/5 and the other measured stations is that they use a single-beam klystron. The reason why it is possible to achieve better linearization results with this kind of klystron is not clear, and further studies will be required. Finally, closed-loop measurements were performed on EuXFEL. Initial results show that the cavity RF stability is unchanged when switching on the predistorter. Future studies will be conducted at klystron saturation to evaluate the benefit of using predistortion on stability.

VI. CONCLUSION

In this article, the first tests of a predistortion-based linearizer with interpolating LUT on accelerator RF power chains at DESY were presented. With such a linearizer, used with IOT and klystrons at CMTB, EuXFEL, and FLASH, it was possible to lower the amplitude linearity MAE from more than 1% to less than 0.1% and the phase MAE to less than 1°, with at least a factor 2 improvements for multibeam klystrons and more than a factor 20 for the other RF amplifiers. Even though closed-loop tests did not show stability improvements, experiments nearer to the klystron saturation will be performed in the future. Questions remain on why the phase error after the linearization of FLASH ACC2/3 and ACC4/5 is roughly one order of magnitude lower than the one recorded in the other stations. Another study to be done is the evaluation of the impact of amplifier long-term drifts on the linearization capabilities of the predistorter. Given the excellent results achieved, it is expected that the predistorter component will be used at EuXFEL and FLASH during user runs by the beginning of 2020. Further studies could include tests on the RF chains of normal conducting structures, such as the accelerators RF guns [17], [18] and the bunch arrival corrector cavity [19].

REFERENCES

[1] R. G. Carter, "Review of RF power sources for particle accelerators," in *Proc. CAS-CERN Accel. School, RF Eng. Part. Accel.*, 1991, pp. 269–300.
[2] V. Ayvazyan *et al.*, "Digital low level RF control system for the DESY TTF VUV-FEL linac," Deutsches Elektronen-Synchrotron, Tech. Rep. PUBDB-2018-04056, TESLA-FEL 2005-06, 2005. [Online]. Available: https://bib-pubdb1.desy.de/record/414574/export/hx?ln=en
[3] V. Vogel, A. Cherepenko, J. Hartung, I. Harders, S. Choroba, and L. Butkowski, "Results of testing of multi-beam klystrons for the European XFEL," in *Proc. LINAC*, 2013, pp. 479–481.
[4] J. Branlard *et al.*, "LLRF tests of XFEL cryomodules at AMTF: First experimental results," in *Proc. SRF*, 2013, pp. 1126–1128.
[5] D. Kostin, W. Moeller, A. Goessel, and K. Jensch, "Superconducting accelerating module tests at DESY," in *Proc. SRF*, 2009, p. 1.
[6] J. Sekutowicz *et al.*, "CW and LP operation test of XFEL-like cryomodule," in *Proc. IPAC*, 2012, pp. 21–25.
[7] B. Aune *et al.*, "Superconducting TESLA cavities," *Phys. Rev. Special Topics-Accel. Beams*, vol. 3, no. 9, 2000, Art. no. 092001.
[8] S. Pfeiffer, G. Lichtenberg, C. Schmidt, H. Schlarb, and H. Werner, "Design of an optimal and robust controller for a free-electron laser exploiting symmetries of the RF-system," in *Proc. IEEE 51st IEEE Conf. Decis. Control (CDC)*, Dec. 2012, pp. 4253–4258.
[9] S. Kirchhoff, C. Schmidt, G. Lichtenberg, and H. Werner, "An iterative learning algorithm for control of an accelerator based free electron laser," in *Proc. 47th IEEE Conf. Decis. Control*, Dec. 2008, pp. 3032–3037.
[10] F. Zavosh *et al.*, "Digital predistortion techniques for RF power amplifiers with CDMA applications," *Microw. J.*, vol. 42, no. 10, p. 12, 1999.
[11] W. Cichalewski, "Linearization of microwave high power amplifiers chain in the RF systems of linear accelerators for FLASH and X-FEL," Ph.D. dissertation, Dept. Microelectron. Comput. Sci., Tech. Univ. Lodz, Łódź, Poland, 2008.
[12] M. Omet *et al.*, "Development and test of klystron linearization packages for FPGA-based low level RF control systems of ILC-like electron accelerators," in *Proc. 19th IEEE-NPSS Real Time Conf.*, May 2014, pp. 1–4.
[13] A. Savitzky and M. J. E. Golay, "Smoothing and differentiation of data by simplified least squares procedures," *Anal. Chem.*, vol. 36, no. 8, pp. 1627–1639, Jul. 1964.
[14] P. Virtanen *et al.*, "SciPy 1.0: Fundamental algorithms for scientific computing in Python," *Nature Methods*, vol. 17, pp. 261–272, Feb. 2020.
[15] M. Hoffmann *et al.*, "High speed digitial LLRF feedbacks for normal conducting cavity operation," in *Proc. IPAC*, 2014, pp. 1–3.
[16] D. Makowski *et al.*, "High-speed data processing module for LLRF," *IEEE Trans. Nucl. Sci.*, vol. 62, no. 3, pp. 1083–1090, Jun. 2015.
[17] M. Vogt *et al.*, "The free-electron laser FLASH at DESY," in *Proc. IPAC*, 2013, p. 1167.
[18] J. Branlard *et al.*, "European XFEL RF gun commissioning and LLRF linac installation," in *Proc. IPAC*, 2014, pp. 2427–2429.
[19] M. Fakhari, S. Pfeiffer, H. Schlarb, K. Flöttmann, and J. Rossbach, "Design of a normal conducting cavity for arrival time stabilization at FLASH," in *Proc. IPAC*, 2015, Art. no. WEPMA029.

Chapter 7

Conclusions and outlook

In this dissertation, different LLRF control techniques for the future EuXFEL CW/LP upgrade were presented. The upgrade requires the Q_L of the superconducting cavities to be $> 10^7$ to limit the RF power consumption. As a consequence the cavity RF bandwidth is of the order of some tens of Hertz. Therefore great attention is given to the detuning disturbances estimation. For this reason, a VS-optimized FPGA-based detuning estimator was designed and implemented in DESY's LLRF CW system. The estimator is also routinely used in HZDR as a tool to help operators in cavity tuning tasks. The ability to perform detuning estimations in real-time with a delay of $170\,\mu s$ and an RMSE in the order of a Hertz opens the possibility to use the module in future resonance controllers. The estimator also calculates the cavity bandwidth online, thus allowing the detection of quenches and multipacting events in CW and LP mode of operation. The delay of detection is orders of magnitude smaller than the existing system installed at EuXFEL. This feature was tested in simulations and at CMTB. Since the calibration of the RF signal is critical for to correctly estimate the cavity bandwidth and detuning, further studies will be needed to determine how and how frequently a re-calibration of the system is needed.

Then ponderomotive instability effects were studied. These effects are the result of the cavity's electromechanical feedback and are depends on the Q_L value.

The control of the monotonic instability was studied. The exploitation of an integral control policy to drive the cavity's piezoelectric tuners resulted in an effective way to prevent static drops when operating near cavity resonance. Another advantage of using an integral control policy is the capability of tuning the cavity to the desired value despite the inverse static drop. The oscillatory instability was also studied in TESLA cavities at accelerating voltages of 15 MV. Simulation with the literature parameters shows that the accelerating system is affected by the instability when detuned by few Hertz [97]. The presence of these effects was also confirmed at CMTB in several tests. The oscillatory instability prevents achieving long-term field stability when driving the accelerating cavities in VS mode at gradients $E_{acc} > 15\,\mathrm{MV\,m^{-1}}$ in a closed RF loop. A similar phenomena was also observed in the two cavities VS accelerator ARIEL. Although the vector sum accelerating field's stability was achieved, the individual cavities showed oscillating behavior in counter-phase [111]. Further research is going to be performed to determine the necessary changes to the field and resonance control systems to prevent oscillatory instabilities from developing when operating in a closed RF feedback loop.

Finally, an FPGA-based component to linearize the RF amplifier output was tested at CMTB, FLASH, and EuXFEL. The motivation for the development of this module was to correct the nonlinearities of the amplifiers that will equip EuXFEL after the CW/LP upgrade. The tests were conducted on IOTs and pulsed klystrons. The achieved mean average error of the RF chain linearity when using the linearizer is better than 0.1% and 1 deg in amplitude and phase. The advantages of using such a component are simplified machine setup operations and a constant RF actuator chain gain. The latter point allows maximizing the gain of the feedback of the RF controller.

7.1 Future development

Further development is needed to realize a LLRF system capable of driving accelerating modules at the EuXFEL CW/LP field stability specifications. The most important point is to develop the resonance controller since the rejection of microphonics and ponderomotive instabilities remains an open issue. The resonance
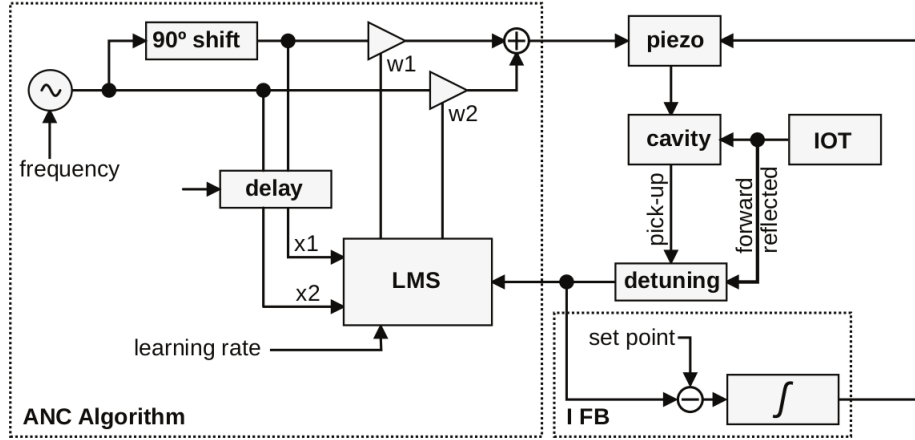
Figure (7.1) Actual LLRF detuning controller [68]. The detuning integrator is also shown.

controller should be designed to operate without complete apriori knowledge of the cavity mechanical dynamics and track eventual changes of the mechanical disturbances properties. Therefore a real-time adaptation of the controller to system variations is desirable. Here a list of possible improvements to the LLRF resonance control system is given.

Narrowband ANC The actual CW LLRF system implements a narrowband Least Mean Square (LMS) Active Noise Controller (ANC) to compensate for sinusoidal microphonics disturbance (Fig. 7.1) [112, 113].

This kind of microphonic disturbance is produced by rotary machinery that operates in the accelerator's proximity like pumps or ventilation and air conditioning fans. With this controller, a fixed frequency FPGA-based signal generator computes the sine and cosine values. These values are then rotated and used to drive the piezoelectric tuner. The applied rotation is iteratively updated using the measured detuning to cancel the mechanical disturbance.

$$p(n) = w_1(n) \cos(\omega_a n) + w_2(n) \sin(\omega_a n), \tag{7.1}$$

$$w_2(n+1) = w_2(n) - \mu e(n) \cos(\omega_a n - \Delta_a), \tag{7.2}$$

$$w_1(n+1) = w_1(n) - \mu e(n) \sin(\omega_a n - \Delta_a), \tag{7.3}$$

$$e(n) = y(n) - y_0, \tag{7.4}$$

with p the piezoelectric tuner drive, ω_a the signal generator frequency, w_1 and w_2 the adapted drive components, μ the learning coefficient, Δ_a a term to address the phase rotation produced by the cavity mechanical transfer function at ω_a and $y(n)$ and y_0 the measured detuning value and its setpoint. In the current LLRF controller, up to four narrowband ANC channels can be activated for a single cavity. The above scheme successfully reduced the magnitude of disturbances by up to 20 dB in tests at CMTB, achieving an RMSE for the detuning of less than one Hertz. One of the limitations of the actual narrowband ANC implementation is a fixed Δ_a term. Depending on the choice of Δ_a, the system can either cancel or amplify the detuning disturbance. Therefore a careful setup procedure has to be performed to achieve mechanical stability. Since EuXFEL has more than 800 cavities, the ANC manual setup would be a time-consuming and error-prone procedure to complete. Recent progress made at CBETA shows a possible method to automatically estimate the mechanical function's phase rotation [114]

$$\Delta_a(n+1) = \Delta_a(n) - \eta e(n)[w_1(n)\sin\left(\omega_a n - \Delta_a(n)\right) \tag{7.5}$$

$$-w_2(n)\cos\left(\omega_a n - \Delta_a(n)\right)], \tag{7.6}$$

with η the learning coefficient for the mechanical transfer function phase rotation adaptation. Another limitation of the presented narrowband ANC schemes is a fixed value for ω_a. Therefore, if the frequency of the noise source changes over time, the ANC cannot track and cancel the disturbance. In literature, the tracking of the disturbance frequency in the original narrowband ANC scheme is performed using a non-acoustic sensor [113]. This implies that the noise sources must continuously communicate their revolution frequency to the LLRF system to adapt to the frequency of the ANC units. It is unclear if all narrowband noise sources in an accelerator system can be identified apriori or if all the noise sources can be equipped with a non-acoustic sensor. A possible alternative to tracking disturbances with non-acoustic sensors is to use the detuning disturbance to adapt the narrowband ANC frequency [115]. This approach has the advantage of not requiring additional hardware modifications on the accelerator and the LLRF system.

Wideband ANC   Even though the narrowband ANC opened the possibility to operate accelerators with detuning disturbances in the order of magnitude of the Hertz [68, 114], only sinusoidal mechanical disturbances can be canceled. Therefore a detuning controller scheme that can reject non-periodic disturbances with time-varying spectral properties is advantageous for the accelerator's availability. The main issue to realize a resonance controller that works in wideband is the complexity of the mechanical transfer function [20]. A possible solution is to use a control scheme based on the LMS filter. Such a filter can estimate in real-time an arbitrary transfer function, and its use is widespread in audio and vibration control [113]. The filter's principle of operation minimizes the error square $|e(n)|^2$ that is achieved through the adaptation of a Finite Impulse Response (FIR) filter, which represents the cavity transfer function. The knowledge of the transfer function enables the compensation of the detuning over a broad range of frequencies. Two kinds of LMS-based ANC schemes can be used for resonance control: feedforward and feedback. In feedforward schemes, a noise pickup measures external microphonic vibrations before they result in a detuning disturbance. The adaptive filter transforms this information to generate a signal that cancels the incoming mechanical vibration. It is critical for the feedforward scheme to work because the vibration measuring device can produce a signal that is highly correlated to the observed detuning disturbance. Another possible scheme is the feedback LMS ANC. This control algorithm would rely only on the measured detuning disturbance to drive the piezoelectric tuners, thus not requiring additional external hardware. A version of this scheme was tested at HZB [75]. Another advantage of the feedback LMS ANC is its ability to correct for detuning disturbances regardless of whether they originate outside or inside the controlled system. Therefore the feedback LMS ANC can improve the resonance control of a high Q_L cavity system in the presence of ponderomotive oscillatory instabilities. Future studies will be planned to confirm the applicability of both feedforward and feedback wideband LMS ANC schemes to superconducting cavities.

Control for LP mode of operation   The LP mode of operation presents unique challenges in terms of detuning regulation. Contrary to the CW mode of operation, which operates at a fixed setpoint, the LP mode of operation periodic accelerating voltage excursions results in the periodic variation of the LFD of several cavity bandwidths. This detuning disturbance must promptly be corrected to

speed up the gradient filling and allow the beam acceleration at a stable condition. The periodic nature of this disturbance makes it possible to use an ILC algorithm. The most straightforward ILC algorithm that can be used for the scope is [116]

$$p_{k+1}(n) = p_k(n) - Ke_k(n), \qquad (7.7)$$

with k identifying the RF pulse, n the sample position within the pulse $p_k(n)$ the drive applied to the piezoelectric tuner, $e_k(n)$ the detuning error, and K the ILC gain. Therefore, every time an RF pulse is generated, (7.7) is updated, so the amplitude of $e_k(n)$ is minimized in the forthcoming pulses. Further studies are required to understand if (7.7) is sufficient or if a different ILC adaptation scheme has to be used. Another possible improvement to the resonance controller when operating in LP mode is to replace the integrator of [20] with a nonlinear controller to enable feedback gain scheduling during the filling where the system changes the most. One of these schemes is the Linear-Parameter-Varying control [117]. This kind of control is modeled as a parametric linear system and is under study at DESY and it is going to be tested during this year.

List of Figures

Bibliography

[1] Massimo Altarelli, Reinhard Brinkmann, Majed Chergui, Winfried Deck-
     ing, Barry Dobson, Stefan Düsterer, Gerhard Grübel, Walter Graeff, Heinz
     Graafsma, Janos Hajdu, et al. "The European x-ray free-electron laser tech-
     nical design report". In: *DESY* 97.2006 (2006), p. 4.

[2] *European XFEL*. URL: http://www.xfel.eu/.

[3] Takahiro Inagaki, C Kondo, H Maesaka, T Ohshima, Y Otake, T Sakurai,
     K Shirasawa, and T Shintake. "High-gradient C-band linac for a com-
     pact x-ray free-electron laser facility". In: *Physical Review Special Topics-
     Accelerators and Beams* 17.8 (2014), p. 080702.

[4] Gerardo D'Auria, Walter Wuensch, Adriana Wawrzyniak, Xander Janssen,
     Daniel Schulte, Graeme Burt, Qiang Gu, Tessa Charles, James Clarke,
     Steinar Stapnes, et al. *X-band Technology for FEL Sources*. Tech. rep.
     2014.

[5] Chao Feng and Hai-Xiao Deng. "Review of fully coherent free-electron
     lasers". In: *Nuclear Science and Techniques* 29.11 (2018), p. 160.

[6] Paul Emma. "Issues and R&D Critical to the LCLS". In: *PACS2001. Pro-
     ceedings of the 2001 Particle Accelerator Conference (Cat. No. 01CH37268)*.
     Vol. 1. IEEE. 2001, pp. 241–245.

[7] Peter McIntosh, R Akre, R Boyce, P Emma, Alan Hill, and C Rago.
     "Overview of the RF Systems for LCLS". In: *Proceedings of the 2005 Par-
     ticle Accelerator Conference*. IEEE. 2005, pp. 2753–2755.

[8]   S Di Matri. *Commissioning and Initial Operation of FERMI@ Elettra.* Tech. rep. SLAC National Accelerator Lab., Menlo Park, CA (United States), 2018.

[9]   Claudio Serpico, Nuaman Shafqat, Alexej Grudiev, and Roberto Vescovo. "High gradient, high reliability, and low wakefield accelerating structures for the FERMI FEL". In: *Review of Scientific Instruments* 88.7 (2017), p. 073303.

[10]   Heung-Soo Lee, Young Jung Park, Young-Do Joo, Hoon Heo, Jinyul Heo, Sang-Hee Kim, Soung-Soo Park, Woon Ha Hwang, Heung-Sik Kang, Kwang-woo Kim, et al. "S-band accelerating structures for the PAL-XFEL". In: *Journal of the Korean Physical Society* 66.3 (2015), pp. 340–344.

[11]   F Loehl, J Alex, H Blumer, M Bopp, H Braun, A Citterio, U Ellenberger, H Fitze, H Joehri, T Kleeb, et al. "Status of the SwissFEL C-band linear accelerator". In: *this conference.* 2013.

[12]   Zhentang Zhao, Dong Wang, Qiang Gu, Lixin Yin, Guoping Fang, Ming Gu, Yongbin Leng, Qiaogen Zhou, Bo Liu, Chuanxiang Tang, et al. "SXFEL: A soft X-ray free electron laser in China". In: *Synchrotron Radiation News* 30.6 (2017), pp. 29–33.

[13]   V. Ayvazyan, A. Brandt, S. Choroba, G. Petrosyan, K. Rehlich, S. N. Simrock, and P. Vetrov. "Digital RF Control System for The DESY FLASH Linear Accelerator". In: *EUROCON 2007 - The International Conference on "Computer as a Tool".* 2007, pp. 1178–1185. DOI: `10.1109/EURCON.2007.4400385`.

[14]   NJ Walker and D Kostin. "The European XFEL–experience and lessons learned". In: *Presentation, International Workshop on Future Linear Colliders (LCWS2017), Strasbourg, France.* 2017.

[15]   John N Galayda. *The LCLS-II: A high power upgrade to the LCLS.* Tech. rep. SLAC National Accelerator Lab., Menlo Park, CA (United States), 2018.

[16]   TO Raubenheimer et al. "The LCLS-II-HE, a high energy upgrade of the LCLS-II". In: *60th ICFA Advanced Beam Dynamics Workshop on Future Light Sources.* 2018, pp. 6–11.

[17]   HT Hou et al. "SRF Status of the SHINE Project at Shanghai". In: (2020).

[18]   Bernard Aune, R Bandelmann, D Bloess, B Bonin, A Bosotti, M Champion, C Crawford, G Deppe, B Dwersteg, DA Edwards, et al. "Superconducting TESLA cavities". In: *Physical Review Special Topics-Accelerators and Beams* 3.9 (2000), p. 092001.

[19]   A. Bellandi, Ł. Butkowski, B. Dursun, A. Eichler, Ç. Gümüş, M. Kuntzsch, A. Nawaz, S. Pfeiffer, H. Schlarb, C. Schmidt, K. Zenker, and J. Branlard. "Online Detuning Computation and Quench Detection for Superconducting Resonators". In: *IEEE Transactions on Nuclear Science* 68.4 (2021), pp. 385–393. DOI: 10.1109/TNS.2021.3067598.

[20]   Andrea Bellandi, Annika Eichler, Sven Pfeiffer, and Julien Branlard. "Integral Resonance Control In Continuous Wave Superconducting Particle Accelerators". In: *1st Virtual IFAC World Congress.* PUBDB-2020-04937. Strahlkontrollen. 2020.

[21]   Andrea Bellandi, Valeri Ayvazyan, Łukasz Butkowski, Wojciech Cichalewski, Burak Dursun, Çağıl Gümüş, Mathieu Omet, Sven Pfeiffer, Rüdiger Onken, Radoslaw Rybaniec, et al. "Results on FPGA-Based High-Power Tube Amplifier Linearization at DESY". In: *IEEE Transactions on Nuclear Science* 67.5 (2020), pp. 762–767.

[22]   M Altarelli. "The European X-ray free-electron laser facility in Hamburg". In: *Nuclear Instruments and Methods in Physics Research Section B: Beam Interactions with Materials and Atoms* 269.24 (2011), pp. 2845–2849.

[23]   B Dwersteg, K Flöttmann, J Sekutowicz, and Ch Stolzenburg. "RF gun design for the TESLA VUV Free Electron Laser". In: *Nuclear Instruments and Methods in Physics Research Section A: Accelerators, Spectrometers, Detectors and Associated Equipment* 393.1-3 (1997), pp. 93–95.

[24]   E. Vogel et al. *Recent developments towards CW operation of the superconducting XFEL accelerator.* Internal presentation. Online; accessed 29 January 2014.

[25]   Elmar Vogel. *Recent developments towards CW operation of the superconducting XFEL accelerator.* European XFEL Gmbh : Internal presentation. XFEL R&D report day. Dec. 2020.

[26]   P Pierini, A Bosotti, N Panzeri, D Sertore, J Iversen, W Singer, E Vogel, H Edwards, MH Foley, ER Harms, et al. "Third harmonic superconducting

cavity prototypes for the XFEL". In: *LINAC08, Victoria, BC, Canada* (2008), p. 821.

[27] Frank Brinker et al. "Commissioning of the European XFEL injector". In: *proceedings of IPAC* (2016).

[28] R Abela, A Aghababyan, M Altarelli, C Altucci, G Amatuni, P Anfinrud, P Audebert, V Ayvazyan, N Baboi, J Baehr, et al. *XFEL: the European X-ray free-electron laser-technical design report.* Tech. rep. DESY, 2006.

[29] Ayla S Nawaz, Sven Pfeiffer, Gerwald Lichtenberg, and Holger Schlarb. "Self-organzied critical control for the european xfel using black box parameter identification for the quench detection system". In: *2016 3rd Conference on Control and Fault-Tolerant Systems (SysTol)*. IEEE. 2016, pp. 196–201.

[30] A Nawaz, S Pfeiffer, G Lichtenberg, and P Rostalski. "Anomaly Detection for the European XFEL using a Nonlinear Parity Space Method". In: *IFAC-PapersOnLine* 51.24 (2018), pp. 1379–1386.

[31] Kasem Khalil, Omar Eldash, Ashok Kumar, and Magdy Bayoumi. "Self-healing hardware systems: A review". In: *Microelectronics Journal* 93 (2019), p. 104620.

[32] Christian Schmidt, Gohar Ayvazyan, Valeri Ayvazyan, V Branlard, and L Butkowski. "Recent developments of the European XFEL LLRF system". In: *IPAC, Shanghai, China* (2013).

[33] Thorsten Lamb, MK Czwalinna, Matthias Felber, Christopher Gerth, Tomasz Kozak, Jost Müller, Holger Schlarb, Sebastian Schulz, Cezary Sydlo, Mikheil Titberidze, et al. "Large-Scale Optical Synchronization System of the European XFEL with Femtosecond Precision". In: *Proc. IPAC'19* (2019), pp. 3835–3838.

[34] Cezary Sydlo, Matthias Felber, Christopher Gerth, Tomasz Kozak, Thorsten Lamb, Jost Müller, Holger Schlarb, Falco Zummack, et al. "Femtosecond optical synchronization system for the European XFEL". In: *Proceedings of IPAC2017* (2017), THPAB108.

[35] R MicroTCA. *is a trademark of PICMG.*

[36] Julien Branlard, Gohar Ayvazyan, Valeri Ayvazyan, MK Grecki, M Hoffmann, T Jezynski, IM Kudla, T Lamb, F Ludwig, U Mavric, et al. "The european XFEL LLRF system". In: *IPAC* 12 (2012), pp. 55–57.

[37] Julien Branlard, Gohar Ayvazyan, Valeri Ayvazyan, Mariusz Grecki, Matthias Hoffmann, Tomasz Jeżyński, Frank Ludwig, Uros Mavrič, Sven Pfeiffer, Holger Schlarb, et al. "MTCA.4 LLRF system for the European XFEL". In: *Proceedings of the 20th International Conference Mixed Design of Integrated Circuits and Systems-MIXDES 2013*. IEEE. 2013, pp. 109–112.

[38] J Branlard, V Ayvazyan, G Cancelo, J Carwardine, W Cichalewski, BC Chase, O Hensler, W Jałmuzna, S Michizono, C Schmidt, et al. "LLRF Automation for the 9mA ILC Tests at FLASH". In: *LINAC12, Israel* (2012).

[39] Sven Pfeiffer, Christian Schmidt, Marie Kristin Bock, Holger Schlarb, Wojciech Jalmuzna, Gerwald Lichtenberg, and H Werner. "Fast feedback strategies for longitudinal beam stabilization". In: *Proceedings of the 3rd International Particle Accelerator Conference*. 2012, pp. 26–28.

[40] C Schmidt, G Lichtenberg, W Koprek, W Jalmuzna, H Werner, and S Simrock. "Parameter estimation and tuning of a multivariable RF controller with FPGA technique for the Free Electron Laser FLASH". In: *2008 American Control Conference*. IEEE. 2008, pp. 2516–2521.

[41] Sven Pfeiffer. "Symmetric grey box identification and distributed beam-based controller design for free-electron lasers". In: (2014).

[42] Łukasz Butkowski, Vladimir Vogel, Holger Schlarb, and Jerzy Szabatin. "A Model-Based Fast Protection System for High-Power RF Tube Amplifiers Used at the European XFEL Accelerator". In: *IEEE Transactions on Nuclear Science* 64.6 (2017), pp. 1203–1210.

[43] M Killenberg, Sebastian Marsching, K Czuba, A Dworzanski, Martin Christoph Hierholzer, N Shehzad, L Petrosyan, Adam Piotrowski, Christian Schmidt, T Kozak, et al. "ChimeraTK: A toolkit for modular control applications". In: *11th International Workshop on Personal Computers and Particle Accelerator Controls*. PUBDB-2016-06461. Strahlkontrollen. 2016.

[44] S Goloboroko, G Grygiel, O Hensler, V Kocharyan, K Rehlich, and P Shevtsov. "DOOCS: an Object-Oriented Control System as the Integrating Part for the TTF Linac". In: *Proceedings of ICALEPCS*. Vol. 97. 1997, p. 141.

[45] A Aghababyan, C Bohm, P Gessler, A Hidvégi, H Kay, G Petrosyan, L Petrosyan, V Petrosyan, and K Rehlich. "XFEL Timing System Specifications". In: *Internal Conceptual Design Report, Short Version* 2 (2012).

[46] S Karstensen, ME Castro Carballo, JM Jäger, and M Staack. "XFEL machine protection system (MPS) based on UTCA". In: *2014 19th IEEE-NPSS Real Time Conference*. IEEE. 2014, pp. 1–4.

[47] Thomas Gerlach, Andreas Kugel, Andreas Wurz, Karsten Hansen, Helmut Klär, Dirk Müntefering, and Peter Fischer. "The DAQ readout chain of the DSSC detector at the European XFEL". In: *2011 IEEE Nuclear Science Symposium Conference Record*. IEEE. 2011, pp. 156–162.

[48] A Allahgholi, J Becker, L Bianco, A Delfs, R Dinapoli, P Goettlicher, Heinz Graafsma, D Greiffenberg, H Hirsemann, S Jack, et al. "AGIPD, a high dynamic range fast detector for the European XFEL". In: *Journal of Instrumentation* 10.01 (2015), p. C01023.

[49] John Coughlan, Sam Cook, Chris Day, Rob Halsall, and Saeed Taghavi. "The data acquisition card for the Large Pixel Detector at the European-XFEL". In: *Journal of Instrumentation* 6.12 (2011), p. C12057.

[50] J Sekutowicz, V Ayvazyan, J Branlard, M Ebert, J Eschke, T Feldmann, A Gössel, D Kostin, M Kudla, F Mittag, et al. "Feasibility of CW and LP Operation of the XFEL Linac". In: *Proc. of 35 Free–Electron Laser Conf.(FEL13)*. 2013, pp. 189–192.

[51] R Brinkmann, EA Schneidmiller, J Sekutowicz, and MV Yurkov. "Prospects for CW and LP operation of the European XFEL in hard X-ray regime". In: *Nuclear Instruments and Methods in Physics Research Section A: Accelerators, Spectrometers, Detectors and Associated Equipment* 768 (2014), pp. 20–25.

[52] Julien Branlard. *CW Studies at DESY's Cryomodule Test Bench*. `https://indico.bnl.gov/event/4460/contributions/24540/`. Second Topical Workshop on Microphonics, LLRF Workshop Series. Sept. 2018.

[53] John Smedley, Triveni Rao, BNL John Warren, DESY Jacek Sekutowicz, Richard Lefferts, and Andrzej Lipski. "Photoemission properties of lead". In: *EPAC04, Lucerne, Swiss* (2004).

[54] J Sekutowicz, SA Bogacz, D Douglas, P Kneisel, GP Williams, M Ferrario, I Ben-Zvi, J Rose, J Smedley, T Srinivasan-Rao, et al. "Proposed continuous wave energy recovery operation of an x-ray free electron laser". In: *Physical Review Special Topics-Accelerators and Beams* 8.1 (2005), p. 010701.

[55] J Sekutowicz, J Iversen, and G Kreps. *Nb-Pb superconducting RF-gun.* Tech. rep. Deutsches Elektronen-Synchrotron (DESY), 2005.

[56] Houjun Qian and Elmar Vogel. "Overview of CW RF Guns for Short Wavelength FELs". In: *39th Free Electron Laser Conf.(FEL'19), Hamburg, Germany, 26-30 August 2019.* JACOW Publishing, Geneva, Switzerland. 2019, pp. 290–296.

[57] Vladimir Vogel, Michael Bousonville, Andrey Cherepenko, Stefan Choroba, Hans-Joerg Eckoldt, Torsten Grevsmuehl, Valery Katalev, Karsten Machau, Petr Morozov, and Burcu Yildirim. "STATUS OF THE KLYSTRONS FOR THE EUROPEAN XFEL AFTER COMMISSIONING AND FIRST USER OPERATION PHASE". In: (2018).

[58] Elmar Vogel, Serena Barbanotti, Arne Brinkmann, Thorsten Buettner, Jens Iversen, Kay Jensch, Daniel Klinke, Denis Kostin, Wolf-Dietrich Möller, Andrea Muhs, et al. "Status of the All Superconducting Gun Cavity at DESY". In: *19th Int. Conf. on RF Superconductivity (SRF'19), Dresden, Germany, 30 June-05 July 2019.* JACOW Publishing, Geneva, Switzerland. 2019, pp. 1087–1090.

[59] Guan Shu, Ye Chen, Shankar Lal, HJ Qian, H Shaker, Frank Stephan, et al. "First Design Studies of a NC CW RF Gun for European XFEL". In: *Proc. 10th Int. Particle Accelerator Conf.(IPAC'19).* 2019, pp. 1698–1701.

[60] H. Padamsee, J. Knobloch, and T. Hays. *RF Superconductivity for Accelerators.* Wiley Series in Beam Physics and Accelerator Technology. Wiley, 1998. ISBN: 9780471154327.

[61] Denis Kostin and Jacek Sekutowicz. "Progress towards continuous wave operation of the SRF Linac at DESY". In: *Superconductivity and Particle Accelerators 2018.* Vol. 11054. International Society for Optics and Photonics. 2019, p. 1105406.

[62] W Singer, A Brinkmann, A Ermakov, J Iversen, G Kreps, A Matheisen, D Proch, D Reschke, X Singer, M Spiwek, et al. "Large grain superconducting RF cavities at DESY". In: *AIP Conference Proceedings.* Vol. 927. 1. American Institute of Physics. 2007, pp. 123–132.

[63] Marc Wenskat, Christopher Bate, Arti Dangwal Pandey, Brian Foster, Thomas Keller, Detlef Reschke, Joern Schaffran, Guilherme Semione, Sven Sievers, Andreas Stierle, et al. "Nitrogen Infusion R&D for CW Operation

at DESY". In: *29\textsuperscript {th} Linear Accelerator Conf.(LINAC'18), Beijing, China, 16-21 September 2018*. JACOW Publishing, Geneva, Switzerland. 2019, pp. 652–657.

[64]   Marc Wenskat, Christopher Bate, Arti Dangwal Pandey, Arno Jeromin, Thomas F Keller, Jens Knobloch, Julia Köszegi, Felix Kramer, Oliver Kugeler, Satish Kulkarni, et al. "Nitrogen infusion R&D at DESY a case study on cavity cut-outs". In: *Superconductor Science and Technology* 33.11 (2020), p. 115017.

[65]   Thomas P Wangler. *RF Linear accelerators*. John Wiley & Sons, 2008.

[66]   Curt Hovater et al. "RF control of high QL superconducting cavities". In: *Linear Accelerator Conference*. 2008, pp. 704–708.

[67]   A Neumann, W Anders, J Knobloch, O Kugeler, et al. "Microphonics in CW TESLA cavities and their compensation with fast tuners". In: *Proc. of the 2007 Workshop on RF Superconductivity, Beijing*. 2007.

[68]   Radoslaw Rybaniec, LJ Opalski, V Ayvazyan, L Butkowski, Sven Pfeiffer, Konrad Przygoda, Holger Schlarb, and Christian Schmidt. "Microphonic disturbances prediction and compensation in pulsed superconducting accelerators". In: *6th Int. Particle Accelerator Conf.(IPAC'15), Richmond, VA, USA, May 3-8, 2015*. JACOW, Geneva, Switzerland. 2015, pp. 2997–2999.

[69]   Julien Branlard, V Ayvazyan, H Schlarb Butkowski, Jacek Sekutowicz, Germany W Cichalewski, A Piotrowski, and K Przygoda. "LLRF system design and performance for XFEL cryomodules continuous wave operation". In: *Proc. of International Conference on RF Superconductivity (SRF2013)*. 2014, pp. 23–27.

[70]   Mariusz Grecki, Henning Weddig, Julien Branlard, Bartlomiej Szczepanski, Robert Wedel, Tomasz Poźniak, and Marcin Chojnacki. "Piezo control for XFEL". In: *arXiv preprint arXiv:1803.09042* (2018).

[71]   Rocco Paparella. "Fast frequency tuner for high gradient SC cavities for ILC and XFEL". PhD thesis. INFN, Milan Bicocca, 2007.

[72]   Andrea Bellandi, Valeri Ayvazyan, Julien Branlard, C Gümüs, S Pfeiffer, K Przygoda, and R Rybaniec. "LLRF R&D TOWARDS CW OPERATION OF THE EUROPEAN XFEL". In: *29\textsuperscript {th} Linear Accel-*

erator Conf.(LINAC'18), Beijing, China, 16-21 September 2018. JACOW Publishing, Geneva, Switzerland. 2019, pp. 223–226.

[73]   Serena Barbanotti, Andrea Bellandi, Julien Branlard, Kay Jensch, et al. "Modal Analysis of the EXFEL 1.3 GHz Cavity and Cryomodule Main Components and Comparison with Measured Data". In: *19th Int. Conf. on RF Superconductivity (SRF'19), Dresden, Germany, 30 June-05 July 2019.* JACOW Publishing, Geneva, Switzerland. 2019, pp. 488–492.

[74]   L Blum, H Wilhelm, B Petersen, and T Schnautz. "Status and commissioning results of the helium refrigerator plant for the European XFEL". In: *IOP Conference Series: Materials Science and Engineering.* Vol. 101. 1. IOP Publishing. 2015, p. 012138.

[75]   A Neumann, W Anders, O Kugeler, and J Knobloch. "Analysis and active compensation of microphonics in continuous wave narrow-bandwidth superconducting cavities". In: *Physical Review Special Topics-Accelerators and Beams* 13.8 (2010), p. 082001.

[76]   Dietrich Schulze. *Ponderomotive stability of rf resonators and resonator control systems.* Tech. rep. Kernforschungszentrum Karlsruhe (FR Germany). Inst. fuer Experimentelle …, 1972.

[77]   Jean Roger Delayen. "Phase and amplitude stabilization of superconducting resonators". PhD thesis. California Institute of Technology, 1978.

[78]   Curt Hovater, Trent Allison, Jean Delayen, John Musson, and Tomasz Plawski. *A digital self excited loop for accelerating cavity field control.* Tech. rep. Thomas Jefferson National Accelerator Facility, Newport News, VA, 2007.

[79]   Gang Huang, Sandeep Babel, Ramakrishna Bachimanchi, Matt Boyes, Garth Brown, Kerri Campbell, David Nam Sul Cha, Brian Chase, Ed Cullerton, Lawrence Doolittle, et al. "High precision RF control for the LCLS-II". In: *NAPAC2016, Chicago, IL, USA* (2016).

[80]   Paolo Pierini, Angelo Bosotti, Julien Branlard, Denis Kostin, Cecilia Maiano, Wolf-Dietrich Möller, Rocco Paparella, Detlef Reschke, Jacek Sekutowicz, Daniele Sertore, et al. "Limits for the operation of the European XFEL 3.9 GHz system in CW mode". In: *8th Int. Particle Accelerator Conf.(IPAC'17), Copenhagen, Denmark, 14â 19 May, 2017.* JACOW, Geneva, Switzerland. 2017, pp. 1023–1026.

[81] Cecilia Maiano, Michele Bertucci, Angelo Bosotti, Jin-Fang Chen, Paolo Michelato, Laura Monaco, Massimiliano Moretti, Carlo Pagani, Rocco Paparella, Paolo Pierini, et al. "Status of the Fabrication of the XFEL 3.9 GHz Cavity Series". In: *proceedings of IPAC* (2014).

[82] Ivan Gonin, Nikolay Solyak, and Timergali Khabiboulline. *FEA Analysis of the LCLS-II 3.9 GHz cavity full assembly (HV+Cavity+Tuner)*. Tech. rep. Technical Report. LCLS-II-16-03, Feb. 2016.

[83] Nikolay Solyak, I Gonin, H Edwards, M Foley, T Khabiboulline, D Mitchell, J Reid, and L Simmons. "Development of the third harmonic SC cavity at Fermilab". In: *Proceedings of the 2003 Particle Accelerator Conference.* Vol. 2. IEEE. 2003, pp. 1213–1215.

[84] R Paparella, M Bertucci, A Bosotti, and C Pagani. "Coaxial blade tuner for European XFEL 3.9 GHz cavities". In: *THP077, this conference.* 2013.

[85] Yuriy Pischalnikov, Evgueni Borissov, Jae-Chul Yun, et al. "Design and Test of the Prototype Tuner for 3.9 GHz SRF Cavity for LCLS II Project". In: *North American Particle Accelerator Conf.(NAPAC'16), Chicago, IL, USA, October 9-14, 2016.* JACOW, Geneva, Switzerland. 2017, pp. 140–142.

[86] U Mavric, K Czuba, D Kuehn, T Lesniak, H Schlarb, J Piekarski, J Branlard, and F Ludwig. "Drift Compensation Module for Pulsed or CW Machines at 1.3 GHz, 3.0 GHz and 3.9 GHz". In: *Low Level Radio Frequency Workshop 2015.* PUBDB-2015-06037. Strahlkontrollen. 2015.

[87] Louise Springer. "Untersuchung von Hochfrequenzdetektoren mit Trägerunterdrückung für die Regelung von Beschleunigerkavitäten im Attosekundenbereich". MA thesis. Am Schwarzenberg-Campus 1 21073 Hamburg: Technische Universität Hamburg (TUHH), 2018.

[88] U Mavric, M Hoffmann, F Ludwig, H Schlarb, and L Springer. "Automatic Loop for Carrier Suppression in Attosecond RF Receivers". In: ().

[89] Frank Ludwig et al. "RF Controls Towards Femtosecond and Attosecond Precision". In: *10th International Particle Accelerator Conference.* 2019, THYPLS1. DOI: 10.18429/JACoW-IPAC2019-THYPLS1.

[90] J Sekutowicz. personal communication. Apr. 1, 2021.

[91]   Sven Pfeiffer, Valeri Ayvazyan, Julien Branlard, Lukasz Butkowski, Radoslaw Rybaniec, Holger Schlarb, and Christian Schmidt. "Virtual Cavity Probe Generation using Calibrated Forward and Reflected Signals". In: *6th International Particle Accelerator Conference*. 2015, MOPWA040. DOI: `10.18429/JACoW-IPAC2015-MOPWA040`.

[92]   Thomas Schilcher. *Vector sum control of pulsed accelerating fields in Lorentz force detuned superconducting cavities*. Tech. rep. DESY, 1998.

[93]   Oleksiy Kononenko, Chris Adolphsen, Zenghai Li, Cho-Kuen Ng, and Claudio Rivetta. "3D multiphysics modeling of superconducting cavities with a massively parallel simulation suite". In: *Physical Review Accelerators and Beams* 20.10 (2017), p. 102001.

[94]   John Clarke Slater. "Microwave electronics". In: *Reviews of Modern Physics* 18.4 (1946), p. 441.

[95]   D Meidlinger et al. "A general perturbation theory for cavity mode field patterns". In: *Proceedings of SRF2009, Berlin, Germany, THPPO005* (2009).

[96]   Yanyun Ma, Ken Fong, Mahsa Keikha, James Keir, David Kishi, SR Koscielniak, Devon Lang, RE Laxdal, R Nagimov, ZY Yao, et al. "Microphonics investigation of ARIEL e-linac cryomodules". In: *the presented at the 29th Linear Accelerator Conf.(LINAC'18), Beijing, China*. 2018.

[97]   Tomasz Czarski, Krzysztof T Pozniak, Ryszard S Romaniuk, and Stefan Simrock. "TESLA cavity modeling and digital implementation in fpga technology for control system development". In: *Nuclear Instruments and Methods in Physics Research Section A: Accelerators, Spectrometers, Detectors and Associated Equipment* 556.2 (2006), pp. 565–576.

[98]   A Ushakov, P Echevarria, A Neumann, et al. "Detuning compensation in SC cavities using Kalman filters". In: *8th Int. Particle Accelerator Conf.(IPAC'17), Copenhagen, Denmark*. 2017.

[99]   Shane Koscielniak. *Ponderomotive Instability of RF Cavities with Vector Sum Control, and Cure By Difference Control*. 2019. arXiv: `1910.07106` `[physics.acc-ph]`.

[100] S. Choroba. "The High Power RF System for the European XFEL". In: *Proc. 29th Linear Accelerator Conference (LINAC'18), Beijing, China, 16-21 September 2018* (Beijing, China). Linear Accelerator Conference 29.

https://doi.org/10.18429/JACoW-LINAC2018-WE1A04. Geneva, Switzerland: JACoW Publishing, Jan. 2019, pp. 601–604. ISBN: 978-3-95450-194-6. DOI: `doi:10.18429/JACoW-LINAC2018-WE1A04`. URL: `http://jacow.org/linac2018/papers/we1a04.pdf`.

[101]   C. Adolphsen. "RF System Conceptual Design for the LCLS-II CW, SCRF Linac". In: *Proc. of 8th CW and average power RF workshop*. 2014. URL: `https://indico.cern.ch/event/276274/contributions/625713/`.

[102]   Anahid Dian Yeremian. *LCLS-II high power RF system overview and progress*. Tech. rep. SLAC National Accelerator Lab., Menlo Park, CA (United States), 2015.

[103]   P Marchand. "Review and prospects of RF solid state power amplifiers for particle accelerators". In: *Particle Accelerator Conf.(IPAC2017)*. 2017.

[104]   Andrey D. Grigoriev, Vyacheslav A. Ivanov, and Sergey I. Molokovsky (deceased). "O-Type Microwave Devices". In: *Microwave Electronics*. Cham: Springer International Publishing, 2018, pp. 109–202. ISBN: 978-3-319-68891-6. DOI: `10.1007/978-3-319-68891-6_7`. URL: `https://doi.org/10.1007/978-3-319-68891-6_7`.

[105]   *Canon Klystron product page*. Webpage. Accessed: 1.12.2020. URL: `https://etd.canon/en/product/category/microwave/klystron.html`.

[106]   A Yano, S Miyake, S Kazakov, A Larionov, V Teriaev, and YH Chin. "The toshiba E3736 multi-beam klystron". In: *Proceedings of LINAC*. 2004, pp. 706–708.

[107]   Meenu Kaushik and LM Joshi. "Inductive output tube (IOT)–a review". In: *Journal of Electromagnetic Waves and Applications* 29.15 (2015), pp. 2027–2037.

[108]   C. D. Child. "Discharge From Hot CaO". In: *Phys. Rev. (Series I)* 32 (5 May 1911), pp. 492–511. DOI: `10.1103/PhysRevSeriesI.32.492`. URL: `https://link.aps.org/doi/10.1103/PhysRevSeriesI.32.492`.

[109]   Richard G Carter. "Simple model of an inductive output tube". In: *IEEE transactions on electron devices* 57.3 (2010), pp. 720–725.

[110]   Feng Li. "Linearization of power amplifiers in wide band communication systems by digital baseband predistortion technique". PhD thesis. UNIVERSITE DE NANTES, 2012.

[111]   Ken Fong and Ramona Leewe. "Parametric Pumped Oscillation by Lorentz Force in Superconducting Rf Cavity". In: *10th International Particle Accelerator Conference*. 2019, WEPRB003. DOI: `10.18429/JACoW-IPAC2019-WEPRB003`.

[112]   Radosław Rybaniec, Konrad Przygoda, Wojciech Cichalewski, Valeri Ayvazyan, Julien Branlard, Łukasz Butkowski, Sven Pfeiffer, Christian Schmidt, Holger Schlarb, and Jacek Sekutowicz. "FPGA-based RF and Piezocontrollers for SRF cavities in CW mode". In: *IEEE Transactions on Nuclear Science* 64.6 (2017), pp. 1382–1388.

[113]   S. M. Kuo and D. R. Morgan. "Active noise control: a tutorial review". In: *Proceedings of the IEEE* 87.6 (1999), pp. 943–973. DOI: `10.1109/5.763310`.

[114]   Nilanjan Banerjee, Georg Hoffstaetter, Matthias Liepe, Peter Quigley, and Zeyu Zhou. "Active suppression of microphonics detuning in high Q L cavities". In: *Physical Review Accelerators and Beams* 22.5 (2019), p. 052002.

[115]   Chung-Ying Ho, Kuo-Kai Shyu, Cheng-Yuan Chang, and Sen M Kuo. "Efficient narrowband noise cancellation system using adaptive line enhancer". In: *IEEE/ACM Transactions on Audio, Speech, and Language Processing* 28 (2020), pp. 1094–1103.

[116]   Kevin L Moore. "Iterative learning control for deterministic systems". In: (2012).

[117]   Christian Hoffmann and Herbert Werner. "A survey of linear parameter-varying control applications validated by experiments or high-fidelity simulations". In: *IEEE Transactions on Control Systems Technology* 23.2 (2014), pp. 416–433.

Eidesstattliche Versicherung / Declaration on oath

Hiermit versichere ich an Eides statt, die vorliegende Dissertationsschrift selbst verfasst und keine anderen als die angegebenen Hilfsmittel und Quellen benutzt zu haben.

Die eingereichte schriftliche Fassung entspricht der auf dem elektronischen Speichermedium.

Die Dissertation wurde in der vorgelegten oder einer ähnlichen Form nicht schon einmal in einem früheren Promotionsverfahren angenommen oder als ungenügend beurteilt.

Hamburg, den 28.04.2021

_____

Unterschrift der Doktorandin

Acknowledgements

This thesis would not have been possible without the contribution and help of many people. I first want to thank my first supervisor, Dr. Julien Branlard, for introducing me to the complex world of particle accelerator controls, for always being open for discussion, and for the nice runs we did in Volkspark from time to time. Then I want to thank Prof. Wolfgang Hillert for always being available for a scientific discussion about accelerator physics. I want to thank also Dr. Holger Schlarb for allowing me participating in many international conferences and workshops. These experiences were invaluable to me. Thanks to Dr. Annika Eichler, Dr. Sven Pfeiffer, and Dr. Christian Schmidt for their deep knowledge in control systems and particle accelerators. Thanks to Cagil Guemus for always being available to help me every time the LLRF at CMTB didn't want to work, for the philosophical discussion about the cosmos and for the Turkish cuisine. Thanks to Ayla Nawaz for being a really positive and knowledgeable person. Discussing with you either cavity dynamics or culture was always a pleasure. Thanks to Dr. Paolo Pierini and Dr. Cecilia Maiano for introducing me to DESY. Hope to see you again in Lund. Thanks to Dr. Jacek Sekutowicz and his vast knowledge in superconducting cavities and passion for experiments. Thanks to Dr. Lukasz Butkowski, Burak Dursun, Katharina Schulz, Michael Buchler, Dr. Mariusz Grecki, Dr. Christopher Gerth, Dr. Uros Mavric, Gohar Ayvazyan, Jan Marjanovic, Louise Springer, Hanna Kunze, Dr. Martin Dr. Killenberg, Martin Hierholzer, Geogin Varghese and all the other MSK members. A special thanks to Dr. Denis Kostin, Dr. Valeri Ayvazyan, Jürgen Eschke, Ruediger Onken, Serena